

LA-UR-20-27730

Approved for public release; distribution is unlimited.

Title: ANALYTIC MODELING OF A DEEP SHIELDING PROBLEM

Author(s): Remedes, Tyler Joseph

Intended for: Dissertation Submission

Issued: 2020-09-30

Disclaimer:

Los Alamos National Laboratory, an affirmative action/equal opportunity employer, is operated by Triad National Security, LLC for the National Nuclear Security Administration of U.S. Department of Energy under contract 89233218CNA000001. By approving this article, the publisher recognizes that the U.S. Government retains nonexclusive, royalty-free license to publish or reproduce the published form of this contribution, or to allow others to do so, for U.S. Government purposes. Los Alamos National Laboratory requests that the publisher identify this article as work performed under the auspices of the U.S. Department of Energy. Los Alamos National Laboratory strongly supports academic freedom and a researcher's right to publish; as an institution, however, the Laboratory does not endorse the viewpoint of a publication or guarantee its technical correctness.

1 ANALYTIC MODELING OF A DEEP SHIELDING PROBLEM

2 By

3 TYLER J. REMEDES

4 A DISSERTATION PRESENTED TO THE GRADUATE SCHOOL
5 OF THE UNIVERSITY OF FLORIDA IN PARTIAL FULFILLMENT
6 OF THE REQUIREMENTS FOR THE DEGREE OF
7 DOCTOR OF PHILOSOPHY

8 UNIVERSITY OF FLORIDA

9 2020

ACKNOWLEDGMENTS

12 I would like to thank Dr. CJ Solomon, Dr. Mike Rising, Dr. Joel Kulesza, and Dr.
13 Jeff Favorite for help with developing MCNP. These colleagues were irreplaceable in
14 answering my questions and helping me understand some of the troubles I was having in
15 developing the MCNP models, especially Dr. Kulesza. I would also like to Dr. Jeremy
16 Conlin and Dr. Wim Haeck who thought a class on NJOY and Dr. Tom Saller who helped
17 me parse the NJOY ACE files to generate the cross section data I needed. I would also
18 like to acknowledge Dr. Cory Ahrens who Introduced me to my mentors who where
19 imperative in completing this dissertation.

20 I would like to specially thank Dr. Scott Ramsey and Mr. Joe Schmidt for providing
21 me the opportunity to complete my dissertation with Los Alamos National Laboratory,
22 mentor and guide me through the process, and provide knowledge and “pick me ups”
23 when I needed them. Thank you Scott and Joe.

²⁴ Finally, I would like to thank my friend Dr. Kelsey Stadnikia. She kept me going
²⁵ through the process when I was ready to acknowledge defeat. Without her encouragement,
²⁶ this document would not exist.

27 This work was supported by the US Department of Energy through the Los Alamos
28 National Laboratory. Los Alamos National Laboratory is operated by Triad National
29 Security, LLC, for the National Nuclear Security Administration of the U.S. Department
30 of Energy (Contract No. 89233218CNA000001). The authors thank J. Favorite and P.
31 Jaegers for valuable insights on these topics.

TABLE OF CONTENTS

		<u>page</u>
32		
33		
34	ACKNOWLEDGMENTS	3
35	LIST OF TABLES	6
36	LIST OF FIGURES	7
37	ABSTRACT	11
	CHAPTER	
38	1 INTRODUCTION AND MOTIVATION	13
39	1.1 Motivation	13
40	1.2 Practices for Code Reliability, Confidence, and Predictive Capability	16
41	1.3 State of Current Used Fuel Cask Research	19
42	1.4 General Description of the Work	25
43	1.4.1 Results Assessment	26
44	1.4.2 Sensitivity Analysis	26
45	1.5 General Overview of Chapters	27
46	2 DISCUSSION OF MAIN PROBLEM	29
47	2.1 Description of Detailed Model	32
48	2.2 Mathematical Model Choice	36
49	2.2.1 Fuel Region	37
50	2.2.2 Stainless Steel MPC	42
51	2.2.3 Dry Air Gap	45
52	2.2.4 Concrete Annulus	45
53	2.2.5 Carbon Steel Outer Shell	48
54	2.3 Identification of Features	53
55	3 THEORY	58
56	3.1 Derivation of the Boltzmann Transport Equation for Neutrons by Derivatives	59
57	3.1.1 External Neutron Sources	62
58	3.2 Reduction of NTE	63
59	3.2.1 Treatment of Time Dependence	63
60	3.2.2 Reduction to 1-D Planar	64
61	3.3 Multigroup Discrete Ordinates Approximation	65
62	3.3.1 Treatment of Energy Dependence	65
63	3.3.2 Treatment of Directional Dependence	67
64	3.4 Reduction to Diffusion Approximation	69
65	3.5 Cylindrical to Polar Coordinate Shift	72

66	4	ANALYSIS OF SUB-PROBLEMS	77
67	4.1	Identification of Mathematical Models in Each Region	77
68	4.2	Discussion of Sub-problems	79
69	4.2.1	Flat Region	79
70	4.2.2	Abrupt Level-off Region	81
71	4.2.3	Inter-bundle Depressions	84
72	4.2.4	Azimuthally Asymmetric Flux	88
73	4.2.5	Non-exponential Decay in Concrete	92
74	4.2.6	Flux in MPC and Carbon Steel Shell	93
75	4.3	Summary	96
76	5	SENSITIVITY ANALYSIS	98
77	5.1	Motivation of Sensitivity Analysis	99
78	5.2	Local Sensitivity Analysis Primer	102
79	6	SENSITIVITY THEORY OF REDUCED PHYSICS MODELS	106
80	6.1	Local Sensitivity Analysis of Representative Spent Fuel Cask Model	106
81	6.1.1	Fuel Region	106
82	6.2	Monte Carlo Based Sensitivity Analysis	109
83	7	DISCUSSION OF SENSITIVITY ANALYSIS	110
84	7.1	Comparison of Results	110
85	7.2	Summary	114
86	8	CONCLUSIONS	115
87	8.0.1	Recommendations for Future Work	117
88	REFERENCES		118
89	BIOGRAPHICAL SKETCH		121

90 LIST OF TABLES

91 <u>Table</u>	<u>page</u>
92 7-1 Summary of cross section data in the homogenized fuel.	110

LIST OF FIGURES

<u>Figure</u>	<u>page</u>
95 2-1 The Holtec HI-STORM 100 spent fuel cask system is designed to protect fuel, transfer decay heat to the environment, prevent proliferation of nuclear material, and attenuate radiation [1]. The MPC is seen partially inserted into the steel and concrete overpack. Current designs of the HI-STORM 100 do not use the inner shell and, therefore, the inner shield is not modeled in MCNP.	30
100 2-2 A cross section view of the multi-purpose canister. While there are multiple designs which accommodate different amounts of fuel, the MPC-32 is chosen for this work [1]. The MPC-32 is capable of holding 32 fuel bundles, one bundle in each square lattice element. The fuel basket and cylindrical wall of the MPC are made using stainless steel 304 and the canister is sealed by welding a baseplate to the bottom and a lid and closure ring to the top of the cylinder respectively.	31
106 2-3 The side view of the HI-STORM 100 spent fuel cask (canister and overpack) modeled in MCNP. This is referred to as the detailed model.	33
108 2-4 The top view of the HI-STORM 100 spent fuel cask modeled in MCNP. This view shows the fuel arrangement of the detailed model. This image shows the extent of geometric details which range from millimeters to meters.	34
111 2-5 The zoomed in image of a single fuel cell cross section in the detailed model. There are neutron absorbing pads (orange rectangles) placed along the interior left and upper faces of the fuel basket (pink regions). Fuel rods (small white circles) include a fuel region, helium gap, and cladding, the helium gap and cladding are not visible in the figure. The larger red circles are the cross sectional view of water cylinders which represent instruments used for monitoring the safety of the HI-STORM 100 spent fuel cask system.	35
118 2-6 The source spectrum used in MCNP simulations. The spectrum is a result of spontaneous fission and (α, n) reactions.	36
120 2-7 The interior neutron flux spatial distribution of the simulated HI-STORM 100 spent fuel cask. The vertical lines represent interfaces between material regions.	37
122 2-8 Energy spectrum of the neutron flux at various locations in the MPC where fuel rods are stored.	40
124 2-9 Angular distribution of the neutron flux at 2-9a 0.50 cm and at 2-9b the inner surface of the MPC (84.34 cm) from the centerline of the fuel cask.	41
126 2-10 The mean-free-path, or distance between interactions, of the materials in the fuel region. The source flux is provided in order to identify energy ranges of greater importance.	43
129 2-11 The mean-free-path of neutrons in stainless steel 304.	44

130	2-12 The neutron energy spectrum at a) 84.6cm and b) 86.6cm in the stainless steel MPC.	45
132	2-13 The neutron angular distribution at the a) inner surface and b) outer surface of the MPC.	46
134	2-14 The mean-free-path of neutrons in the air gap. The low density of gaseous air lead to a high MFP. The air gap can be treated as a streaming region since the MFP is much larger than the thickness of the air gap.	47
137	2-15 The mean-free-path of neutrons in the concrete annulus.	48
138	2-16 Energy spectrum of neutrons throughout the concrete annulus.	50
139	2-17 The angular distribution of the neutron flux at a) the inner surface (95.25cm) and the b) outer surface (166.37cm) of the concrete annulus.	50
141	2-18 The mean-free-path of neutrons in carbon steel.	51
142	2-19 The neutron energy spectrum near the a) inner surface (166.847cm) and the b) outer surface (167.803cm) of the carbon steel shell. The two peaks in each figure allude to a two energy group model.	52
145	2-20 The angular distribution of the neutron flux at the a) inner surface and b) outer surface of the carbon steel shell. Since the flux is heavily forward-pointed, two directions can be used to model the flux.	53
148	2-21 The neutron flux spatial distribution between the cask centerline and inner face of the MPC. The highlighted region is considered the flat flux region. This neutron flux is relatively flat and does not vary on the same order as the physical dimensions of materials in this region.	55
152	2-22 The flux stops decreasing and instead levels-off in the abrupt level-off region. The flux decreases less than 3% over the last ten centimeters before the interface between the fuel region and MPC.	55
155	2-23 There are three depressions in the neutron flux spatial distribution located approximately 22 cm apart. The flux decreases about 2% at each depression.	56
157	2-24 A density plot of the neutron flux at a “central slice” of the fuel cask as viewed from above. This plot shows the neutron flux is less in the upper left section than in the lower right section. The asymmetry is most evident in the blue and light blue sections at the outer radius of the figure.	56
161	2-25 A contrast plot emphasizing the asymmetry of the flux values.	57
162	2-26 The overpack accounts for about half of the reduction to the neutron flux. The purpose of investigating this region is to determine which physical processes are responsible for the attenuation.	57

165	3-1	As the factor $\frac{k}{r}$ decreases, the planar solutions better approximate polar solutions in the homogenous fuel material. The location of the black vertical line shows the point where the factor $\frac{k}{r}$ is 10% of its initial value.	76
168	4-1	The homogeneous model. The gray circle is the fully homogenized fuel which fills the entire volume interior to the MPC.	80
170	4-2	The results of the simulated neutron flux spatial distribution from the homogenous model (circles) is similarly flat to the neutron flux spatial distribution of the detailed model (solid line). The flux calculated using the diffusion approximation (dotted line) is also plotted against the two MCNP models. The diffusion approximation also shows the flatness of the neutron flux spatial distribution.	82
175	4-3	A) Section views of the homogeneous model, B) Helium model. The helium model includes an annulus of helium gas, ~ 10 cm thick, added around the homogenized fuel to allow streaming at the edge of the fuel region. Not to scale.	83
178	4-4	The neutron flux spatial distribution simulated by the helium model (circles) captures the neutron flux spatial distribution flattening out in the detailed model (solid line) over the 20 cm region before exiting the fuel region. The diffusion approximation (dotted line) also captures the flux flattening near 65 cm from the cask centerline after adding a helium annulus for neutron streaming.	85
183	4-5	The mean free paths for stainless steel 304 (blue), neutron absorbing pad material (orange), and fuel pin material (green). These three mean free paths are similar to the physical thicknesses of each material implying that the steel and neutron absorbing pads need to be included in MCNP simulations as discrete materials instead of being incorporated into the homogenized fuel.	86
188	4-6	The 1-D basket model used to identify the cause of the small depressions. The model is repeating layers of stainless steel (pink), neutron absorbing pads (orange), helium (blue), and cell homogenized fuel (gray).	87
191	4-7	The neutron flux spatial distribution simulated from the 1-D basket model. The colors are representative of each material: stainless steel 304 (pink), neutron absorbing pad (orange), helium (blue), and cell homogenized fuel (green). There are depressions present in the flux which occur within the stainless steel and neutron absorbing pads.	88
196	4-8	The ratio of the neutron flux spatial distribution in the upper left section of the fuel region to the neutron flux spatial distribution in the lower right section of the fuel region. This ratio is nearly 1 over the entirety of the fuel region, confirming the assumption that removing the neutron absorbing pads removes the previously identified depressions.	89

201	4-9	The cruciform model. The gray squares are cell homogenized fuel, the stainless steel fuel basket and MPC are pink, the helium annulus is blue, the air exterior to the MPC is green, and concrete is yellow. The neutron absorbing pads (orange) are present in this diagram, but are too thin to be seen here.	90
205	4-10	The neutron flux spatial distribution of the cruciform model (triangles) capture the flatness of, the leveling off of, and the depressions in the neutron flux spatial distribution seen in the detailed model (solid).	91
208	4-11	The neutron flux spatial distribution of the analytic E ₂ S ₂ model (dashed line), helium model (circles), and detailed model (solid lines). The fast and thermal portions of the E ₂ S ₂ solutions are shown in the blue and brown dotted lines respectively. The inset graphs shows the error between the analog models and detailed model.	93
212	4-12	The neutron flux spatial distribution of the analytic E ₂ S ₂ model (dashed line), helium model (circles), and detailed model (solid lines). The fast and thermal portions of the E ₂ S ₂ solutions are shown in the blue and brown dotted lines respectively. The inset graphs shows the error between the analog models and detailed model.	95
216	4-13	The neutron flux spatial distribution of the analytic E ₂ S ₂ model (dashed line), helium model (circles), and detailed model (solid lines). The fast and thermal portions of the E ₂ S ₂ solutions are shown in the blue and brown dotted lines respectively. The inset graphs shows the error between the analog models and detailed model.	96
220	7-1	Analytical sensitivity coefficients as a function of the cylindrical radius in the homogenized fuel region.	111
222	7-2	The absolute values of the sensitivity coefficients depicted in Fig. 7-1.	113

223 Abstract of Dissertation Presented to the Graduate School
224 of the University of Florida in Partial Fulfillment of the
225 Requirements for the Degree of Doctor of Philosophy

226 ANALYTIC MODELING OF A DEEP SHIELDING PROBLEM

227 By

228 Tyler J. Remedes

229 Dec 2020

230 Chair: James Baciak
231 Major: Nuclear Science and Engineering Program - Department of Material Science

232 Previous generations of scientists would make tremendous efforts to simplify
233 non-tractable problems and generate simpler models that preserved the fundamental
234 physics. This process involved applying assumptions and simplifications to reduce
235 the complexity of the problem until it reached a solvable form. Each assumption and
236 simplification was chosen and applied with the intent to preserve the essential physics of
237 the problem, since, if the core physics of the problem were eliminated, the simplified model
238 served no purpose. Moreover, if done correctly, solutions to the reduced model would
239 serve as useful approximations to the original problem. In a sense, solving the simple
240 models laid the ground-work for and provided insight into the more complex problem.

241 Today, however, the affordability of high performance computing has essentially replaced
242 the process for analyzing complex problems. Rather than “building up” a problem by
243 understanding smaller, simpler models, a user generally relies on powerful computational
244 tools to directly arrive at solutions to complex problems. As computational resources
245 grow, users continue trying to simulate new, more complex, or more detailed problems,
246 resulting in continual stress on both the code and computational resources. When these
247 resources are limited, the user will have to make concessions by simplifying the problem
248 while trying to preserve important details. In the context of MCNP, simplifications
249 typically come as reductions in geometry, or by using variance reduction techniques. Both
250 approaches can influence the physics of the problem, leading to potentially inaccurate

251 or non-physical results. Errors can also be introduced as a result of faulty input into a
252 computational tool: something as simple as transposing numbers in a tally input can
253 result in incorrect answers.

254 In this paradigm, reduced complexity computational and analytical models still have
255 an important purpose. The explicit form of an analytic solution is arguably the best way
256 to understand the qualitative properties of simple models [2]. In contrast to “building
257 up” a complex problem through understanding simpler problems, results from detailed
258 computational scenarios can be better explained by “building down” the complex model
259 through simple models rooted in the fundamental or essential phenomenology. Simplified
260 analytic and computational models can be used to 1) increase a user’s confidence in the
261 computational solution of a complex model, 2) confirm there are no user input errors, and
262 3) ensure essential assumptions of the simulation tool are preserved.

263 This process of using analytic models to develop a more valuable analysis of
264 simulation results is named the results analysis methodology. The utility of the results
265 assessment methodology and a complimentary sensitivity analysis is exemplified through
266 the analysis of the neutron flux in a dry used fuel storage cask. This application was
267 chosen due to current scientific interest in used nuclear fuel storage.

CHAPTER 1

INTRODUCTION AND MOTIVATION

1.1 Motivation

271 America is the largest producer of nuclear power in the world, with 98 reactors
272 producing approximately 805 billion kilowatt-hours of power in 2017 [3]. Despite being
273 the largest producer of nuclear energy, the United States has not established a permanent
274 used nuclear fuel storage facility. Instead, nuclear power plants store used fuel on site,
275 many using storage casks or canisters. A Savannah River National Laboratory report states
276 nearly 100,000 fuel assemblies are stored in more than 2,000 casks at 75 storage sites [4].

277 Fuel casks are designed to store and protect spent nuclear fuel while shielding power
278 plant workers and others from harmful radiation generated by unstable radioisotopes
279 created through the fission process. There does not exist a singular design of a spent fuel
280 cask due to multiple companies designing fuel casks and various types of spent nuclear fuel
281 which need to be stored. While each design is varied, there exist certain components which
282 are found across many spent fuel cask designs. Spent fuel casks typically have a right
283 cylindrical shape with layers of high atomic number and low atomic number materials,
284 such as steel alloys and concrete respectively. Layering materials with different atomic
285 numbers provides radiation shielding for both gamma rays and neutrons, which are the
286 two most penetrating types of radiation emitted by radioisotopes present in the fuel
287 (e.g., O-17, Cm-242, and Sr-90). High atomic number materials are used to mainly shield
288 gamma rays, whereas low atomic number materials are used to mainly shield neutrons.
289 For this reason, most spent fuel casks have an inner region where spent fuel is stored, an
290 outer region made of low atomic number materials (i.e. concrete) and high atomic number
291 materials (i.e. steel alloys). Layered materials are also utilized in baseplates and lids.

Materials in a spent fuel cask are specifically chosen to be multi-functional. Spent fuel casks must conduct heat away from spent fuel rods, protect fuel from damage, prevent proliferation of radioactive materials, as well as shield radiation. Heat conduction is

295 achieved by using materials with high thermal conductivities to draw heat away from
296 spent fuel rods to the environment. Thick layers of materials, such as steel and concrete,
297 protect the cask contents from environmental or other sources of damage (i.e. a hurricane
298 or a cask being dropped during transportation). Casks are also designed to prevent
299 proliferation by, for example, featuring welded lids or the addition of security tags to
300 discourage unauthorized access to spent fuel. Finally, spent fuel casks are designed
301 to shield employees and the public from the harmful radiation produced by decaying
302 radioisotopes created in the fuel during the power making process.

303 If a cask inadequately performs any of the above functions, it may become necessary
304 to open the cask for a visual inspection. This is a costly and time consuming endeavor.
305 Greulich et. al. state the cost to re-open a cask could be in the millions of dollars and
306 require man-months of time [5]. The process of opening a cask to visually inspect the
307 contents also carries an increased risk of exposing workers to radiation. The high costs
308 associated with opening a cask would certainly make visual inspection an unappealing
309 option. Simulation based and experimental research has been motivated by the desire to
310 develop a non-destructive assay technique to verify cask contents.

311 Analyzing the capabilities of technology to ensure the contents of a spent fuel cask
312 has motivated many scientific investigations, with a large reliance on computational
313 simulations [5–7]. Simulation results can then be correlated to experimental observations
314 in order to identify promising techniques to inspect the interior of a cask without opening
315 the cask. Neutron flux and dose are common measurable quantities sought after in the
316 simulation and experimental works surrounding radiation shielding investigations of spent
317 fuel casks. In reality, these two quantities are the same with the latter being a scalar
318 multiple of the former. These works tend to be concerned with the neutron flux at or
319 beyond the surface of the cask, since the radiation environment exterior to the spent
320 fuel cask is potentially harmful to worker safety. Understanding the interior neutron flux
321 is useful in any simulation studying the exterior neutron flux. The neutron flux at the

322 surface of the spent fuel cask is directly dependent on the physics occurring interior to
323 the spent fuel cask. Ultimately, the behavior of the interior neutron flux is controlled by
324 the configuration and choice of materials inside the fuel cask. The relationship between
325 interior structure and exterior neutron flux has prompted many simulation investigations
326 using radiation transport codes. Further, simulation tools are not only used to design
327 non-destructive assay techniques, but are also used to validate radiation transport codes as
328 applied to spent fuel casks.

329 Ideally, simulation results should be compared to a series of identical or similar
330 experiments *and* numerous results from other computational and numerical tools,
331 and analogous analytical models. Computational, numerical and analytical tools act
332 complimentary to experiments, in that the former tend not to be limited by physical
333 restraints such as, but not limited to, detector placement, experimental design challenges,
334 personnel safety, and costs. Nonetheless, experimental data is highly sought after since
335 analytical models only provide exact solutions for the most simplistic non-physical
336 problems and computational and numerical tools only approximate solutions, albeit these
337 approximations can be quite accurate. Unfortunately, limited amounts of experimental
338 data result in an increased reliance on computational and numerical tools. To further
339 exacerbate the issue, it is of utmost importance that conclusions can be confidently drawn
340 from simulation results. In the case of spent fuel casks, human lives and livelihood depend
341 on the correctness of simulation results. The results assessment methodology provides a
342 way to ensure the appropriateness and inerrancy of computational and numerical tools.

343 The results assessment methodology formulates analogs which are designed to share
344 phenomenological physics with its more detailed counterpart. A discussion motivating the
345 use of analogs is, therefore, useful. Fickett describes analogs as a qualitative representation
346 of the original, constructed, not derived, in order to maximize simplicity while minimizing
347 loss important properties [8]. Further, analogs have the following benefits 1) exact
348 solutions are simpler to find and more likely to exist, 2) mathematical rigor in determining

349 analytical solutions is reduced, and 3) salient physics is more readily observable after the
350 removal of extraneous features. The simplified computational and analytical models used
351 in this work are developed as analogs. Before further description of the analytical models
352 acting as analogs in this work, it is important to discuss the processes of validation,
353 verification, uncertainty quantification and sensitivity analysis as applied to general
354 computational tools and to simulations of used fuel casks.

355 **1.2 Practices for Code Reliability, Confidence, and Predictive Capability**

356 The behavior of physical systems is commonly described using complex mathematical
357 expressions, typically consisting of differential equations. Exact solutions of these
358 equations (also variously known as analytical or closed-form solutions) tend to be limited
359 to only the simplest scenarios. Indeed, the cost of exactly solving these equations often
360 involves the extensive use of simplifying assumptions to reduce the complexity of an
361 equation to a form where an analytical solution is possible. Approximating a differential
362 equation as a series of coupled linear equations became an alternative to finding direct
363 analytical solutions. Unfortunately, discretization introduces a degree of error into
364 the solution proportional to the fidelity to which a problem was discretized. Further,
365 discretization requires a high degree of computational rigor and, therefore, was not a
366 realistic technique for solving differential equations until adequate advancements in
367 computation had occurred. However, the modern-day advancement of computational
368 power has motivated the development of tools which approximate the solutions of complex
369 differential equations in broad sets of circumstances via approximation techniques, as
370 opposed to simplifying assumption techniques that may yield closed-form solutions only in
371 special cases.

372 These simulation tools, or simulation codes, often rely on algebraic calculations to
373 approximate solutions of the complex differential equations which describe real-world
374 physics. The processes of verification and validation generate evidence “that computer
375 [codes] have adequate accuracy and level of detail for their intended use” [9]. Verification

376 assesses “the numerical accuracy of the solution to a computational model,” and validation
377 “addresses the physical modeling accuracy of a computational simulation by comparing
378 the computational results with experimental data” [10]. Stated another way, verification
379 studies if a code solves equations correctly, and validation investigates the utility of a
380 code through comparison with experimental data. Beyond verification and validation,
381 uncertainty quantification has been added to quantify the accuracy with which simulation
382 codes predict outcomes. Sensitivity analysis can be considered a type of uncertainty
383 quantification which stratifies input parameters based on degree of impact to the error of
384 simulation results. A short description of verification, validation, and sensitivity analysis
385 will now be discussed.

386 Verifying a simulation tool requires demonstrating that the code is approximately
387 solving the underlying equations as intended by the code developer [11]. Two examples
388 of verification methods are benchmarking and comparison to analytical models. In
389 benchmarking, results from a simulation tool are compared to known solutions from
390 experiments, numerical tools, or other verified simulation tools.

391 Validation is ensuring a simulation tool approximately solves a representative set of
392 equations consistent with the applications of the code. Validation relies on comparing
393 experimental, analytical or numerical results against simulation results and validation is
394 conducted on an application specific situations. Simulation tools are validated for different
395 applications on a case-by-case basis. Validation commonly requires experimental data
396 for a given application. However, sometimes experimental data is limited or non-existent
397 since experiments can be financially burdensome, potentially risky to public and worker
398 health, or difficult to conduct due to proprietary reasons. Difficulties in obtaining
399 experimental data have led to alternative methods for validation, namely comparison
400 between simulation codes. This methods attempts to validate a code by comparing results
401 with a previously validated simulation code for an application.

402 Verification and validation determine the accuracy of a simulation tool for a specific
403 application, however, neither certifies the usage of a particular code in solving a problem.
404 Rather, it is the responsibility of the analyst to ensure that a particular simulation is
405 relevant to the solution of a problem - ensuring the simulation is made in accordance with
406 the manner which the code is verified and validated. Uncertainty analysis and sensitivity
407 analysis aid in this process.

408 Simulation tools require parameters, or data provided by the user, such as physical
409 properties measured through experiments (e.g., cross section data, viscosity, or thermal
410 conductivity. These values have associated error; measurement error is an example.

411 Uncertainty quantification is concerned with quantifying the error on the final result due
412 to the error of input parameters, as well as, error introduced by the simulation tool itself.

413 Further, uncertainty quantification is not concerned with the truth of a model, rather
414 how parameters effect the solution [12]. Sensitivity analysis improves on uncertainty
415 quantification by identifying which parameters most influence the result.

416 The typical approach to computational sensitivity analysis requires performing many
417 simulations where a change is made in each computation - an approach called the direct
418 method [13]. This process requires excessive computational resources. Applying sensitivity
419 analysis techniques to analytical models allows for the identification of sensitivities
420 without requiring as much computational resources, a strength of analytical sensitivity
421 analysis. Further, if an equation yields an analytical solution, the sensitivities of an
422 equation to its parameters can be found with minimal computational resources and
423 requires solving sensitivity equations only once.

424 The history of sensitivity analysis as applied to differential equations is broad and
425 extensive, therefore, only previous research that pertains to this work will be discussed.

426 The first methodology for sensitivity analysis was developed on linear electrical circuits
427 by Bode in 1945 [14]. At that time, sensitivity analysis motivated the use of feedback
428 in circuit design. From its origins in circuit control, sensitivity analysis permeated

429 many others fields of science, including nuclear engineering, and many methods were
430 developed. McKay provides an introduction into basic definitions and concepts related
431 to sensitivity analysis [15]. Cacuci unified and generalized the direct method and the
432 perturbation methods of sensitivity analysis in 1980 based on Frechet-derivatives [13].
433 A year later, Cacuci further generalized his methodology to analyze systems of response
434 along arbitrary directions using the Gâteaux-derivative (G-derivative). This non-linear
435 operator determines system responses to multiple perturbations in input parameters
436 simultaneously. In doing so, Cacuci developed the Forward Sensitivity Analysis Procedure
437 (FSAP) and Adjoint Sensitivity Analysis Procedure. The FSAP will be used to find
438 sensitivities of the linear differential equations in this work.

439 The overall purpose of performing verification, validation, uncertainty quantification,
440 and sensitivity analysis procedures is to identify the accuracy of a particular code for
441 given scenarios. Ultimately, a code user must decide if a code adequately simulates the
442 problem and if the user can have confidence that the simulated results are an accurate
443 portrayal of the real-world problem. While the processes of verification, validation, and
444 uncertainty quantification have been and continue to be extensively developed, there exists
445 a limitation - how can a code be validated if there is no experimental data for comparison?
446 The purpose of this document is to introduce a methodology aimed at answering this
447 question.

448 1.3 State of Current Used Fuel Cask Research

449 Interest in experimental and simulation work stems from the need to ensure the safety
450 and security of spent fuel casks; since there is currently no long term, national storage
451 plan. Before discussing how simulations have been used to study spent fuel casks, it is
452 important to take an aside and discuss the verification and validation of a commonly used
453 radiation transport simulation code, the Monte Carlo N-Particle (MCNP) simulation code.

454 MCNP has been extensively verified and includes a series of benchmark problems.
455 Further, Mosteller compiled a list of documents which discuss verification efforts on

456 MCNP [16]. analytical models have also been used in validation efforts [17, 18]. analytical
457 models provide an exact solutions against which simulation tools can be compared.
458 However, exact analytical solutions are often only available for heavily simplified problems
459 which do not represent physical systems. Nonetheless, excellent agreement has been
460 achieved between simple MCNP models and analytical solutions. Verification is considered
461 an activity in mathematics where a successful test demonstrates that the governing
462 equations of a simulation tool were solved correctly [19]. Validation of a simulation code is
463 undertaken after verification.

464 MCNP has also undergone general validation in multiple disciplines within nuclear
465 engineering; including but not limited to radiation shielding [20], criticality [21], and
466 intermediate and high-energy physics [22] where MCNP results were compared to
467 simple experiments. In order to validate computational tools as applied to spent fuel
468 casks, scientist have turned to a comparative method where results from other radiation
469 transport codes are compared with MCNP [23, 24]. However, discrepancies between results
470 from different simulation tools are attributed to different physics being included in each
471 tool. While this may be the driving factor leading to the apparent disagreement, this
472 conclusion would benefit from identifying the physics seen in one simulation tool and
473 neglected in the other. Comparison with experiments and other simulation tools is a valid,
474 imperative, and important technique for validating simulation results, but more analysis
475 should be done in order to increase confidence that simulation results can be trusted.

476 There exists a limited body of experimental work which measured the radiation dose
477 at or near the surface of various used fuel casks. Unfortunately, none of the experiments
478 were conducted on HI-STORM 100 spent fuel casks. Hence, discussion of past experiments
479 will include radiation measurements performed on any spent fuel cask, including but not
480 limited to experiments compared to any radiation transport code. Thiele et. al. even
481 include a comparison between experimental results and the results from two radiation
482 transport simulation tools (comparing Monaco/MARVIC with SAS4/MORSE) [25].

483 Both simulation tools are developed as part of the Standardized Computer Analysis
484 for Licensing Evaluation (SCALE) packages by Oak Ridge National Laboratory. Since
485 these radiation transport codes are not used in this work, no further explanation of the
486 codes will be given. The author's report concludes that simulation tools can be applied
487 for the assessment of dry storage casks. While experimental validation of simulation
488 results is arguably the best way to corroborate simulation results, it is still important to
489 not treat experimental data as sacrosanct [19]. Experiments still include measurement
490 and procedural errors, and without the validation of multiple experiments of the same
491 cask, the result of a lone experiment should not be considered to validate or invalidate
492 simulation results. There also exists a large number of various dry fuel storage casks and
493 experimental data may not exist to validate simulation results against. Computational
494 and numerical tools have proven useful as an alternative to experimental data. Ziock et.
495 al. measure the thermal neutron and gamma ray radiation signatures from six different
496 spent fuel cask designs; the HI-STORM 100 was not one of the six. The authors posit the
497 radiation signature can be used as an identifier for individual casks. Their experiments
498 proved inconclusive resulting from limitations of the imaging devices used. Wharton et.
499 al. used MCNP to determine the fraction of gamma rays which would be detected by a
500 high purity germanium detector placed at the top surface of two spent fuel cask designs
501 [26]. These simulations were used to determine the feasibility of a system designed to
502 used passive gamma radiation to determine if a fuel bundle was present or absent from
503 a spent fuel cask. The authors concluded that the thick shielding of the spent fuel casks
504 measured sufficiently scattered radiation and the system was not capable of resolving
505 discrete gamma ray peaks. This resulted in the measurements being stopped without fully
506 testing the capabilities of the system. It should be noted, the MCNP results suggested the
507 system was capable of performing the measurements and distinguishing between empty
508 and filled fuel storage positions. This work serves as an example for the importance of
509 corroborating simulation results with further investigations.

510 Simulation studies of the HI-STORM 100 spent fuel cask using MCNP are more
511 numerous than experimental studies. Priest conducted an in-depth investigation of
512 neutron and gamma flux and dose rates interior to a HI-STORM 100 spent fuel cask
513 with the purpose of identifying an imaging system capable of withstanding the harsh
514 environment inside the multi-purpose canister (MPC) [27]. The author performed
515 simulations using multiple MPC configurations with used nuclear fuel from both
516 pressurized water and boiling water reactors.

517 Harkness et. al. used MCNP to investigate the validity using helium-4 fast neutron
518 detectors to determine if fuel had been removed from a HI-STORM 100 spent fuel cask
519 [7]. This work describes a methodology to generate a source definition for MCNP based
520 on data provided in the Next Generation Safeguards Initiative. This fuel rod composition
521 data was aged using ORIGEN-S, a material irradiation and decay calculation code, to
522 create an MCNP compatible source definition. A further description of this process will
523 be provided later in this work. The neutron flux and energy spectrum at the surface of
524 the cask were tallied as part of this investigation. From the results of MCNP simulations,
525 the authors concluded that neutron spectroscopy was feasible using helium-4 detectors,
526 however, confidently determining if all fuel was present in a sealed spent fuel cask required
527 further investigation.

528 Miller et. al. determined the feasibility of using a mono-energetic photon source to
529 verify the contents of a sealed HI-STORM 100 spent fuel cask [28]. The authors simulated
530 photon transport through the spent fuel cask and found a 1000-fold reduction in the
531 transmitted flux when a fuel assembly is present as compared to a reduction of two in the
532 transmitted flux when there is no assembly present. The authors further corroborated
533 their work using analytical calculations to predict the scale of the uncollided flux for when
534 a fuel assembly is present and when there is no fuel assembly. The results from their
535 analytical modeling agreed with corresponding MCNP simulations.

536 Kelly et. al. performed an uncertainty analysis in radiation dose exterior to a
537 HI-STORM 100S (a variant of the HI-STORM 100 cask) spent fuel cask based on
538 variabilities in concrete composition and density [29]. The authors state that density
539 variations in the concrete have the largest effect on radiation shielding capabilities.
540 Varying concrete composition mostly affected neutron and associated capture gamma ray
541 dose rates.

542 Because of the interest in modeling radiation transport in spent fuel casks, research
543 has not been limited to using MCNP as a simulation tool nor has it been limited to a
544 single cask design. Gao et. al. use the radiation transport code MAVRIC (a radiation
545 transport code developed by Oakridge National Laboratory and distributed in with the
546 SCALE code package) to simulate neutron and gamma transport through a TN-32 spent
547 fuel cask [30]. In this work, the authors explore the effect of two geometries and two
548 sets of cross section data on the neutron and gamma fluxes at the surface of the cask.
549 The authors used a detailed model which included details of individual fuel rods and a
550 homogenous model which calculated a homogenous fuel definition that simplified the
551 geometry in each fuel cell. The authors also used two sets of cross section data. The
552 first set were continuous energy cross section data and the second were multigroup cross
553 sections. The authors concluded that changes to the geometry of the problem had a larger
554 effect on the result than changing how the cross section data was handled.

555 Interest in verifying cask contents has led to simulations investigating methods for
556 tomographic imaging. These investigations rely on simulation tools as a proof of concept
557 and to aid experimental design. Liao and Yang have used cosmic-ray muon simulations
558 to aid in experimental design choices for a spent fuel cask tomography system [31, 32].
559 The authors used Geant4 (another radiation transport code) and MCNP to simulate
560 cosmic-ray muon transport through a spent fuel cask as well as through a test setup to
561 guide experimental design. The authors then conducted experiments using the prototype

562 muon imaging systems. The authors concluded they were able to detect a quarter of a
563 missing fuel bundle located anywhere in the cask.

564 Greulich et. al. also investigated the possibility of tomographic imaging techniques in
565 verifying the contents of a spent fuel cask [5]. The authors simulated neutron transport
566 through a TN-32 spent fuel cask using MCNP. Using a beam source of neutrons incident
567 at the surface of the cask, the uncollided flux of neutrons leaving the cask provides
568 information which can be used to reconstruct an image of the interior of the cask.

569 The previously described works were all interested in either radiation dose or
570 radiation flux values at or exterior to the surface of the cask. Since dose is directly
571 proportional to flux, and since the exterior neutron flux is a direct result of how interior
572 cask structure affects the interior flux, the aim of this work is to investigate the interior
573 neutron flux so as to have the most general relevance to existing work. The neutron flux
574 was chosen over other types of radiation as the governing equation for neutrons is linear
575 and provides a basis and proof-of-concept for the results assessment methodology.

576 The body of work focusing on simulations of spent fuel cask is quite large, which
577 demonstrates scientific interest in simulating spent fuel casks. However, experimental
578 data to validate simulated results is limited. Further, the final safety analysis report
579 delivered by Holtec when licensing the HI-STROM 100 spent fuel canister system did
580 not include any experimental data pertaining to the radiation shielding capabilities of
581 this design [1]. Instead, MCNP was used to demonstrate the cask design was capable of
582 attenuating radiation to an adequate level. Maintaining a safe environment for power
583 plant workers and members of the public is of utmost importance and an alternate method
584 for validating the accuracy of simulation results is needed if simulation results are to be
585 relied upon in the absence of experimental data. The discrepancy between the amount
586 of simulated results and experimental data identifies the need to validate or otherwise
587 reinforce confidence in simulation results without relying on experimental data.

588

1.4 General Description of the Work

589 The results assessment and sensitivity analysis methods presented in this work act
590 complimentary to existing techniques - verification, validation, uncertainty analysis, and
591 sensitivity analysis- in order to develop a more valuable analysis. This work includes
592 high-fidelity MCNP simulations of the interior neutron flux from a Holtec Hi-STORM
593 100 spent fuel cask, and the attendant analytical analysis of the simulation results in the
594 absence of significant experimental validation data. A detailed model of the HI-STORM
595 100 spent fuel cask is simulated in MCNP to investigate the neutron flux interior to the
596 fuel cask. Owing to a lack of validation data against which to compare these simulation
597 results, an analytical analysis framework called "simulation results assessment" (or,
598 henceforth, "results assessment") is developed and applied to provide an alternative
599 (but not replacement) means for enhancing confidence in the computational model. The
600 accuracy of the model is assessed by first developing simplified analytical and MCNP
601 computational models. The design of these analogous models is made to retain essential
602 physics while reducing geometric complexities. Since the essential physics is preserved,
603 the neutron flux found using the analogous models will approximate the neutron flux
604 interior to the cask of the detailed model. Developing analogous models is an iterative
605 process where the initial simplified models were overly simplified and lost essential physics.
606 Essential physics was identified from locations where disagreements between the results of
607 the detailed model and the analogous models occur. More detailed analogs are developed
608 in order to rectify differences observed between the two sets of results until a final set
609 of analogous models are found. This process identified physical details that must be
610 preserved in the detailed model in order for the detailed model to accurately simulate
611 reality. A sensitivity analysis is also conducted on the final analogous model in each
612 material region as well as on the detailed model in order to further validate the accuracy
613 of the detailed model through the comparison of sensitivity structures between the models.
614 This is also an iterative process which involves further refinement of analogous models

615 and input parameters in order to achieve comparable sensitivity structures between the
616 detailed and analogous models. Finally confidence that the detailed model accurately
617 simulates the interior neutron flux of a HI-STORM 100 spent fuel cask is increased after
618 reaching comparable results and sensitivity structures between all models.

619 **1.4.1 Results Assessment**

620 A detailed model of this cask is developed in the MCNP code to predict the neutron
621 flux in its interior. In an attempt to isolate essential physics, 1) five other MCNP
622 simulations are developed to model various analogous problems, and 2) analytical models
623 are developed to explain key characteristics of the flux seen in these analogous problems.
624 The results of the simplified calculations are then used to reveal the fundamental physics
625 controlling the shape and other characteristics of the flux distribution resulting from the
626 complex model. This procedure is phenomenological in nature, and is thus intended to
627 capture elemental physical processes that are occurring within sub-regions of the full-scale
628 system. Therefore, while no single analytical solution is expected to be available for
629 the full-scale system, any understanding gained in the sub-regions reinforces confidence
630 that the integrated scales are being simulated in accordance with physical intuition.
631 This outcome is valuable in cases where experimental data is sparse or nonexistent. A
632 complimentary investigation of sensitivity structures produces a quantitative basis for
633 comparison of analytical and computational models.

634 **1.4.2 Sensitivity Analysis**

635 The procedure of quantifying comparisons between analytical models, reduced
636 geometry computational models, and the full model is demonstrated through the
637 inclusion of sensitivity analysis procedures. Forward modeling of sensitivity structures
638 is conceptually simple but computationally expensive for large problems, as it involves
639 sampling a space of possible parameter values and executing a new simulation for each
640 value. For analytical models the procedure is the opposite: using a generalized notion
641 of the directional derivative, sensitivity structures can be computed in closed-form. The

642 comparison of these two methods forms the final component of this work. In addition to
643 basic physics phenomenology, the sensitivity structure arising from analytical models can
644 be compared to that found from forward sensitivity modeling of full-scale simulations.
645 When these structures compare favorably, confidence in the full-scale simulations is once
646 again reinforced.

647 1.5 General Overview of Chapters

648 This document discusses the rigorous analysis of a HI-STORM 100 used fuel cask
649 using the results assessment methodology and a sensitivity analysis procedure. The results
650 assessment methodology is discussed in chapters [2](#), [3](#), and [4](#), and chapters [5](#), [6](#) and [7](#)
651 describe the process of adding a complimentary sensitivity analysis.

652 The second chapter of this document introduces the detailed MCNP model of the
653 HI-STORM 100 used fuel cask. This model is used to demonstrate the results analysis
654 methodology. The results of the simulated interior neutron flux are shown and features are
655 identified in this chapter. A feature is defined in more depth in chapter [2](#).

656 Chapter [3](#) introduces the various analytical models used in this work. The neutron
657 transport equation is derived and then reduced through application of assumptions and
658 simplifications. From a reduced form of the neutron transport equation, the multigroup
659 discrete ordinates equation and diffusion approximation are developed. The two equations
660 form the basis of the analytical modeling used in this work.

661 The results assessment methodology is demonstrated in chapter [4](#). This chapter
662 discusses why each analytical model is chosen as well as how each reduced complexity
663 computational model is developed. After describing how the models are determined,
664 each previously identified feature of the interior neutron flux is analyzed using the results
665 assessment methodology.

666 Chapter [5](#) provides an overview into sensitivity analysis using the FSAP. A record of
667 previous sensitivity analysis techniques is also provided. This chapter also introduces the
668 sensitivity analysis process which will be used for the computational models in MCNP.

669 Chapter 6 provides foundational theory of the FSAP.

670 Comparisons between the FSAP analysis on analytical models and MCNP results are

671 discussed in Chapter 7.

672 The last chapter includes final thoughts and conclusion regarding the work.

673 Recommendations for future work are also provided in chapter 8.

674

675

CHAPTER 2

DISCUSSION OF MAIN PROBLEM

676 Dry storage casks provide protection, shielding, security, and cooling for used
677 nuclear fuel which has spent at least one year in a spent fuel pool [33]. Shielding is
678 especially important as used nuclear fuel is highly radioactive after being removed from
679 a reactor and shielding is required to protect civilians, radiation plant workers, and the
680 environment. The storage of used nuclear fuel has become a challenge in the United
681 States since there is no long-term storage location. Instead, used nuclear fuel is stored in
682 dry storage casks at the facility where it was generated. These casks are designed to 1)
683 shield harmful radiation generated by the used nuclear fuel, 2) conduct decay heat away
684 from fuel rods to prevent damage to the fuel and cladding, 3) protect spent nuclear fuel
685 from environmental damage and other hazards, and 4) prevent proliferation of nuclear
686 materials. Large efforts have been made in studying and designing casks to accomplish
687 these challenges. While each function is imperative in analyzing the efficacy of a spent
688 fuel cask, this work is only concerned with the radiation shielding capabilities of a Holtec
689 International HI-STORM 100 spent fuel canister system.

690 Figure 2-1 is a diagram of the HI-STORM 100 spent fuel canister system partially
691 loaded into an overpack of the same name. These two components together, the canister
692 and overpack, will be referred to as a spent fuel cask. The HI-STORM 100 canister
693 system is chosen as it is the most common used fuel storage system in the United States
694 (750 canisters have been loaded before 2017) [4]. The overpack consists of two parts: a
695 cylindrical dual material structure welded to a baseplate and a dual material removable
696 lid. Both parts of the overpack use a combination of concrete and carbon steel to shield
697 radiation, protect fuel, and prevent proliferation of nuclear material. Four vents are
698 located at both the top and bottom of the overpack. These vents allow air to circulate
699 between the overpack and MPC, removing heat caused by decaying isotopes in the spent
700 fuel. Spent fuel rods are stored in the MPC, the central cylinder in Fig. 2-1. Figure 2-2 is

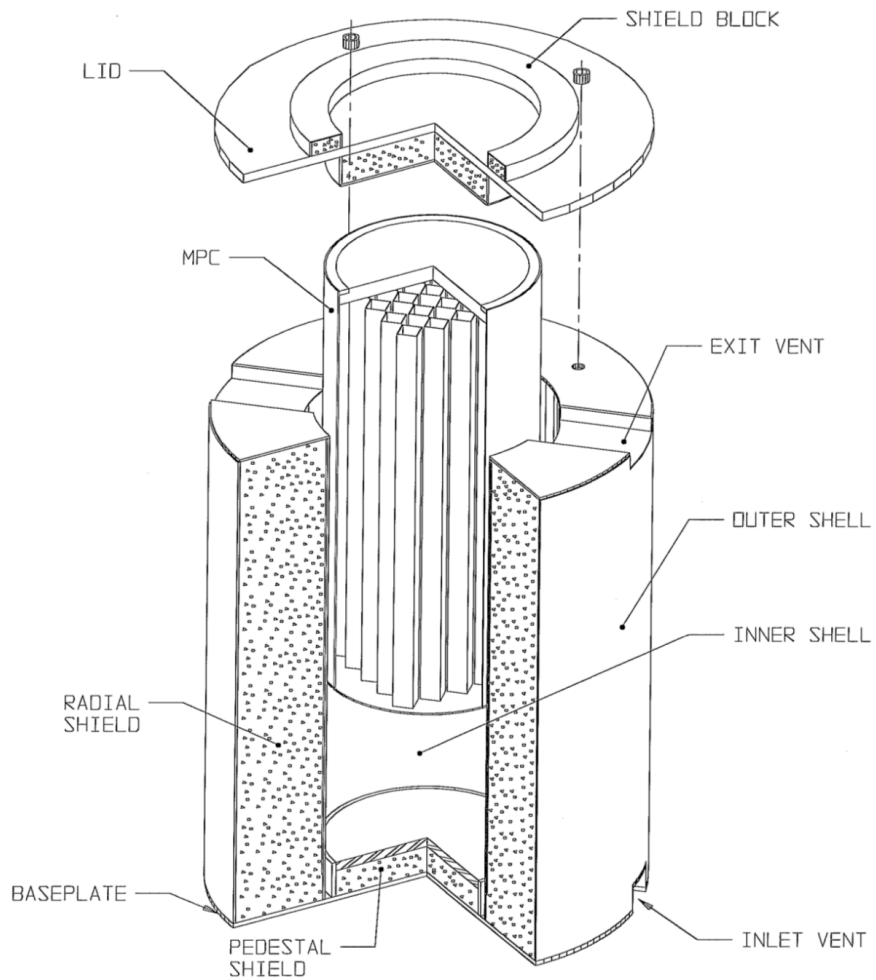


Figure 2-1. The Holtec HI-STORM 100 spent fuel cask system is designed to protect fuel, transfer decay heat to the environment, prevent proliferation of nuclear material, and attenuate radiation [1]. The MPC is seen partially inserted into the steel and concrete overpack. Current designs of the HI-STORM 100 do not use the inner shell and, therefore, the inner shield is not modeled in MCNP.

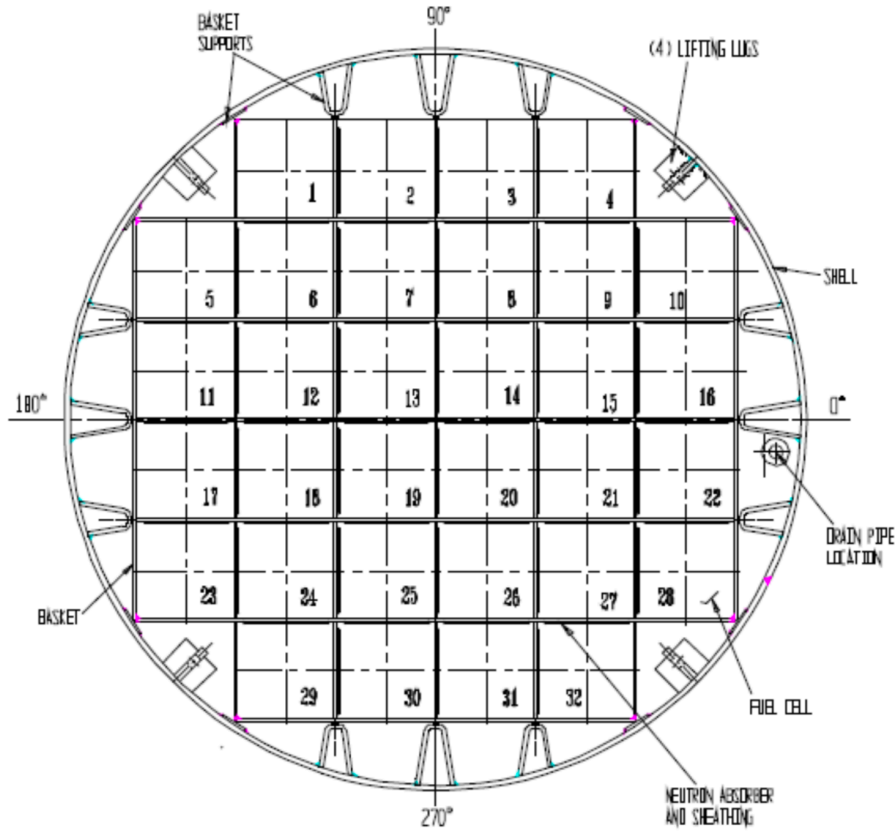


Figure 2-2. A cross section view of the multi-purpose canister. While there are multiple designs which accommodate different amounts of fuel, the MPC-32 is chosen for this work [1]. The MPC-32 is capable of holding 32 fuel bundles, one bundle in each square lattice element. The fuel basket and cylindrical wall of the MPC are made using stainless steel 304 and the canister is sealed by welding a baseplate to the bottom and a lid and closure ring to the top of the cylinder respectively.

701 the top-down cross section view of the MPC. Each cell in the honeycomb structure houses
 702 a single fuel bundle.

703 Power plant workers must be protected from the radiation produced by spent nuclear
 704 fuel rods, hence opening a sealed MPC is an expensive and potentially dangerous task.

705 Therefore, alternative methods are being explored to ensure the content and integrity
 706 of fuel components which do not require opening a cask. A sample of these techniques
 707 includes neutron spectroscopy, deduction of interior structure based on exterior dose
 708 rates, and neutron based computer tomography which were previously discussed in detail

709 in Section 1.3. Each of these techniques relies on simulations using various radiation
710 source definitions, virtual detectors, and simulated cask designs to determine specific
711 quantities related to the neutron flux within the spent fuel cask. The key metric of this
712 work is the interior neutron flux spatial distribution of the HI-STORM 100 spent fuel
713 cask, as this quantity is shared among research in spent fuel casks. Clearly, simulation
714 tools have become an important part of investigating the efficacy of a nondestructive
715 evaluation technique, and ensuring the accuracy of these results is even more important
716 since experimental data associated with the techniques is limited.

717 **2.1 Description of Detailed Model**

718 The MPC and overpack are modeled using the MCNP simulation code to determine
719 the simulated interior neutron flux spatial distribution averaged over the height of the cask
720 as a function of radial distance from the centerline. Figures 2-3 and 2-4 show, respectively,
721 a side view and cross section of the cask geometry simulated in MCNP. This model is
722 called the “detailed model” throughout this work and models the geometry of the cask
723 down to the individual fuel rod level. Each fuel rod acts as a source term for neutrons
724 produced from spontaneous fission and (α, n) reactions.

725 Figure 2-5 shows a single fuel cell cross section from the detailed model. The fuel
726 cell contains two neutron absorbing pads composed of boron-carbide and aluminum, 264
727 fuel rods with zircalloy cladding and 25 water rods representing instrumentation. Fuel
728 rod composition is determined using data from the Next Generation Safeguards Initiative
729 which analyzed the composition of Westinghouse 17x17 fuel bundles with various degrees
730 of initial ^{235}U enrichment and burn-up values [34]. This work investigates fuel with an
731 initial enrichment of 3% ^{235}U and a burn-up value of 30 GWd/MTU. The composition of
732 each individual fuel rod is unique, since fission fragment distribution is probabilistic, which
733 introduces variance in the local neutron flux. These variations in fuel rod composition
734 could influence the flux and potentially hide salient physics. Identifying and explaining
735 salient physics is a goal of this work. Therefore, an average fuel rod composition is

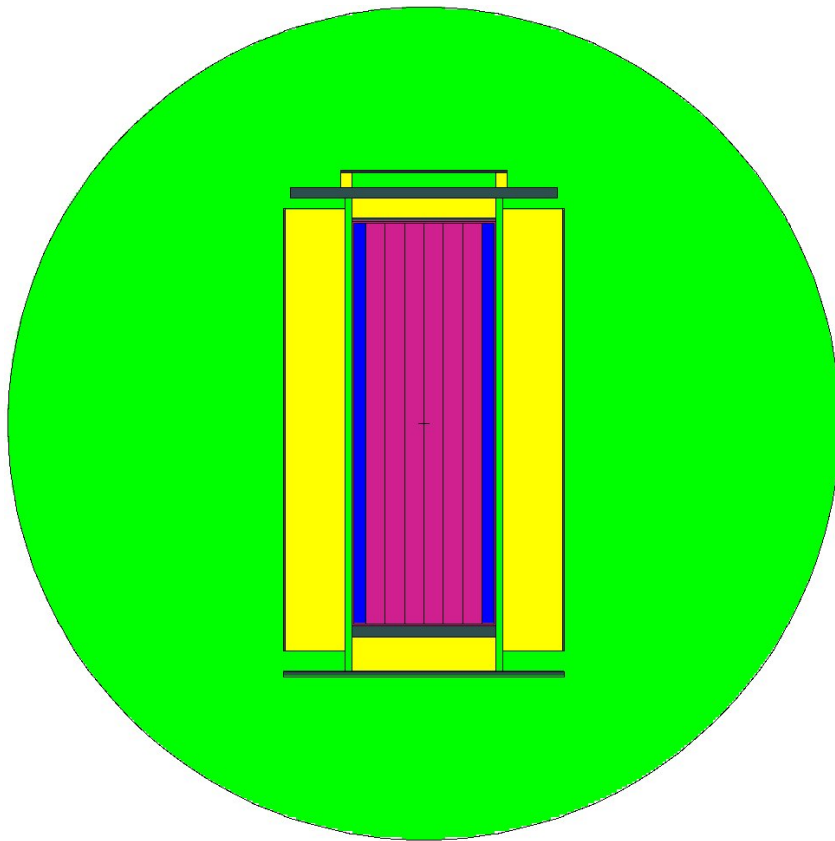


Figure 2-3. The side view of the HI-STORM 100 spent fuel cask (canister and overpack) modeled in MCNP. This is referred to as the detailed model.

736 determined based on the mass of each isotope present in a single spent fuel bundle in order
 737 to more clearly investigate the effects of geometry, detail, and non-fuel materials without
 738 influence from loading patterns of specific fuel rods.

739 The associated intrinsic neutron source is included via an MCNP neutron source
 740 definition. This definition is found using the ORIGEN-S 0-dimensional irradiation and
 741 decay code supplied with the SCALE package from Oak Ridge National Laboratory [35].
 742 The neutron energy spectrum associated with the intrinsic source is shown in Fig. 2-6.
 743 The source spectrum results from spontaneous fission of isotopes in the fuel (such as ^{252}Cf)
 744 and (α, n) reactions occurring in the irradiated fuel.

745 Fig. 2-7 depicts the height-averaged scalar neutron flux as a function of radial
 746 position within the HI-STORM 100 spent fuel cask predicted using MCNP. The color

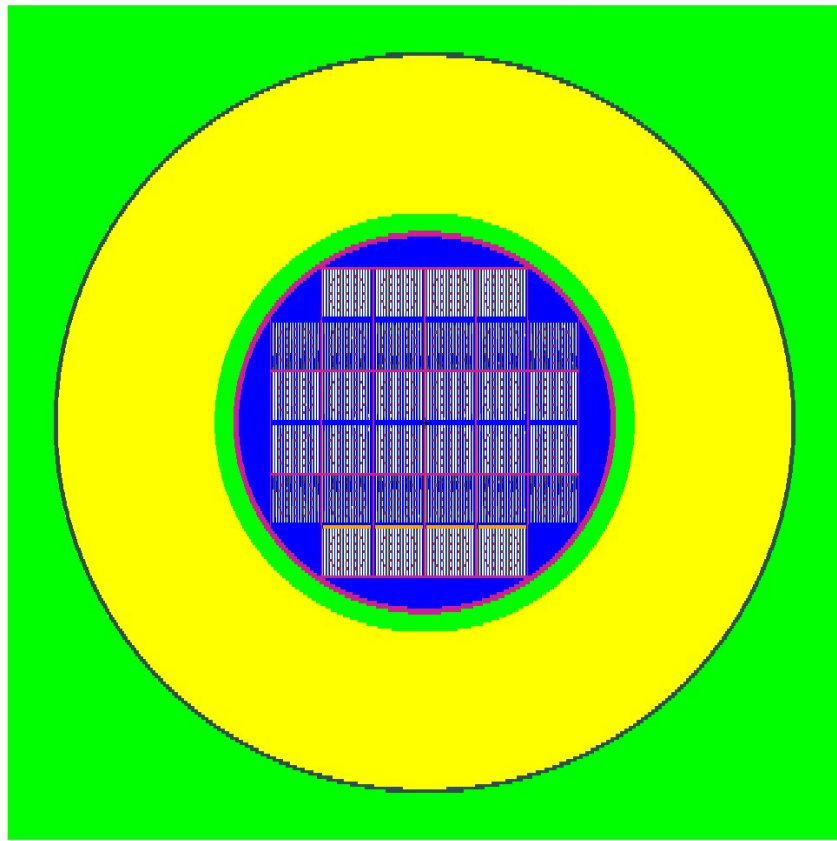


Figure 2-4. The top view of the HI-STORM 100 spent fuel cask modeled in MCNP. This view shows the fuel arrangement of the detailed model. This image shows the extent of geometric details which range from millimeters to meters.

747 of the line is related to the material through which the neutron flux is being simulated:
748 fuel is green (the entire area interior to the MPC is considered the fuel region), MPC is
749 blue, air is yellow, concrete is red, and carbon steel is black. The vertical lines designate
750 interfaces between material boundaries; green is the interface between the fuel region and
751 MPC, blue is the interface between the MPC and dry air, yellow is the interface between
752 air and the concrete annulus, red is the interface between concrete and carbon steel,
753 and black is exterior face of the cast. Figure 2-7 shows about half (54%) of the neutron
754 flux is attenuated in the fuel region, and the concrete further reduces the flux by 39%.
755 This result is intuitively sensible: the fuel region is comparatively dense and contains
756 neutron-absorbing materials (e.g., boron), while the thick concrete overpack region is

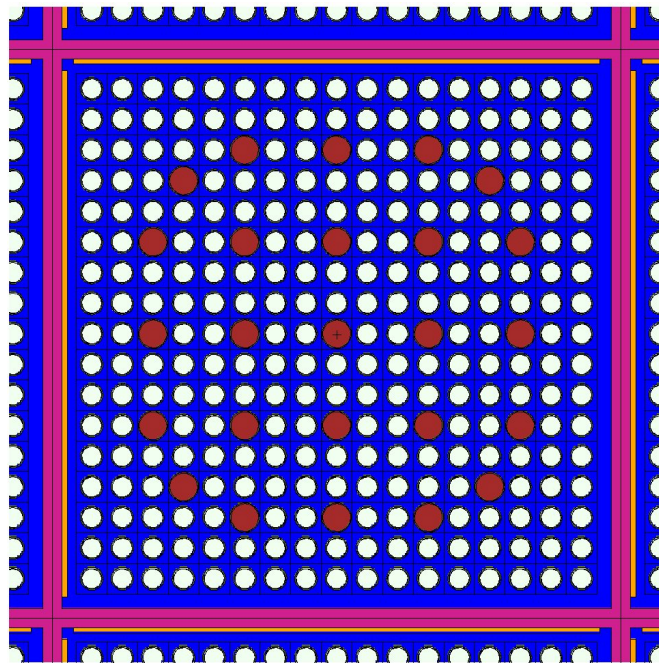


Figure 2-5. The zoomed in image of a single fuel cell cross section in the detailed model. There are neutron absorbing pads (orange rectangles) placed along the interior left and upper faces of the fuel basket (pink regions). Fuel rods (small white circles) include a fuel region, helium gap, and cladding, the helium gap and cladding are not visible in the figure. The larger red circles are the cross sectional view of water cylinders which represent instruments used for monitoring the safety of the HI-STORM 100 spent fuel cask system.

757 composed principally of highly thermalizing isotopes (e.g., hydrogen). Together, these
 758 processes are indicative of the observed dramatic reduction in neutron flux throughout
 759 the cask. However, advancing beyond intuition requires definitive answers to a variety of
 760 additional questions, namely:

- 761 • Are the results correct?
- 762 • Could a mistake have been made in the simulation input?
- 763 • Was an assumption made that neglected important physics?
- 764 • Does the problem include physics or exist in a physical regime outside the viability
 765 of the simulated tool used?

766 While corroborating simulation results with intuition is qualitatively valuable, quantitative
 767 or semi-quantitative assessments and their associated effects on confidence in simulation

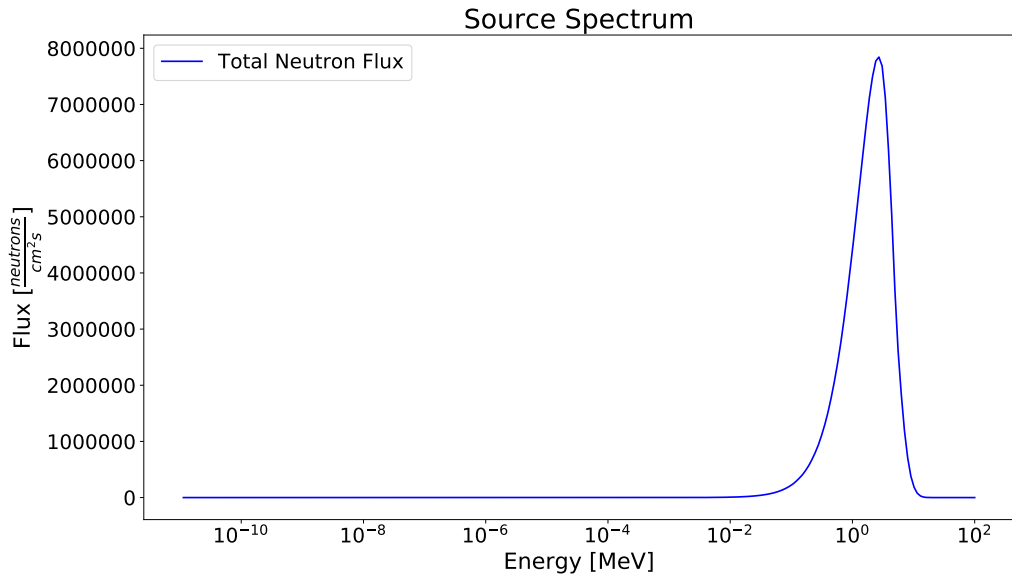


Figure 2-6. The source spectrum used in MCNP simulations. The spectrum is a result of spontaneous fission and (α, n) reactions.

768 results demands that the preceding questions be comprehensively addressed. The purpose
 769 of this work is to answer these questions by 1) identifying key features of the neutron
 770 flux spatial distribution as simulated in the detailed model, 2) developing simple physical
 771 models to determine the cause of each feature, and 3) gain confidence in the accuracy of
 772 the solution and inerrancy of the simulation process. In order to identify features in the
 773 neutron flux, each material region in the spent fuel cask is analyzed briefly.

774 **2.2 Mathematical Model Choice**

775 In the interest of constructing a complementary analytic representation of the
 776 neutron population behavior within the cask fuel region, inspection of the various features
 777 appearing in Figs. 2-1 and suggests several modeling simplifications.

778 • Aside from various isotope production and depletion processes featuring characteristic
 779 time scales spanning weeks to years, the spent fuel cask is essentially a static object.
 780 It is therefore assumed that the analytical representation of the cask is entirely
 781 time-independent (hereafter referred to as "static").

782 • The neutron energy spectrum within the fuel region is essentially "fast"; that
 783 is, it principally exists at fission neutron energies (i.e., 1-2 MeV) with minimal

Spatial Variation of Flux

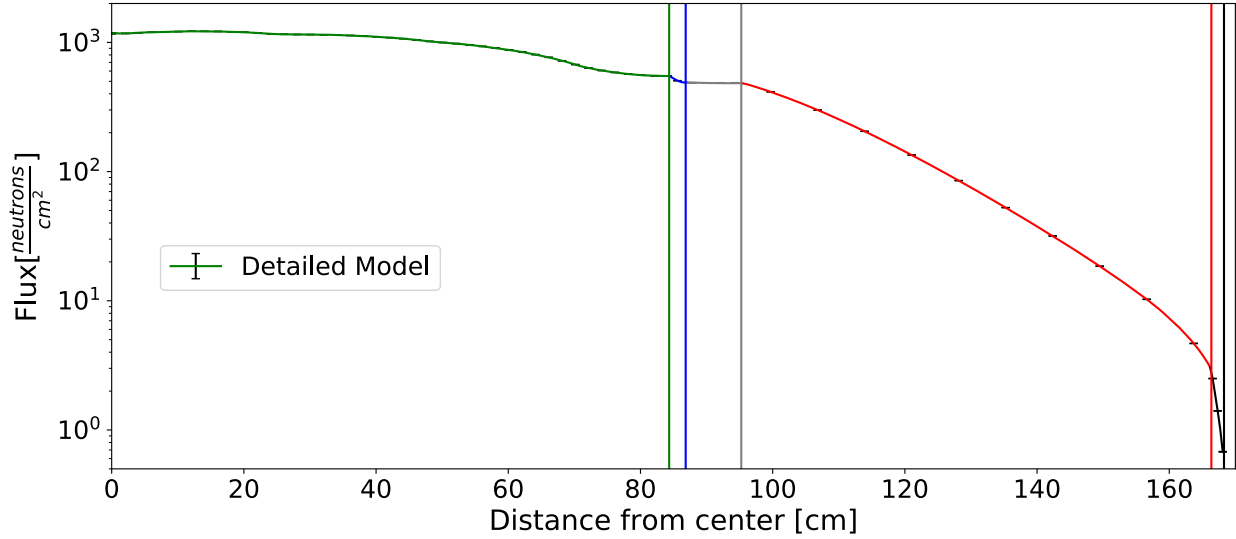


Figure 2-7. The interior neutron flux spatial distribution of the simulated HI-STORM 100 spent fuel cask. The vertical lines represent interfaces between material regions.

784 thermalization. As such, the analytical model used to characterize the cask fuel
 785 region is taken to be approximately monoenergetic.

786 • Owing to the high hydrogen content in the concrete annulus, the energy spectrum
 787 can be represented with two energy groups (one thermal and one fast). An analytic
 788 model characterizing the neutron transport in concrete is assumed to require two
 789 energy groups.

790 As a consequence of these observations and associated simplifications, a static,
 791 monoenergetic balance law model is used to characterize the neutron population
 792 information within the cask fuel region.

793 2.2.1 Fuel Region

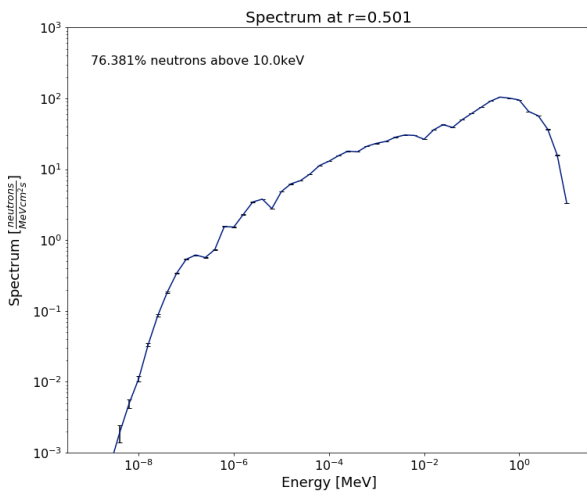
794 The fuel region of the HI-STORM 100 spent fuel cask features various materials
 795 including spent UO₂ nuclear fuel, a stainless steel basket, boron-containing neutron
 796 absorbing pads, and helium backfill. The geometric configuration of these materials is
 797 highly complex, as depicted in Fig. 2-1. Unfortunately, a single mathematical model
 798 capable of describing the neutron flux in the fuel region would not be tractable. Therefore,
 799 a simplified model must be developed using assumptions and approximations derived from

800 physics occurring in the model. In order to identify appropriate simplification, the energy
801 spectrum and angular distribution of the neutron flux and cross section data of various
802 materials are analyzed at various locations in the fuel region.

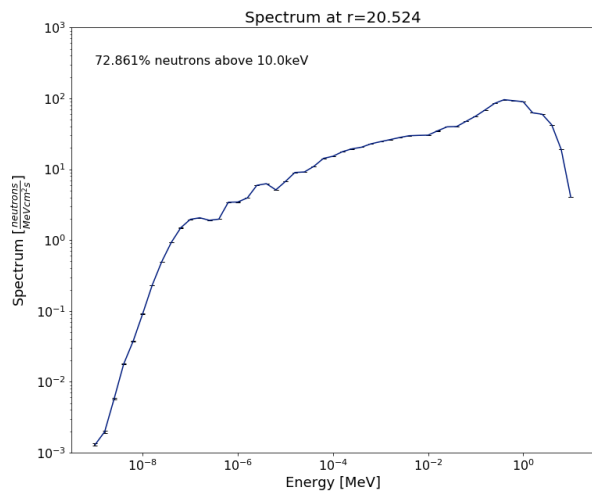
803 Figure 2-8 shows the energy spectrum of the neutron flux throughout the spent fuel
804 cask. These plots show the neutron flux has little variation throughout the fuel region.
805 This is a result of evenly distributing fuel rods through the fuel region. Further, the lack
806 of thermalizing materials in the fuel cask means there is little change in the neutron
807 spectrum. Therefore, it can be assumed that energy dependence of the neutrons can be
808 handled uniformly throughout the fuel region. This is a very helpful assumption that
809 allows for uniform treatment of material properties throughout the fuel region with respect
810 to energy. Unfortunately, there have been no assumptions concerning how to handle
811 neutron energy-dependence at this point, (e.g., is a monoenergetic method appropriate, or
812 will a different model be require?).

813 Analysis of the energy spectrum will determine how to best handle energy-dependence.
814 The percent of neutrons above 10keV varies between $\sim 78\%$ at inner radius values to $\sim 71\%$
815 at the edge of the fuel region as shown in Figs. 2-8a-2-8h. A monoenergetic handling
816 of the energy-dependence can be assumed since the majority of neutrons have energies
817 between 10keV and 10MeV, using an appropriate group weighting spectrum described
818 by Bell and Glasstone [36]. After choosing a method for handling energy-dependence,
819 it becomes necessary to determine a method for handling directional-dependence of the
820 neutron flux.

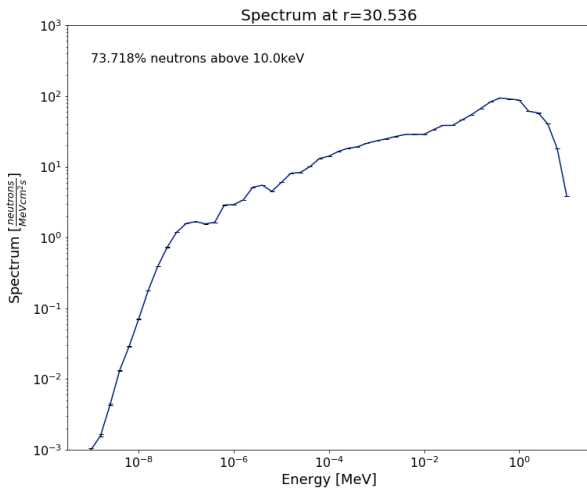
821 Figure 2-9 shows the angular distribution of the flux 0.5cm from the centerline (Fig.
822 2-9a) and at the edge of the fuel region (Fig. 2-9b). The angular distribution was tallied
823 at these locations to capture the two extents of the angular flux. A perfectly isotropic flux
824 would be a horizontal line with zero slope. If half of the neutron population is traveling
825 in either direction (inward and outward), then the neutron flux can be approximated
826 as isotropic with the understanding that deviations from isotropy will lead to errors in



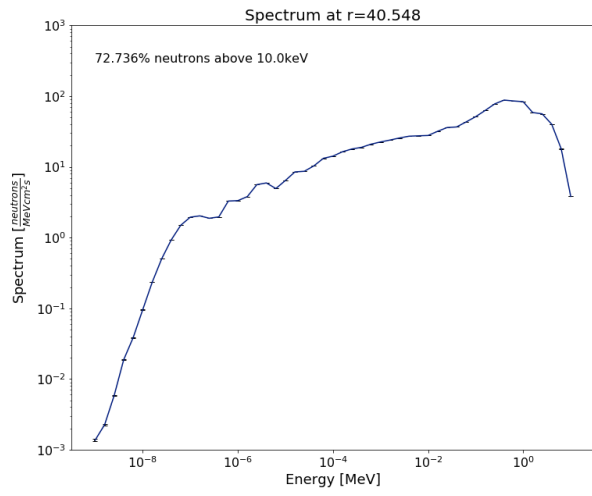
(a)



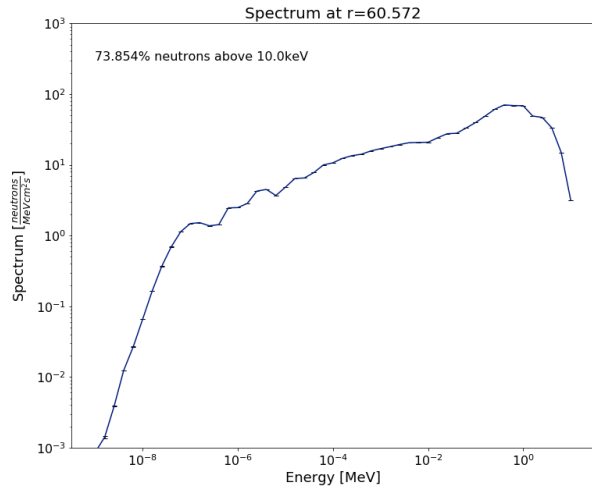
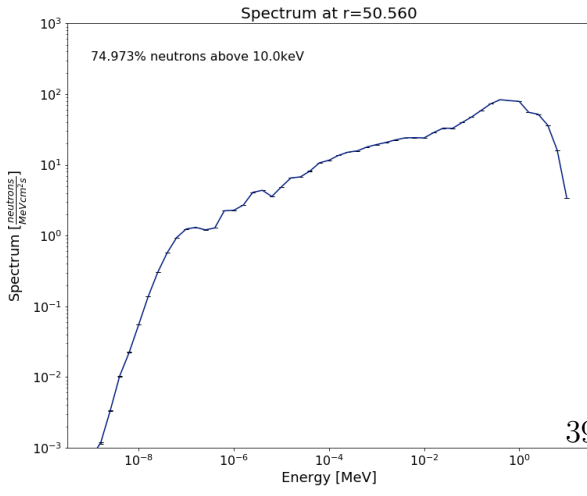
(b)

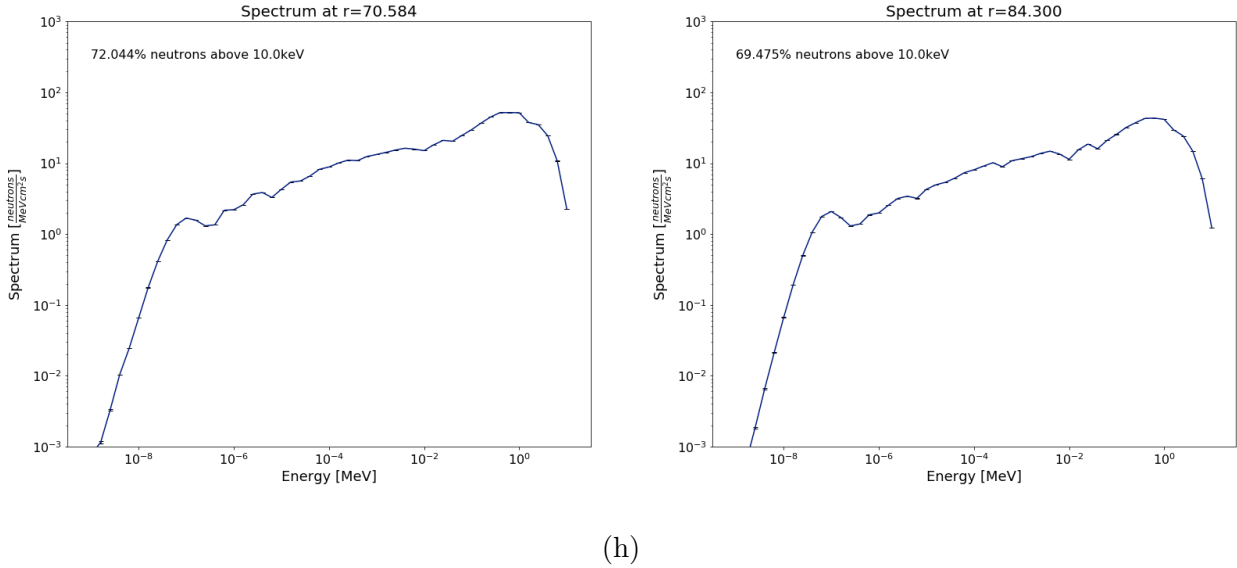


(c)



(d)



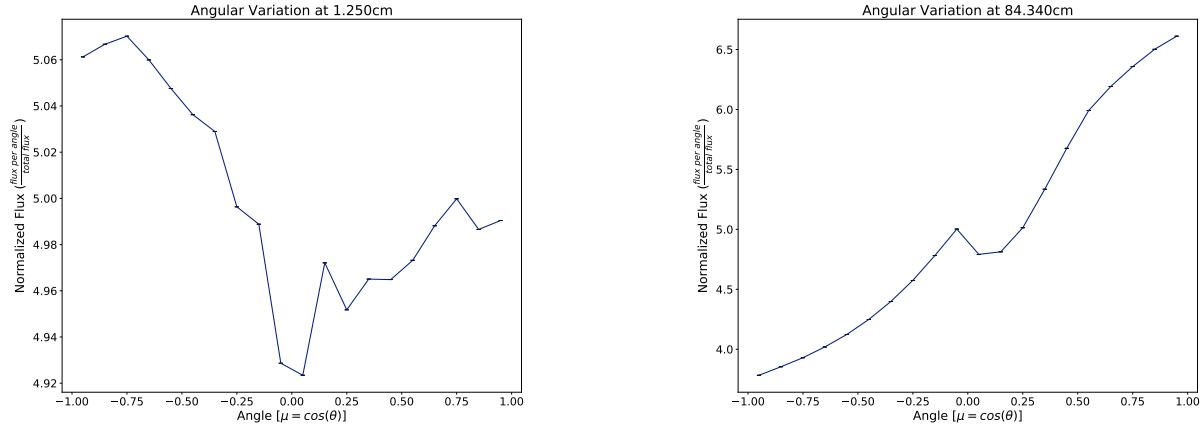


(g)

(h)

Figure 2-8. Energy spectrum of the neutron flux at various locations in the MPC where fuel rods are stored.

827 the results. Figure 2-9a shows the neutron flux is slightly inward-peaked 0.5cm from the
 828 centerline with 50.278% of all neutrons traveling toward the centerline. This indicates
 829 the flux can be approximated as isotropic near the centerline, a perfectly isotropic flux
 830 would have 50% of neutrons scattering toward the center of the fuel region. The flux at
 831 the outer edge has an outward peaked flux as shown in Fig. 2-9b. This is because the
 832 neutron population density is high in the fuel region, since the source of neutrons is in
 833 the fuel region, and neutrons are diffusing, or leaking, out of the fuel region where the
 834 neutron population density is lower. The percent of neutrons traveling outward from the
 835 fuel region 57.290% at the surface of the fuel region. While, the angular distribution in
 836 Fig. 2-9b shows the neutrons are slightly forward peaked, the angular distribution of the
 837 neutron flux deviates from isotropic by only $\sim 7\%$, thus, can be approximated as isotropic
 838 with the understanding that this approximation may lead to some disagreement between
 839 analytic and computational results.



(a)

(b)

Figure 2-9. Angular distribution of the neutron flux at 2-9a 0.50 cm and at 2-9b the inner surface of the MPC (84.34 cm) from the centerline of the fuel cask.

840 Figure 2-10 shows the mean-free-path (MFP) of each of the materials in the fuel
 841 region. The MFP is the average distance between neutron interactions in a material.
 842 Figure 2-10 shows the MFP in the fuel (blue), cladding (orange), helium (green), stainless
 843 steel (red), and neutron absorbing material (purple). The source flux is also shown in
 844 grey to identify which energy regions are most important (i.e., energy regions where the
 845 source flux is higher are more important). Assessing the MFP of each material helps to
 846 identify other assumptions and approximations that aid in determine the appropriate
 847 mathematical model to represent the neutron flux. The MFP of helium is about 1km
 848 where the source flux is most intense near 1MeV. The thickest region of helium occurs
 849 between the fuel cells and edge of the fuel region and is on the order of 10cm thick.
 850 The MFP is approximately two orders of magnitude larger, meaning there will be a
 851 negligible number of neutrons interacting in helium. The first material assumption is
 852 that helium outside of the fuel cells can be neglected. The remaining materials have a
 853 MFP of approximately 1cm at 1MeV. These materials show up in the fuel region on the
 854 same order, therefore, the remaining materials cannot be neglected. However, since these
 855 materials are evenly distributed (i.e., the materials exist throughout the fuel region and

856 not just at a single location) and since the remaining materials have similar MFP's, a
857 homogenization technique can be used to approximated the geometry in the fuel region.

858 A cylinder shaped homogenous fuel material is made based on the weight ratio of
859 each material in the fuel region. The volume of the homogenous cylinder of fuel material
860 is determined to preserve the volume from the 32 original fuel cells, and the radius of the
861 cylinder is approximately 75cm. The volume around the cylinder of homogenous fuel is
862 treated as a vacuum in the mathematical model. The radius of the homogenized fuel is
863 about two orders of magnitude greater than the MFP of the materials used in the fuel
864 region (e.q., $\sim 100\text{cm}$ radius of fuel $>> \sim 1\text{cm}$ MFP). Hence, the diffusion equation is
865 an appropriate model since the fuel material is much thicker than the neutron's MFP.
866 Therefore, the monoenergetic diffusion equation is an appropriate mathematical model to
867 represent the neutron flux in the fuel region, given the previous identified assumptions and
868 approximations derived from physical properties of materials in the fuel region.

869 A monoenergetic diffusion approximation is an appropriate choice of an analytic
870 model for the fuel region, however, that may not be the case for other materials in the
871 cask. It is important to identify how the flux behaves in the remaining materials of the
872 fuel cask and to identify appropriate models.

873 **2.2.2 Stainless Steel MPC**

874 The MPC encompasses the fuel area in a 2.5cm thick stainless steel 304 cylindrical
875 container. Figure 2-11 shows the MFP in stainless steel 304. The most important thing to
876 notice from the figure is that the MFP is on a similar order of magnitude as the thickness
877 of the MPC. The diffusion equation is not an appropriate model when a material's
878 thickness is fewer than a couple MFP's thick. Therefore, the diffusion approximation
879 is unlikely to be an appropriate mathematical model. Instead, the multigroup discrete
880 ordinates equation is a better approximation in this situation.

881 The number of energy groups and angles required to adequately model neutron
882 transport in the stainless steel is still needed. Analyzing the energy spectrum at the

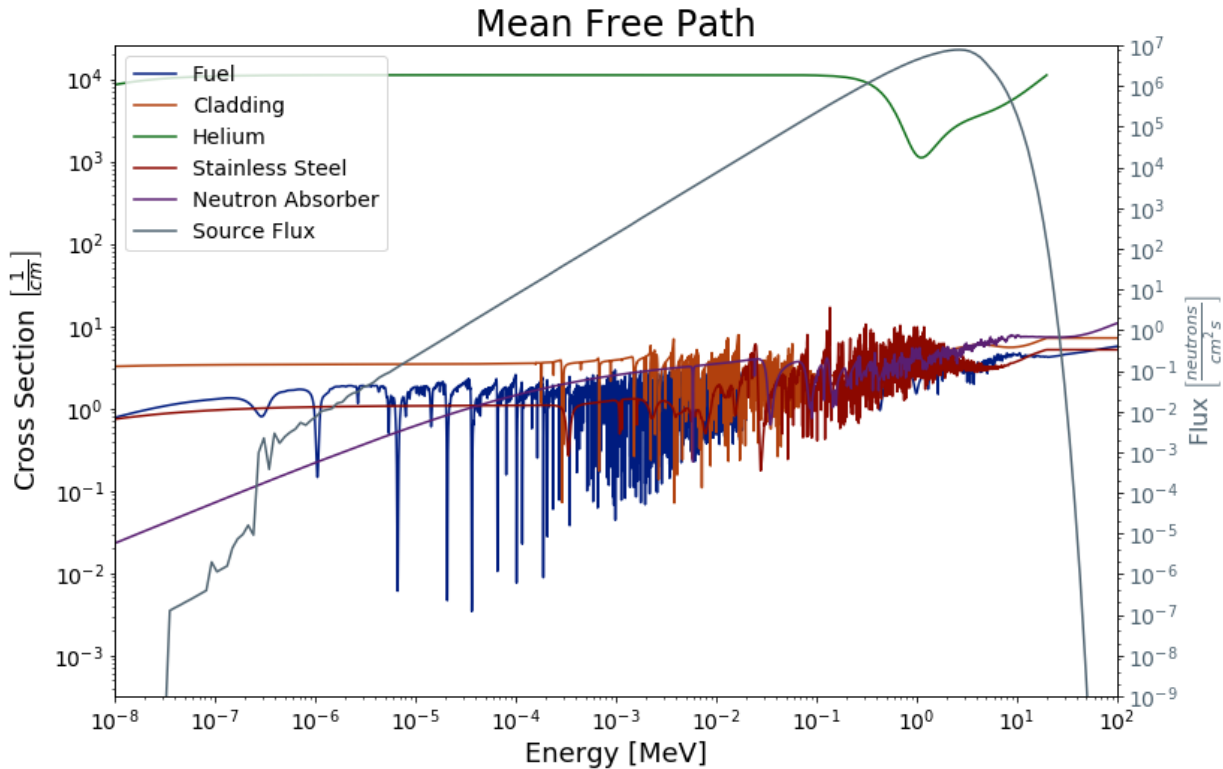


Figure 2-10. The mean-free-path, or distance between interactions, of the materials in the fuel region. The source flux is provided in order to identify energy ranges of greater importance.

883 interior and exterior surface of the MPC aid in finding an appropriate number of energy
 884 groups. Figure 2-12 shows the neutron energy spectrum at the interior surface (Fig. 2-12a)
 885 and exterior surface (Fig. 2-12b) of the MPC. At the interior surface of the MPC, the
 886 neutron flux is $\sim 70\%$ above 10keV and a single energy model would be appropriate. This
 887 would be preferable since the group structure in the MPC would match the energy group
 888 boundaries in the fuel region. However, the number of slow neutrons increases though
 889 the thickness of the MPC, and Fig. 2-12b shows that $\sim 59\%$ of neutrons are above 10keV.
 890 Hence, a two group analytic model is preferable.

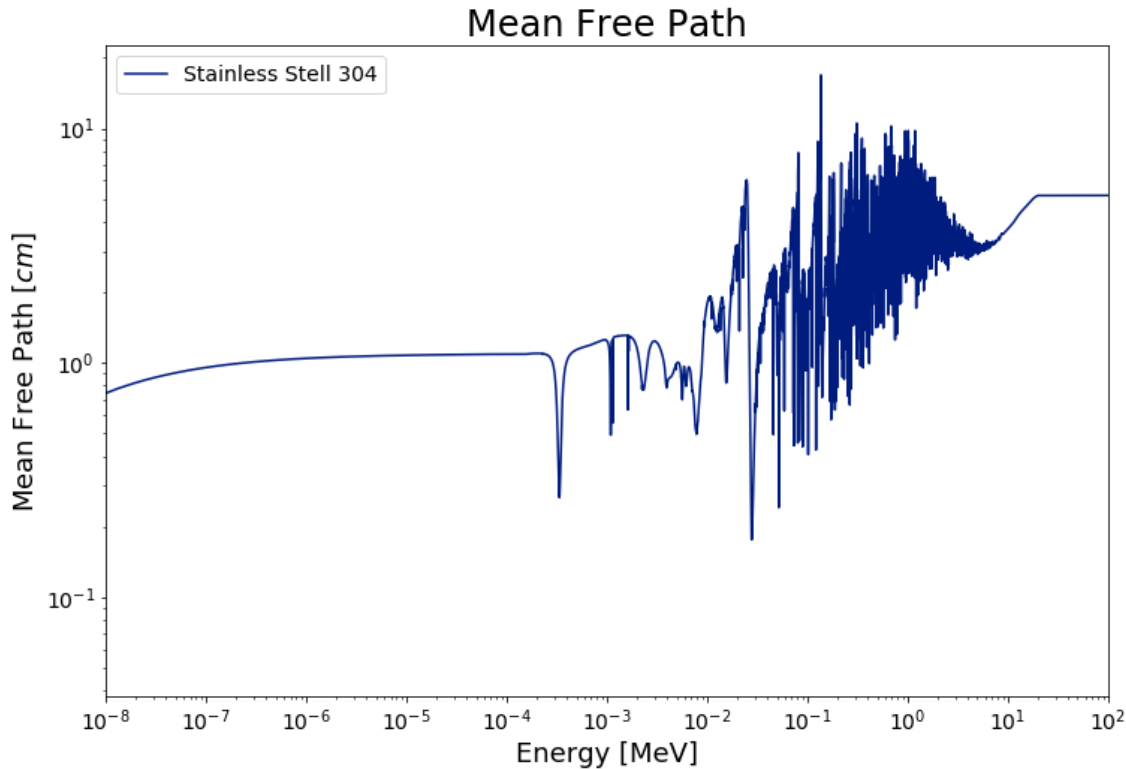


Figure 2-11. The mean-free-path of neutrons in stainless steel 304.

891 Analysis of the angular distribution (Fig. 2-13) helps to determine the number

892 of angles to use in the multigroup discrete ordinates approximation. Figure 2-13a is

893 the angular distribution of the flux at the interior surface of the MPC. Approximately

894 57% of the neutrons are forward scattering at this point in the MPC and Fig. 2-13b

895 shows that the number of forward scattered neutrons is relatively similar ($\sim 56\%$). In

896 the fuel region, the flux is considered isotropic even though over half of the neutrons are

897 traveling away from the centerline near the outer surface of the cask. This is an acceptable

898 approximation since there exists location in the fuel region that are closer to isotropic.

899 However, the neutron flux in the stainless steel is only forward-pointed, which alludes

900 to using two angles to approximate the neutron flux. Finally, the multigroup discrete

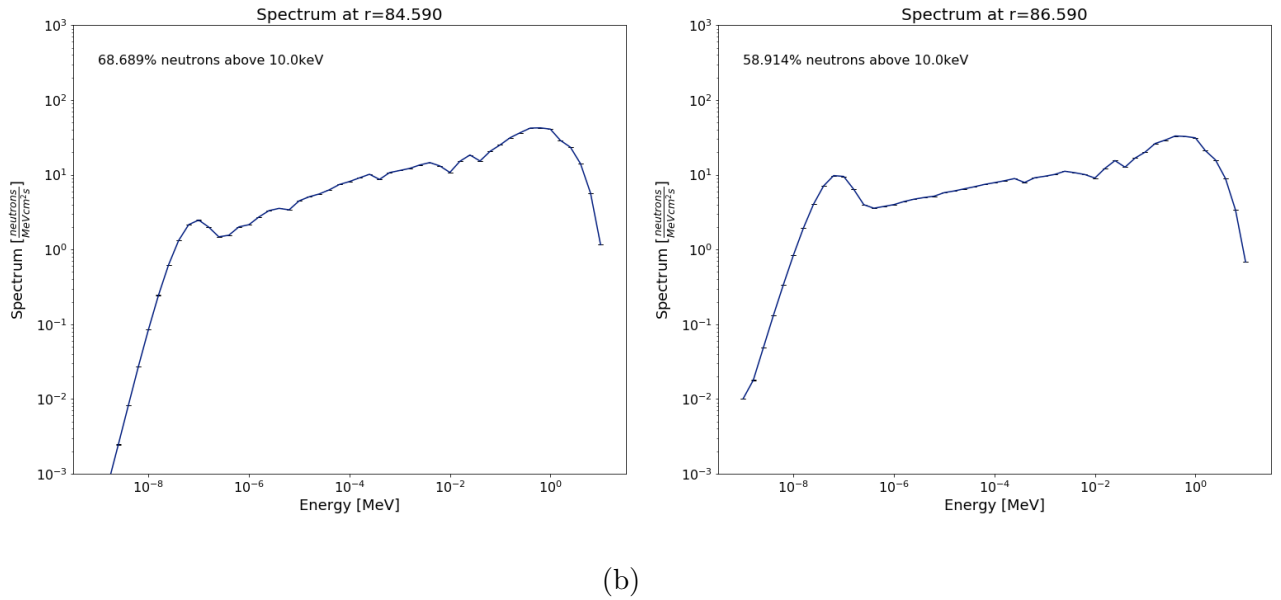


Figure 2-12. The neutron energy spectrum at a) 84.6cm and b) 86.6cm in the stainless steel MPC.

901 ordinates approximation with two energy groups and two angles is chosen to model
 902 neutron transport in the stainless steel.

903 2.2.3 Dry Air Gap

904 Surrounding the MPC is a gap of dry air for heat removal from the fuel. Figure 2-14
 905 shows the mean free path of neutrons in dry air. The MFP is two orders of magnitude
 906 larger than the thickness of the air gap ($\sim 10\text{cm}$). Meaning, the air gap can be treated as a
 907 vacuum and there is no need for a mathematical model in this region.

908 2.2.4 Concrete Annulus

909 The 71.12cm thick concrete annulus provides nearly half the neutron shielding
 910 capabilities in the spent fuel cask due to scattering on hydrogen. Following a similar
 911 method as before, the MFP of neutrons in concrete are investigated. Concrete, being
 912 a thermalizing material, is expected to change the neutron energy spectrum through
 913 down-scattering neutrons, so both fast and thermal energies need to be taken into account
 914 when analyzing Fig. 2-15. At higher energies, 1MeV, the concrete is about 7 MFP's thick.

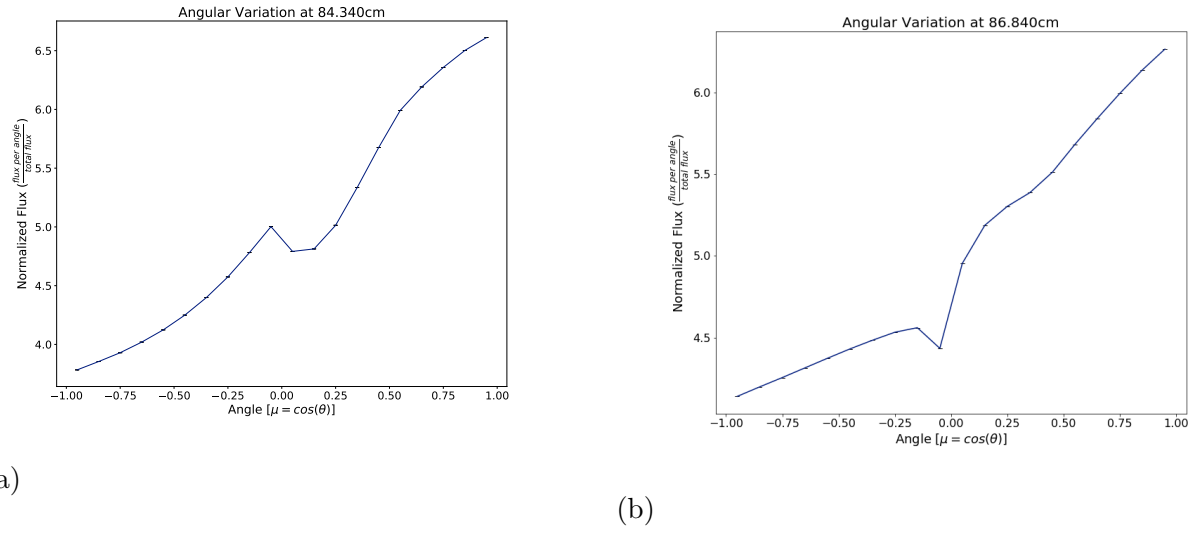


Figure 2-13. The neutron angular distribution at the a) inner surface and b) outer surface of the MPC.

915 Therefore, diffusion may not be an appropriate model for these energies of neutrons.
 916 However, at lower energies, 1eV, the concrete is about 35 MFP's thick. At lower energies,
 917 the diffusion approximation is an appropriate model. Overall, analysis of Fig. 2-15 would
 918 indicate that a multigroup discrete ordinates approximation would be better suited as
 919 an analytic model in the entire concrete. Further investigation of the neutron energy
 920 spectrum and angular distribution will aid in solidifying a model choice.

921 The energy spectrum does change significantly over the thickness of the concrete
 922 annuls. Figure 2-16a shows the neutron energy spectrum at the inside surface of the
 923 concrete annulus. The neutron flux is $\sim 53\%$ above 10keV at the innermost surface of the
 924 concrete. The neutron flux is quickly thermalized and less than a third of the neutron flux
 925 is above 10keV after the neutrons have traveled ten centimeters into the concrete (Fig.
 926 2-16b). At the exiting surface, less than 6% of the neutrons remain above 10keV as shown
 927 in Fig. 2-16h. The large change in neutron energies means more than one energy will be
 928 required to model transport in concrete. The shape of the flux shows the presence of two
 929 local maxima in the neutron spectrum that occur throughout the concrete region, one near

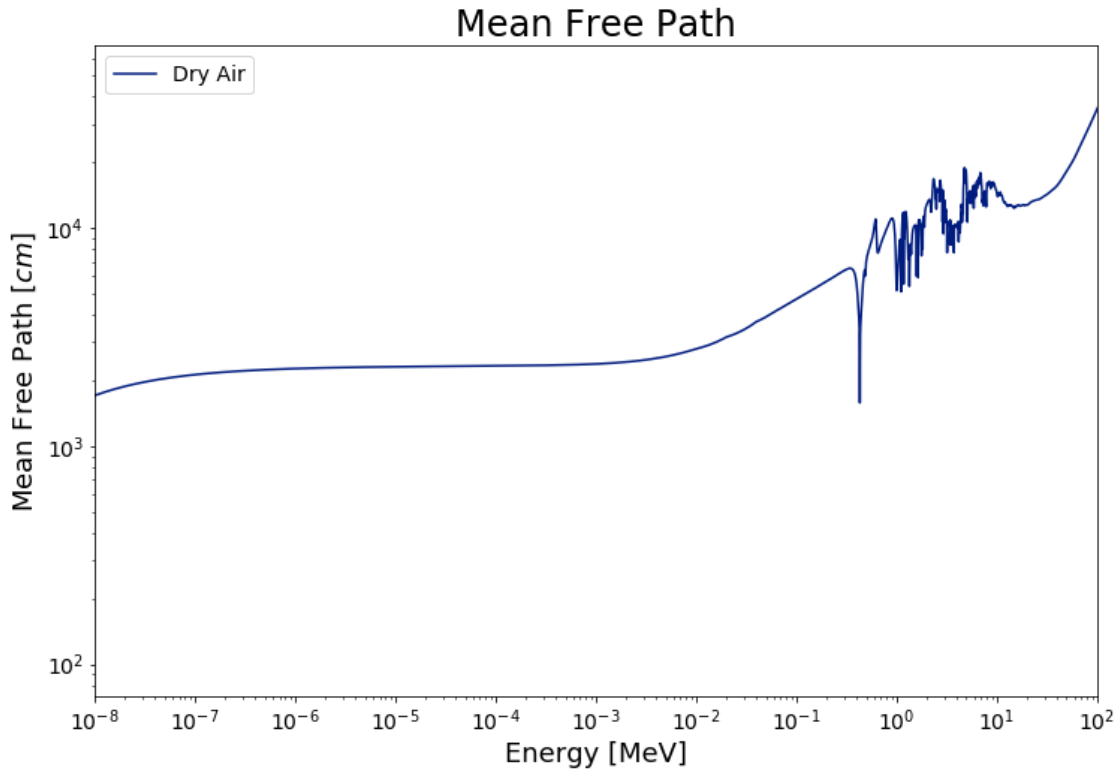


Figure 2-14. The mean-free-path of neutrons in the air gap. The low density of gaseous air lead to a high MFP. The air gap can be treated as a streaming region since the MFP is much larger than the thickness of the air gap.

930 1MeV and the other near 0.1eV. Therefore, a two energy group model is expected to be
 931 adequate. Analysis of the angular distribution will indicate the number of angles necessary
 932 for the multigroup discrete ordinates model.

933 Figure 2-17 show the angular distribution at the entering and exiting surfaces of
 934 the concrete annulus. Analysis of the angular distribution shows the neutron flux is
 935 forward-peaked with $\sim 55\%$ of the neutrons traveling outward at the inner surface of the
 936 concrete annulus. At the exiting surface, $\sim 68\%$ of the neutrons are traveling outward.

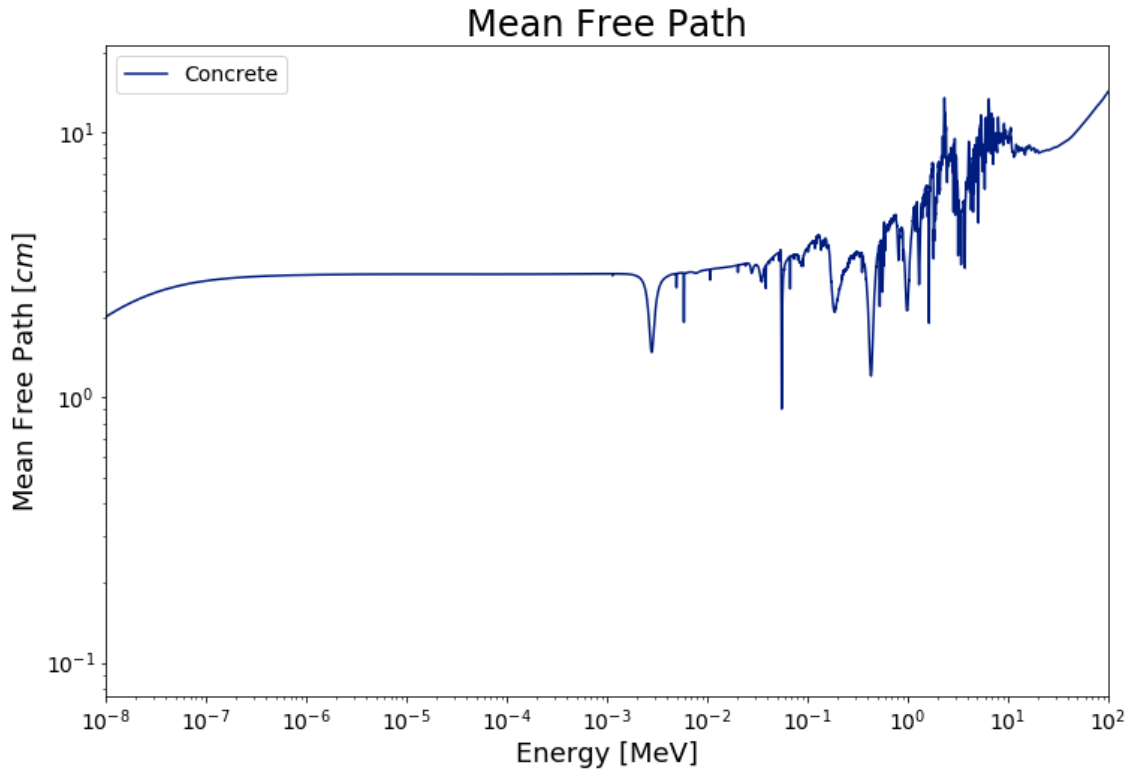


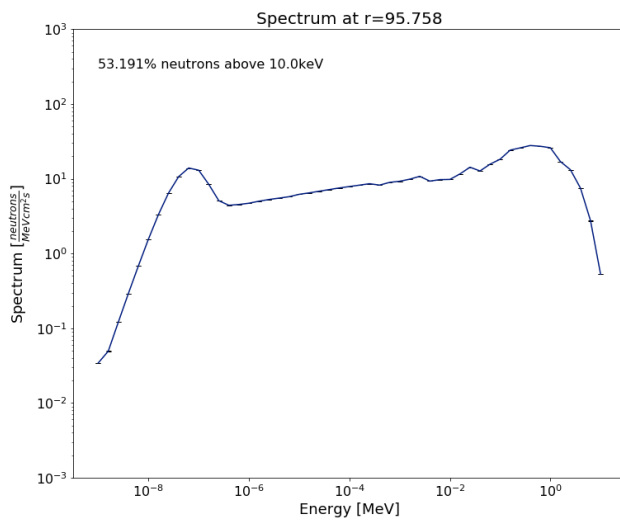
Figure 2-15. The mean-free-path of neutrons in the concrete annulus.

937 This results confirms the model choice of the multigroup discrete ordinates approximation.

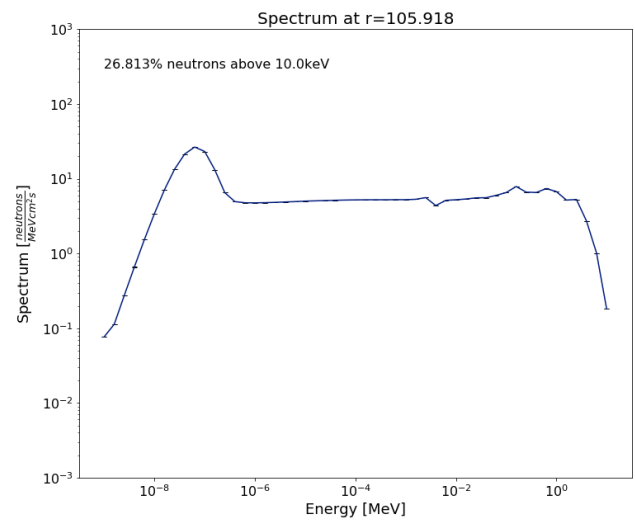
938 Further, two angles are adequate to describe the flux to a first-order-approximation.

939 **2.2.5 Carbon Steel Outer Shell**

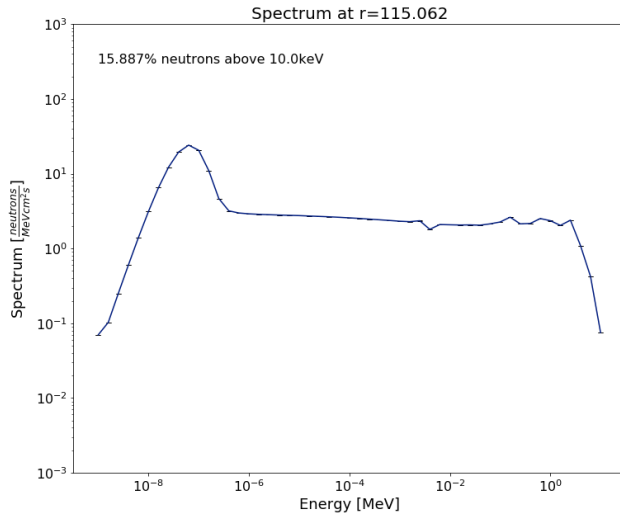
940 The 1.905cm thick carbon steel shell is the final material being analyzed in the spent
 941 fuel cask. Using a similar analysis as with previous materials, the MFP is compared
 942 to the thickness of the steel shell to aid in determining a mathematical model. Figure
 943 2-18 shows the MFP of neutrons in carbon steel. The most probable energy of neutrons
 944 leaving entering the carbon steel shell is about 0.1MeV, shown in Fig. 2-16h. Using this
 945 information, the most probable MFP of neutrons in the carbon steel shell is \sim 1cm. This is
 946 on the order of the magnitude of the carbon steel shell thickness. Therefore, the diffusion



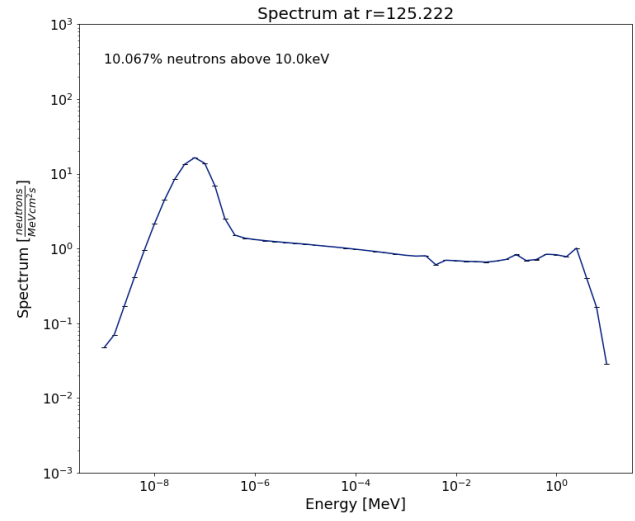
(a)



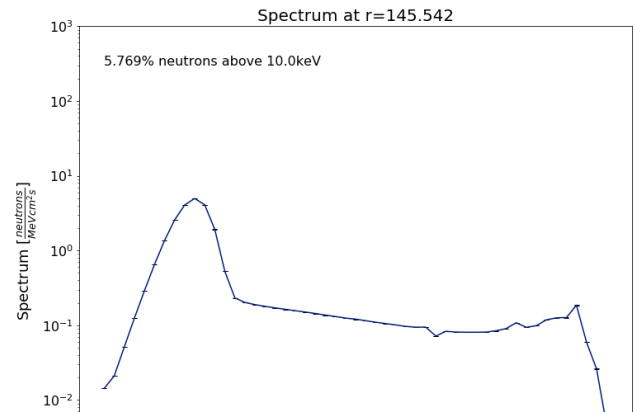
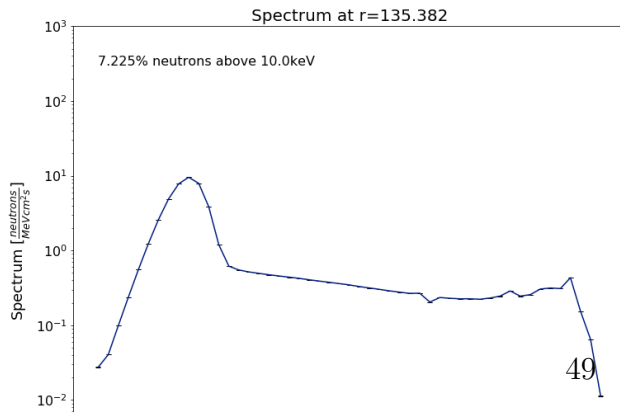
(b)

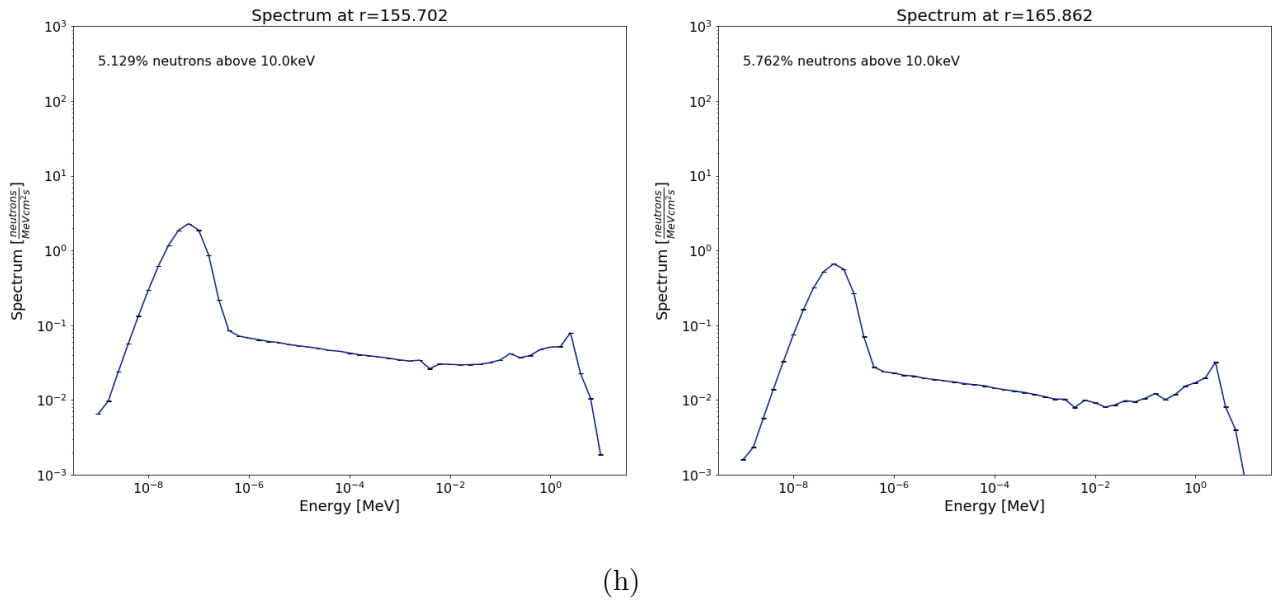


(c)



(d)





(g) (h)

Figure 2-16. Energy spectrum of neutrons throughout the concrete annulus.

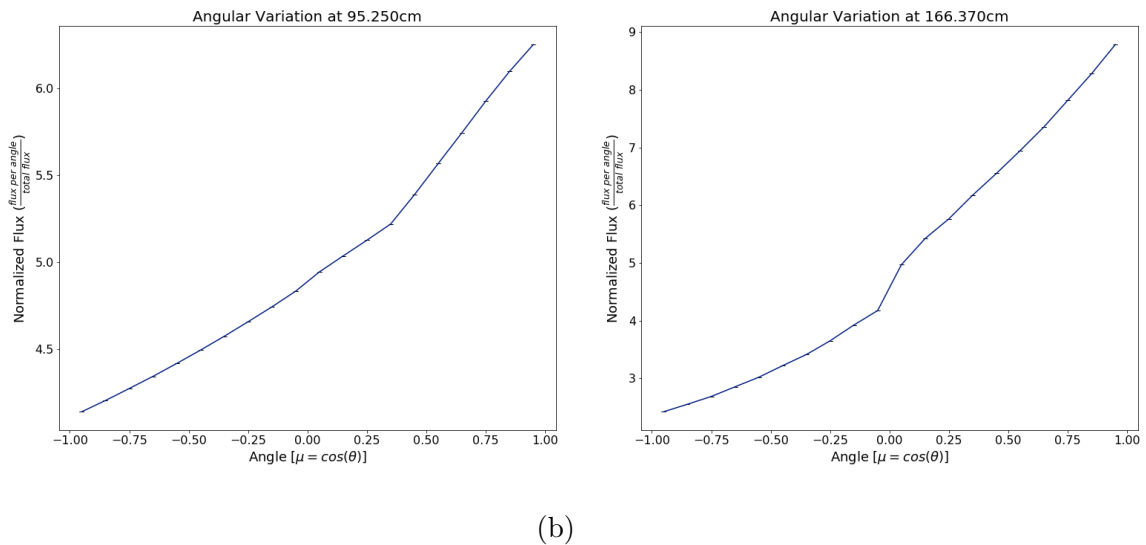


Figure 2-17. The angular distribution of the neutron flux at a) the inner surface (95.25cm) and the b) outer surface (166.37cm) of the concrete annulus.

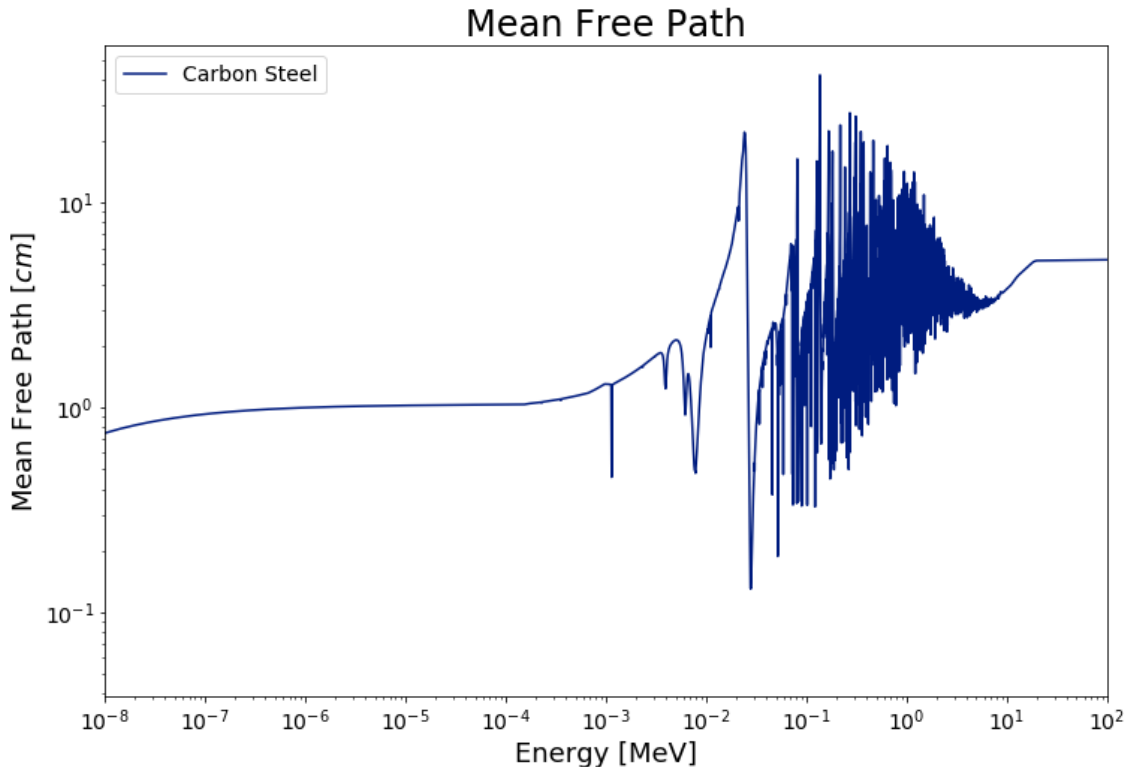


Figure 2-18. The mean-free-path of neutrons in carbon steel.

947 equation is likely a poor choice of mathematical model and the multigroup discrete
 948 ordinates equation is likely a better choice.

949 Figure 2-19 shows the energy spectrum at the inner surface (Fig. 2-19a) and outer
 950 surface (Fig. 2-19b). A small number of neutrons are bred in carbon steel resulting in
 951 the growing number of neutrons above 10keV. For this reason, two energy groups should
 952 be used to model the neutron flux in the carbon steel.

953 Finally, the angular distribution graphs of the neutron flux entering the carbon steel
 954 (Fig. 2-20a) and leaving the carbon steel shell (Fig. 2-20b) show the neutron flux is
 955 forward peaked. In fact, at the inner carbon steel surface $\sim 68\%$ of the flux is traveling
 956 outward and that fraction increases to $\sim 97\%$ of neutrons traveling outward at the exiting

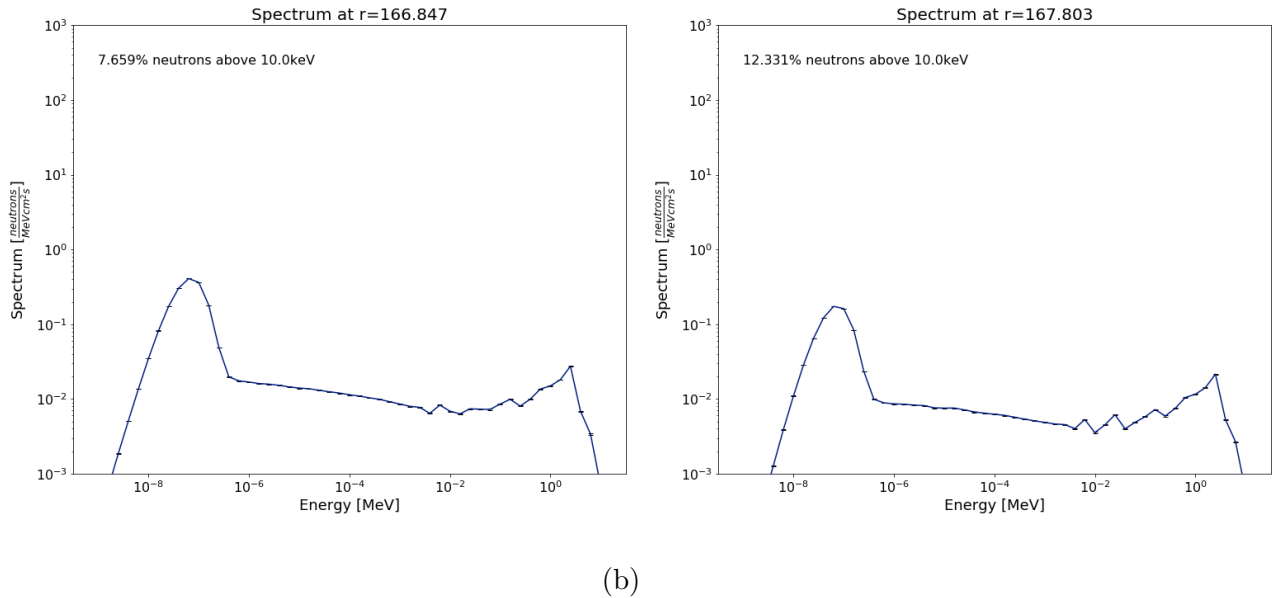


Figure 2-19. The neutron energy spectrum near the a) inner surface (166.847cm) and the b) outer surface (167.803cm) of the carbon steel shell. The two peaks in each figure allude to a two energy group model.

957 surface of the cask. Nearly all of the neutrons are traveling away from the cask because
 958 the cask is placed in dry air. As shown previously, the MFP of neutrons in dry air is large,
 959 greater than 1km, resulting in a small number of neutrons returning to the cask after
 960 leaving. The small number of returning neutrons provides boundary condition information
 961 for the final model. Therefore, the outermost boundary of the spent fuel cask can be
 962 treated as non-reentrant. Further, two angular groups are capable of approximating the
 963 flux since the distribution is strongly preferential in a forward direction.

964 By no means are the previous choices in analytic models meant to be the most
 965 exhaustive means of describing the neutron flux in each material. Rather, choices were
 966 made in order to keep the models as simplistic as possible while capturing the physics
 967 of the spent fuel cask in an attempt to highlight inherent phenomenon in the problem.
 968 As will be seen during the sensitivity analysis portion of the work, even these simplistic
 969 models yield complex sensitivity results. Therefore, identifying any physical meaning using

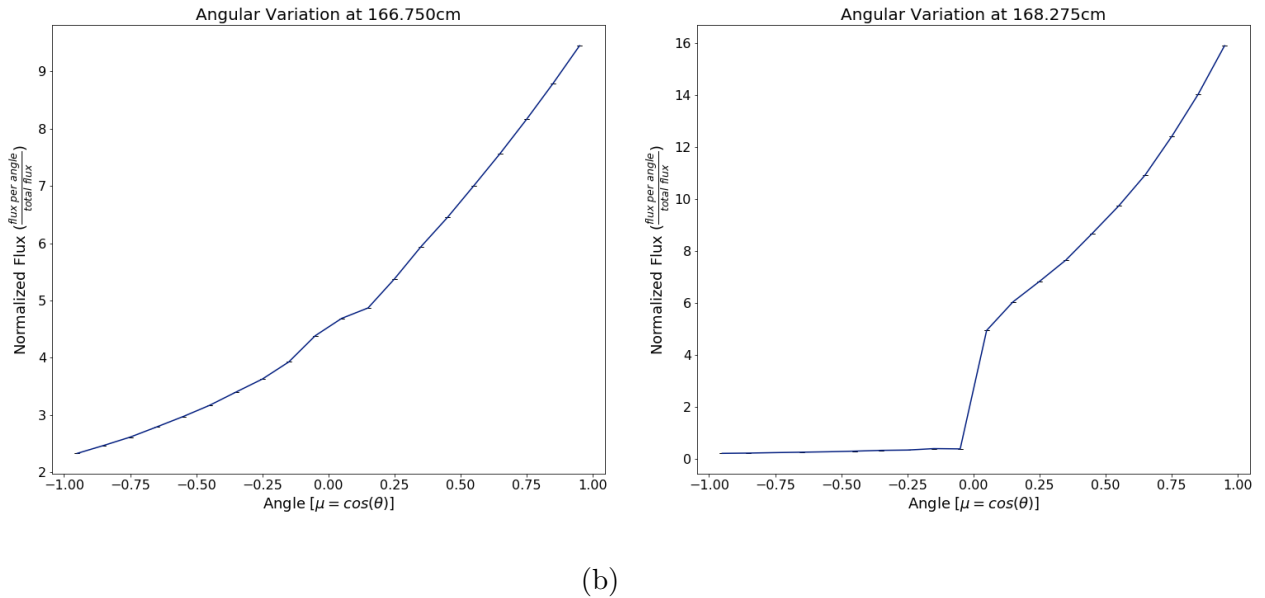


Figure 2-20. The angular distribution of the neutron flux at the a) inner surface and b) outer surface of the carbon steel shell. Since the flux is heavily forward-pointed, two directions can be used to model the flux.

970 the analytic models becomes challenging, if possible, even when using very simple models.
 971 While the mathematical models have been chosen, the geometry which each will be solved
 972 in has yet to be determined, which will be discussed in Chp. 3.

973 2.3 Identification of Features

974 “Features” are locations in the simulated neutron flux spatial distribution shown in
 975 Fig. 2-7 which appear to be the result of a physical process. Using a reduced complexity
 976 analytic or computational model to reproduce a feature yields two benefits: 1) the physical
 977 process that generates the feature in question is identified and, 2) confidence is gained in
 978 the accuracy of the simulation result. Confidence in the simulation result is gained when
 979 a feature is determined to be a result of an understood physical process. That is, the
 980 feature should exist in the problem, is being modeled correctly in the code, and is not a
 981 computational artifact. Ensuring agreement between simplified and complex models also
 982 corroborates the accuracy of the simulation input itself. Something as simple as inputting

983 an incorrect area or volume would not result in a fatal error message in MCNP, but would
984 lead to incorrect neutron flux results. The process of reproducing features using simplified
985 analytic and computational models provides an opportunity to identify errors in the
986 simulation input and addressing these errors leads to increased confidence in the accuracy
987 of a simulation.

988 There are five features discussed in this paper which are identified as:

- 989 1. The “flat” flux region (highlighted in Fig. 2-21): The flux in this region smoothly
990 decreases by approximately 36% even though intuition suggests the flux should
991 increase in the fuel pins and decrease in the space between fuel pins.
- 992 2. The abrupt level-off region (highlighted in Fig. 2-22): The flux only decreases $\sim 3\%$
993 over the region $65\text{ cm} \leq r \leq 84.1\text{ cm}$ from the cask centerline.
- 994 3. Periodic depressions (highlighted in Fig. 2-23): There is a $\sim 2\%$ reduction in the flux
995 near 25 cm, 50 cm, and 75 cm from the cask centerline.
- 996 4. The asymmetric flux: Figure 2-24 is a density plot of the neutron flux when looking
997 at a center slice of the cask from above. Figure 2-25 is a contour plot to better
998 illustrate the neutron flux asymmetry present in Fig. 2-24. The neutron flux in the
999 upper left section (above the diagonal line) of the plot is less than the neutron flux
1000 in the lower right section (below the diagonal line) of the image. This asymmetry is
1001 most obvious at the outer edge of the fuel region.
- 1002 5. The concrete flux (Fig. 2-26): The concrete region provides the second-most
1003 significant reduction in the neutron flux within the cask. Identifying the processes
1004 which attenuate radiation in this region provides evidence the overpack was modeled
1005 correctly.

1006 The remaining chapters will discuss how the results assessment methodology is used
1007 to identify the salient physics in each of the previously identified features, as well as, how
1008 confidence is gained in the simulation results of the detailed model through sensitivity
1009 analysis. However, the next chapter will provide an in-depth background on neutron

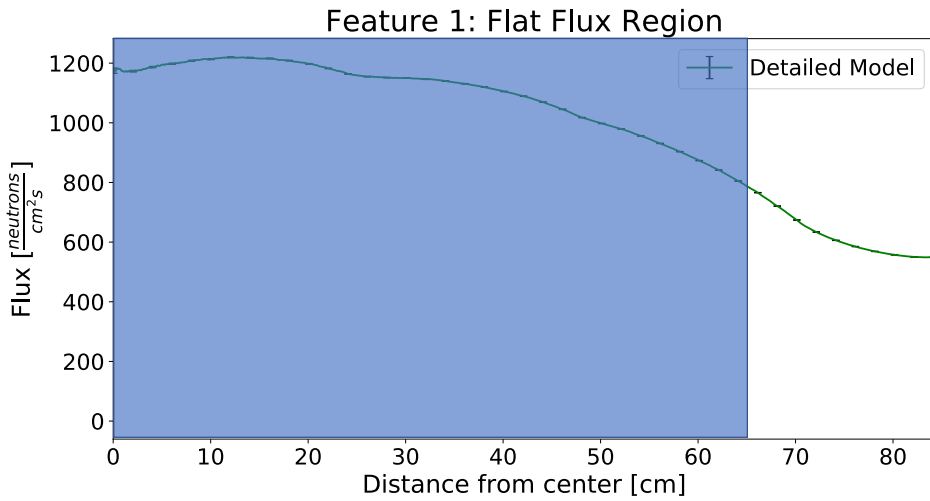


Figure 2-21. The neutron flux spatial distribution between the cask centerline and inner face of the MPC. The highlighted region is considered the flat flux region. This neutron flux is relatively flat and does not vary on the same order as the physical dimensions of materials in this region.

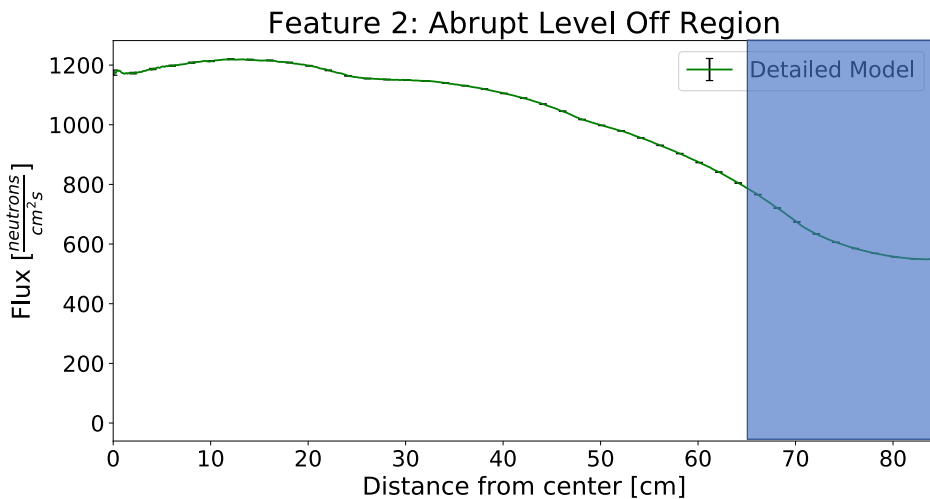


Figure 2-22. The flux stops decreasing and instead levels-off in the abrupt level-off region. The flux decreases less than 3% over the last ten centimeters before the interface between the fuel region and MPC.

¹⁰¹⁰ transport theory and the development of the analytic models which will be used in the

¹⁰¹¹ analysis before we can discuss the features further.

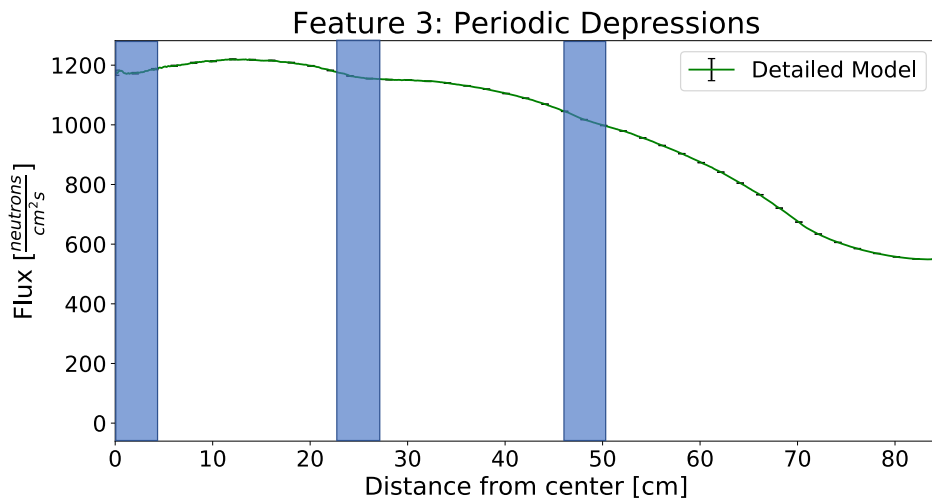


Figure 2-23. There are three depressions in the neutron flux spatial distribution located approximately 22 cm apart. The flux decreases about 2% at each depression.

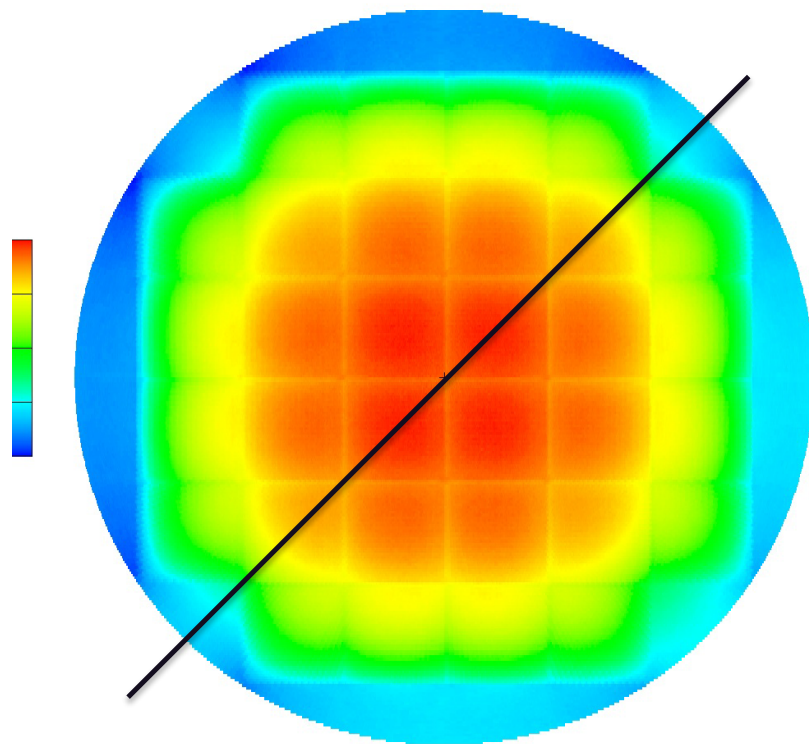


Figure 2-24. A density plot of the neutron flux at a "central slice" of the fuel cask as viewed from above. This plot shows the neutron flux is less in the upper left section than in the lower right section. The asymmetry is most evident in the blue and light blue sections at the outer radius of the figure.

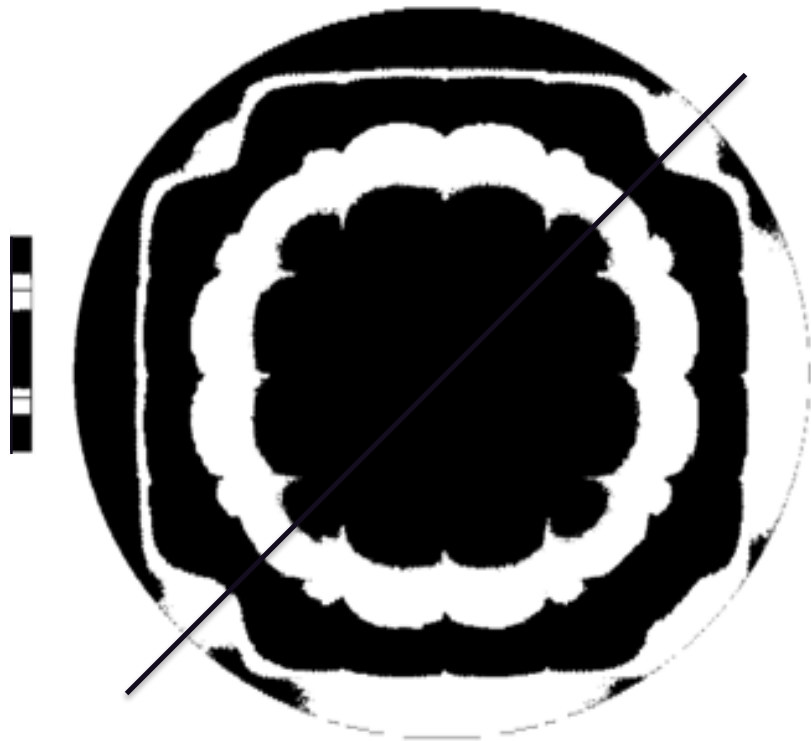


Figure 2-25. A contrast plot emphasizing the asymmetry of the flux values.

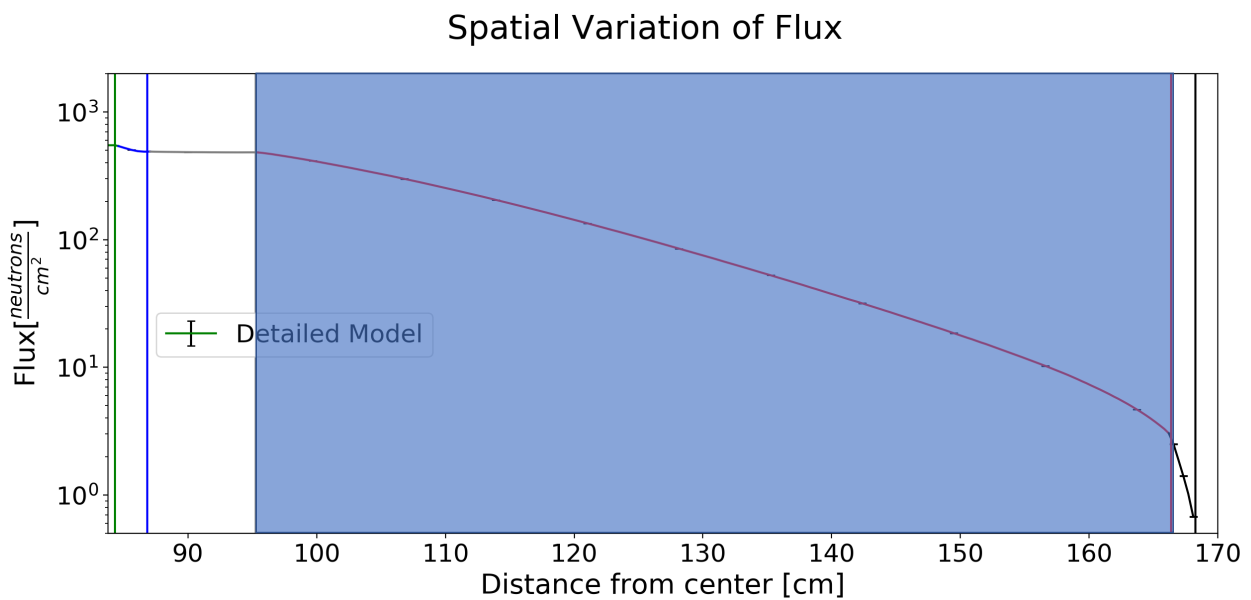


Figure 2-26. The overpack accounts for about half of the reduction to the neutron flux. The purpose of investigating this region is to determine which physical processes are responsible for the attenuation.

1012
1013

CHAPTER 3 THEORY

1014 The behavior of any nuclear system is governed by the distribution of radioactive
1015 particles within the system. In the case of a system containing neutrons, the distribution
1016 of neutrons can be found by solving the neutron transport equation (NTE). The NTE
1017 is also referred to as the Boltzmann transport equation because of its similarity to
1018 Boltzmann's equation governing the kinetic theory of gas. Finding an analytic solution
1019 of the NTE for even the simplest geometries is a challenging task. Not only because the
1020 equation is an integro-differential equation defined over a seven variable phase space, but
1021 also because the solution of the NTE depends on parameters which are heavily dependent
1022 on the solution to the original equation. The NTE can be solved for the flux by applying
1023 assumptions and approximations to reduce the complexity of the equation. The NTE
1024 is derived before applying assumptions and simplifications to reduce the NTE into two,
1025 distinct tractable approximations; known as (1) the diffusion approximation and (2) the
1026 multigroup discrete ordinates equations.

Before deriving the NTE, it is important to define terms which will be used. The neutron angular density,

$$N(\mathbf{r}, \hat{\Omega}, E, t),$$

describes the expected number of neutrons in the region of phase space defined by a neutron's position vector \mathbf{r} , direction of travel $\hat{\Omega}$, and kinetic energy E at time t . It follows that the expected number of neutrons at time t in a volume element dV having energies in dE about E and directions within a narrow beam $d\hat{\Omega}$ about $\hat{\Omega}$ can be described by

$$N(\mathbf{r}, \hat{\Omega}, E, t) dV d\hat{\Omega} dE.$$

The angular flux is defined as the product of speed v and the number of neutrons,

$$\varphi(\mathbf{r}, \hat{\Omega}, E, t) = vN(\mathbf{r}, \hat{\Omega}, E, t).$$

Using the angular flux, the reaction rate is defined as

$$R_x(\mathbf{r}, \hat{\Omega}, E, t) = \Sigma_x(E) \varphi(\mathbf{r}, \hat{\Omega}, E, t)$$

1027 where $R_x(\mathbf{r}, \hat{\Omega}, E, t)$ is the frequency of interactions between neutrons and surrounding
 1028 materials. The parameter $\Sigma_x(E)$ called the macroscopic cross section for reaction “x”
 1029 (e.g., total reaction cross section, absorption cross section, scattering cross section). The
 1030 macroscopic cross section describes the probability of an interaction occurring per unit
 1031 length as a function of incoming neutron energy.

1032 **3.1 Derivation of the Boltzmann Transport Equation for Neutrons by
 1033 Derivatives**

1034 The NTE can be derived by “following” a group of neutrons, referred to as a packet,
 1035 through a material and describe how neutrons are gained or lost in time. Neutrons with
 1036 energy E are lost from the packet as a result of a collision over the distance $v\Delta t$, whereas
 1037 neutrons that do not interact over the distance $v\Delta t$ remain in the packet. The probability
 1038 of a neutron being removed from the packet over the distance $v\Delta t$ can then be written as

$$\begin{aligned} \text{Probability of a neutron} & \equiv \Sigma_t(\mathbf{r}, E)v\Delta t, \\ \text{being removed from the packet} & \end{aligned} \quad (3-1)$$

1039 and the probability of a neutron remaining in the packet over the distance $v\Delta t$ is defined
 1040 as

$$\begin{aligned} \text{Probability of a neutron} & \equiv 1 - \Sigma_t(\mathbf{r}, E)v\Delta t. \\ \text{remaining in the packet} & \end{aligned} \quad (3-2)$$

1041 Using 3-2, the number of neutrons remaining in the packet after traveling a small
 1042 distance of $v\Delta t$ is

$$\begin{aligned} \text{Number of neutrons} & \equiv N(\mathbf{r}, \hat{\Omega}, E, t)[1 - \Sigma_t(\mathbf{r}, E)v\Delta t] dV d\hat{\Omega} dE. \\ \text{remaining in packet} & \end{aligned} \quad (3-3)$$

1043 Eqn. 3-3 adjusts the neutron population accounting for neutrons which left the packet
 1044 through interactions, however, neutrons can enter the packet through two mechanisms: 1)
 1045 internal neutron source or 2) by scattering from one packet into another. The number of

¹⁰⁴⁶ neutrons which enter the packet from an internal neutron source is given by

$$\begin{aligned} \text{Number of neutrons entering} \\ \text{packet from internal sources} &\equiv s(\mathbf{r}, \hat{\Omega}, E, t) dV d\hat{\Omega} dE \Delta t. \end{aligned} \quad (3-4)$$

Neutrons can also enter the packet through scattering interactions, called inscattering. An inscattering reaction occurs when a neutron belonging to the packet described by a volume element dV with energies in dE' about E' and directions within $d\hat{\Omega}'$ about $\hat{\Omega}'$ undergoes a scattering event leaving the neutron traveling in $d\hat{\Omega}$ about $\hat{\Omega}$ with energy in dE about E , adding this neutron to the packet $(\mathbf{r}, \hat{\Omega}, E, t)$. The probability of neutrons with energy E' and direction $\hat{\Omega}'$ which scatter into the energy $E + dE$ with direction in $\hat{\Omega} + d\hat{\Omega}$ can be written as:

$$\begin{aligned} \text{Probability of neutrons entering} \\ \text{packet due to inscattering} &\equiv \Sigma_s(\mathbf{r}, \hat{\Omega}' \rightarrow \hat{\Omega}, E' \rightarrow E, t) v N(\mathbf{r}, \hat{\Omega}', E', t). \end{aligned} \quad (3-5)$$

Integrating definition 3-5 over all initial energies dE' and initial directions $d\hat{\Omega}'$ yields the number of neutrons that enter the packet due to inscattering,

$$\begin{aligned} \text{Number of neutrons entering} \\ \text{packet due to inscattering} &\equiv \\ \left[\int_{4\pi} d\hat{\Omega} \int_0^\infty dE \Sigma_s(\mathbf{r}, \hat{\Omega}' \rightarrow \hat{\Omega}, E' \rightarrow E, t) v N(\mathbf{r}, \hat{\Omega}', E', t) \right] dV d\hat{\Omega} dE \Delta t. \end{aligned} \quad (3-6)$$

The neutron density at $\mathbf{r} + \hat{\Omega} v \Delta t$ at time $t + \Delta t$ is found by adding 3-3, 3-4, and 3-6 and dividing that sum by $dV d\hat{\Omega} dE$:

$$\begin{aligned} N(\mathbf{r} + \hat{\Omega} v \Delta t, \hat{\Omega}, E, t + \Delta t) = \\ N(\mathbf{r}, \hat{\Omega}, E, t) (1 - \Sigma_t v \Delta t) \\ + \left[\int_{4\pi} d\hat{\Omega}' \int_0^\infty dE' \Sigma_s(\mathbf{r}, \hat{\Omega}' \rightarrow \hat{\Omega}, E' \rightarrow E, t) N(\mathbf{r}, \hat{\Omega}', E', t) \right] \Delta t + S \Delta t. \end{aligned} \quad (3-7)$$

Dividing Eqn. 3-7 and taking the limit as $\Delta t \rightarrow 0$ yields the result, after rearranging terms,

$$\begin{aligned} \lim_{\Delta t \rightarrow 0} \left[\frac{N(\mathbf{r} + \hat{\boldsymbol{\Omega}} v \Delta t, \hat{\boldsymbol{\Omega}}, E, t + \Delta t) - N(\mathbf{r}, \hat{\boldsymbol{\Omega}}, E, t)}{\Delta t} \right] + \Sigma_t v N(\mathbf{r}, \hat{\boldsymbol{\Omega}}, E, t) \\ = \int_{4\pi} d\hat{\boldsymbol{\Omega}}' \int_0^\infty dE' \Sigma_s(\mathbf{r}, \hat{\boldsymbol{\Omega}}' \rightarrow \hat{\boldsymbol{\Omega}}, E' \rightarrow E, t) N(\mathbf{r}, \hat{\boldsymbol{\Omega}}', E', t) + S. \end{aligned} \quad (3-8)$$

1047 Simplifying the first term requires adding and subtracting $N(\mathbf{r}, \hat{\boldsymbol{\Omega}}, E, t + \Delta t)$ to the
1048 second term in the numerator of the fraction in Eqn. 3-8 and simplifying the expressions
1049 individually. Adding $N(\mathbf{r}, \hat{\boldsymbol{\Omega}}, E, t + \Delta t)$ to the second term in the numerator gives

$$\lim_{\Delta t \rightarrow 0} \left[\frac{N(\mathbf{r}, \hat{\boldsymbol{\Omega}}, E, t + \Delta t) - N(\mathbf{r}, \hat{\boldsymbol{\Omega}}, E, t)}{\Delta t} \right] = \frac{\partial N}{\partial t}. \quad (3-9)$$

Subtracting $N(\mathbf{r}, \hat{\boldsymbol{\Omega}}, E, t + \Delta t)$ from the first term in the numerator leads to a less trivial expression, but it is more readily derived when decomposed in Cartesian coordinates as

$$\begin{aligned} \lim_{\Delta t \rightarrow 0} \frac{N(\mathbf{r} + \hat{\boldsymbol{\Omega}} v \Delta t, \hat{\boldsymbol{\Omega}}, E, t) - N(\mathbf{r}, \hat{\boldsymbol{\Omega}} E, t + \Delta t)}{\Delta t} = \\ \lim_{\Delta t \rightarrow 0} \frac{N(x + \Omega_x v \Delta t, y + \Omega_y v \Delta t, z + \Omega_z v \Delta t, \hat{\boldsymbol{\Omega}}, E, t) - N(x, y, z, \hat{\boldsymbol{\Omega}}, E, t)}{\Delta t}, \end{aligned} \quad (3-10)$$

where \mathbf{r} and $\hat{\boldsymbol{\Omega}}$ have components x, y, z and $\Omega_x, \Omega_y, \Omega_z$ respectively. The infinitesimal $\hat{\boldsymbol{\Omega}} v \Delta t$ is equivalent to Δx . Equation 3-10 is then solved using the chain rule.

$$\begin{aligned} \lim_{\Delta t \rightarrow 0} \frac{N(x + \Delta x, y + \Delta y, z + \Delta z) - N(x, y, z)}{\Delta t} = \\ \frac{\Delta N}{\Delta x} \frac{\Delta x}{\Delta t} + \frac{\Delta N}{\Delta y} \frac{\Delta y}{\Delta t} + \frac{\Delta N}{\Delta z} \frac{\Delta z}{\Delta t} = \\ v \Omega_x \frac{\partial N}{\partial x} + v \Omega_y \frac{\partial N}{\partial y} + v \Omega_z \frac{\partial N}{\partial z} = v \hat{\boldsymbol{\Omega}} \cdot \nabla N \end{aligned} \quad (3-11)$$

1050 Inserting the results of Eqn. 3-9 and Eqn. 3-11 into Eqn. 3-8, and using the definition
1051

$$\varphi(\mathbf{r}, \hat{\boldsymbol{\Omega}}, E, t) \equiv N(\mathbf{r}, \hat{\boldsymbol{\Omega}}, E, t) v \quad (3-12)$$

yields the NTE,

$$\frac{1}{v} \frac{\partial \varphi}{\partial t} + \hat{\Omega} \cdot \nabla \varphi + \Sigma_t \varphi(\mathbf{r}, \hat{\Omega}, E, t) = \int_{4\pi} d\hat{\Omega}' \int_0^\infty dE' \Sigma_s(\mathbf{r}, \hat{\Omega}', E', t) \varphi(\mathbf{r}, \hat{\Omega}', E', t) + S(\mathbf{r}, \hat{\Omega}, E, t). \quad (3-13)$$

1052 3.1.1 External Neutron Sources

1053 Discussion of external sources is precluded in the previous section since external
1054 source can be handled has boundary conditions when solving for the neutron flux.
1055 However, it is important to take a moment to discuss internal source as many texts
1056 simply introduce internal source, but provide little further discussion.

1057 A brief dimensional analysis can provide insight into how source terms are defined
1058 in the NTE. Since the neutron transport equation describes the number of neutrons in
1059 a volume at a point in time, then the units must be $\frac{\text{neutrons}}{\text{Length}^3 \text{Time}}$, or in SI units $\frac{\text{neutrons}}{\text{cm}^3 \text{s}}$.
1060 This is easily confirmed by checking the units of one term in Eqn. 3-13. Analyzing the
1061 dimensions of the interaction term,

$$\Sigma_t \varphi(\mathbf{r}, \hat{\Omega}, E, t) \equiv \left[\frac{1}{\text{Length}} \right] \left[\frac{\text{neutrons}}{\text{Length}^2 \text{Time}} \right] = \left[\frac{\text{neutrons}}{\text{Length}^3 \text{Time}} \right], \quad (3-14)$$

1062 which confirms the previous statement. Therefore, any source term must have these same
1063 units.

1064 Neutron sources can be categorized into two types: 1) flux-driven sources and 2)
1065 decay reactions. The distinction is made by how the source strength, or the number of
1066 neutrons per volume per unit time, varies with the radiation flux. In flux-driven sources,
1067 the source strength changes proportionally with the radiation flux. That is because these
1068 sources produce neutrons through reactions that occur when radiation interacts with
1069 the target nucleus and produces neutrons. Decay reaction sources do not depend on the
1070 neutron flux. Instead, these decay reactions, or simply decays, occur when a nucleus is left
1071 in an unstable energy state, typically resulting from some other nuclear reaction. These
1072 nuclei need to release energy in order to arrive at a stable energy state. Occasionally,

1073 nuclei get rid of excess energy by ejecting one or more neutrons. Flux-driven sources are
 1074 handled as boundary conditions when solving the mathematical models. Decay reaction
 1075 sources show up as the source term, S , in the diffusion approximation.

1076 **3.2 Reduction of NTE**

1077 Upon inspection of Eqn. 3-13, there are four derivatives on the left-hand side of the
 1078 equation (one in time and three spatial derivatives) and three integrals on the right-hand
 1079 side of the equation (one in energy and two in direction). Equations containing both
 1080 integrals and derivatives are called integro-differential equation and are among the
 1081 hardest forms of problems to solve. Further, the NTE is a function of seven variables;
 1082 three spatial, two direction, one energy, and one time. In its current form, the NTE has
 1083 no complete analytic solution. Therefore, assumptions and approximations are applied
 1084 to reduce Eqn. 3-13 into a tractable form. The following sections will discuss how the
 1085 multigroup discrete ordinates equation and the 1-D planar diffusion approximation are
 1086 derived from the NTE.

1087 **3.2.1 Treatment of Time Dependence**

1088 The time dependence is contained in the first term in Eqn. 3-13. Assuming the
 1089 neutron flux is unchanging or slowly changing in time will simplify the time-derivative to
 1090 zero. This is a fair assumption since the time between neutron interactions is much smaller
 1091 than the time over which the neutron flux is evolving [37]. In this assumption φ is taken
 1092 to be independent of time, and

$$\frac{\partial \varphi}{\partial t} = 0. \quad (3-15)$$

Then Eqn. 3-13 becomes the steady-state neutron transport equation,

$$\hat{\Omega} \cdot \nabla \varphi(\mathbf{r}, \hat{\Omega}, E) + \Sigma_t(\mathbf{r}, E) \varphi(\mathbf{r}, \hat{\Omega}, E) = \int_{4\pi} d\hat{\Omega}' \int_0^\infty dE' \Sigma_s(E' \rightarrow E, \hat{\Omega}' \rightarrow \hat{\Omega}) \varphi'(\mathbf{r}, \hat{\Omega}', E') + s(\mathbf{r}, E, \hat{\Omega}). \quad (3-16)$$

1093 Even after eliminating the partial derivative in time, Eqn. 3-13 is still not tractable
 1094 due to the three spatial derivatives and three integrals. Therefore, further reduction is
 1095 necessary.

1096 **3.2.2 Reduction to 1-D Planar**

Reducing the problem from three spatial dimensions to one spatial dimension eliminates two of the three spatial derivatives and one of the two direction derivatives. As an aside, the components of the direction vector $\hat{\Omega}$ are ϕ and θ components. ϕ is the azimuthal angle and θ is the polar angle. It is common to define the variable μ in terms of θ as

$$\mu \equiv \cos \theta,$$

where μ is defined over the range $[-1, 1]$ and ϕ is defined over the range $[0, 2\pi]$. Integrating Eqn. 3-16 over y , z , and ϕ reduces the dimensionality of the problem as

$$\int_{-\infty}^{\infty} dy \int_{-\infty}^{\infty} dz \int_0^{2\pi} d\phi \hat{\Omega} \cdot \nabla \varphi(\mathbf{r}, \hat{\Omega}, E) + \Sigma_t(\mathbf{r}, E) \varphi(\mathbf{r}, \hat{\Omega}, E) - \int_{4\pi} d\hat{\Omega}' \int_0^{\infty} dE' \Sigma_s(E' \rightarrow E, \hat{\Omega}' \rightarrow \hat{\Omega}) \varphi'(\mathbf{r}, \hat{\Omega}', E') + s(\mathbf{r}, E, \hat{\Omega}).$$

Solving the integrals yields:

$$\begin{aligned} \mu \frac{\partial}{\partial x} \varphi(x, E, \mu) + \Sigma_t(x, E) \varphi(x, E, \mu) = \\ 2\pi \int_0^{\infty} \int_{-1}^1 \Sigma_s(x, E', \mu' \rightarrow E, \mu) \varphi(x, E', \mu') d\mu' dE' + S(x, E, \mu). \end{aligned} \quad (3-17)$$

1097 Eqn. 3-17 is the steady-state 1-D planar form of the NTE. While this equation
 1098 appears much simpler to solve, the derivative on the left-hand side and two integrals
 1099 on the right-hand side indicate the equation is still an integro-differential equation and
 1100 further simplification is required to arrive at a tractable form. There are two common
 1101 reductions to Eqn. 3-17, 1) the multigroup discrete ordinates approximation and 2) the
 1102 diffusion approximation. The following sections apply each of these approximations to

₁₁₀₃ the NTE in order to arrive at two tractable forms of the NTE which will be used in the
₁₁₀₄ remainder of this work.

₁₁₀₅ 3.3 Multigroup Discrete Ordinates Approximation

₁₁₀₆ The multigroup discrete ordinates equations handle the two integrals on the
₁₁₀₇ right-hand side of Eqn. 3-17 by treating the integral over energy as integrals over energy
₁₁₀₈ ranges and approximating the integral over μ by evaluating the neutron flux at discrete
₁₁₀₉ angles within the full range of $[-1, 1]$. The final result is a set of coupled, first-order
₁₁₁₀ ordinary differential equations that are analytically tractable.

₁₁₁₁ 3.3.1 Treatment of Energy Dependence

₁₁₁₂ The first step in developing multigroup equations is to divide the neutron energy
₁₁₁₃ range of interest into a finite number of energy groups, E_g , where $g = 1, 2, \dots, G$. The order
₁₁₁₄ of the energy group number is such that energy decreases as the group number increases,
₁₁₁₅ (e.g., $E_g > E_{g+1}$) [36]. Energy groups are typically chosen such that the cross section
₁₁₁₆ shows little variation within a group. This is done in order for the group averaged cross
₁₁₁₇ section to best represent the energy-dependent cross section values of that group.

The 1-D planar time-independent neutron transport equation, Eqn. 3-17, is reproduced below for the readers convenience.

$$\mu \frac{\partial}{\partial x} \varphi(x, E, \mu) + \Sigma_t(x, E) \varphi(x, E, \mu) = 2\pi \int_0^\infty \int_{-1}^1 \Sigma_s(x; E', \mu' \rightarrow E, \mu) \varphi(x, E', \mu') d\mu' dE' + S(x, E, \mu). \quad (3-17)$$

Integrating Eqn. 3-17 over g yields

$$\underbrace{\int_g \mu \frac{\partial}{\partial x} \varphi(x, E, \mu) dE}_{(1)} + \underbrace{\int_g \Sigma_t(x, E) \varphi(x, E, \mu) dE}_{(2)} = \underbrace{\int_g 2\pi \int_0^\infty \int_{-1}^1 \Sigma_s(x; E', \mu' \rightarrow E, \mu) \varphi(x, E', \mu') d\mu' dE' dE}_{(3)} + \underbrace{\int_g S(x, E, \mu) dE}_{(4)} \quad (3-18)$$

where each term will be discussed individually. Before continuing, it is important to define the the group flux and group cross sections as:

$$\varphi_g(x, \mu) \equiv \int_{E_g}^{E_{g-1}} \varphi(x, E, \mu) dE = \int_g \varphi(x, E, \mu) dE, \quad (3-19)$$

$$\Sigma_{t,g}(x, \mu) \equiv \frac{\int_g \Sigma_t(x, E, \mu) \varphi(x, E, \mu) dE}{\varphi_g(x, E, \mu)}, \quad (3-20)$$

$$\Sigma_{s,g' \rightarrow g}(x, \mu) \equiv \frac{\int_{g'} \varphi(x, E', \mu) \int_g \int_{-1}^1 \Sigma_s(x; E', \mu' \rightarrow E, \mu) d\mu' dE dE'}{\varphi_{g'}(x, E', \mu)}. \quad (3-21)$$

₁₁₁₈ $\varphi_g(x, \mu)$ is the group averaged flux, $\Sigma_{t,g}(x, \mu)$ is the group averaged cross section, and

₁₁₁₉ $\Sigma_{s,g' \rightarrow g}(x, \mu)$ is the group to group, or transfer, cross section.

₁₁₂₀ Definitions 3-19 - 3-21 are used to rewrite Eqn. 3-18 term by term. The first term of
₁₁₂₁ Eqn. 3-18 is rewritten in terms of the group flux, 3-19 as

$$\int_g \mu \frac{\partial}{\partial x} \varphi(x, E, \mu) dE = \mu \frac{\partial}{\partial x} \varphi_g(x, \mu). \quad (3-22)$$

Rewriting the second term in Eqn. 3-18 using the total group cross section, Eqn. 3-20, yields

$$\int_g \Sigma_t(x, E, \mu) \varphi(x, E, \mu) dE = \Sigma_{t,g}(x, \mu) \varphi_g(x, \mu). \quad (3-23)$$

The third term in Eqn. 3-18 requires a bit more work. If the integral of dE' is taken over each individual energy group rather than over 0 to ∞ , then

$$\int_0^\infty dE' = \sum_{g'=1}^G \int_{E_{g'}}^{E_{g'-1}} dE' = \sum_{g'=1}^G \int_{g'} dE',$$

and the third term can be expressed using group constants, Eqn. 3-24.

$$\int_{g'} \varphi(x, E', \mu) \int_g \Sigma(x; E', \mu' \rightarrow E, \mu) dE dE' = \sum_{g'=1}^G \Sigma_{g' \rightarrow g}(x, \mu) \varphi_{g'}(x, \mu) \quad (3-24)$$

₁₁₂₂ Finally, the fourth term is the group source term, Eqn. 3-25. The group source term
₁₁₂₃ describes an arbitrary internal source of neutrons with energy in group g .

$$\int_g S(x, E, \mu) dE \equiv S_g(x, \mu). \quad (3-25)$$

₁₁₂₄ Using the redefined terms, Eqns. 3-22 - 3-25, Eqn. 3-18 becomes a set of equations
₁₁₂₅ characterizing the flux in each energy group:

$$\mu \frac{\partial \varphi_g}{\partial x} + \Sigma_{t,g} \varphi_g = 2\pi \sum_{g'=1}^G \int_{-1}^1 \Sigma_{s,g' \rightarrow g} \varphi_{g'} + S_g, \quad g = 1, 2, \dots, G. \quad (3-26)$$

₁₁₂₆ 3.3.2 Treatment of Directional Dependence

Equation 3-26 is a set of monoenergetic neutron transport equations where each equation defines the flux for the energy group g . Therefore, if a method for handling the directional dependence can be found for a single equation in the set of equations, the same method can be extended to all equations in Eqn. 3-26. The discrete ordinates method can be used to handle the integral over μ . By first assuming isotropic scattering, the in-scattering term reduces to

$$2\pi \sum_{g'=1}^G \int_{-1}^1 \Sigma_{s,g' \rightarrow g} \varphi_{g'} d\mu' = \frac{1}{2} \sum_{g'=1}^G \Sigma_{s,g' \rightarrow g} \int_{-1}^1 \varphi_{g'} d\mu',$$

₁₁₂₇ and Eqn. 3-26 reduces to

$$\mu \frac{\partial \varphi_g}{\partial x} + \Sigma_{t,g} \varphi_g = \frac{1}{2} \sum_{g'=1}^G \Sigma_{s,g' \rightarrow g} \int_{-1}^1 \varphi_{g'} + S_g, \quad g = 1, 2, \dots, G. \quad (3-27)$$

₁₁₂₈ Discrete ordinates treats directional dependence by evaluating the integral over μ at
₁₁₂₉ a unique set of directions, $\{\mu_i\}$. Evaluating the integral in Eqn. 3-27 at each value of μ_i
₁₁₃₀ leads to a weighted sum of neutron fluxes, Eqn. 3-28.

$$\int_{-1}^1 \varphi_{g'} = \sum_{j=1}^N \omega_j \phi_{g'}(x, \mu_j) \quad (3-28)$$

₁₁₃₁ Evaluating Eqn. 3-27 along the set of direction vectors $\{\mu_i\}$, using Eqn. 3-28, results in

₁₁₃₂ the multigroup discrete ordinates equations:

$$\mu_i \frac{d\phi_i^g}{dx} + \Sigma_t^g \phi_i^g = \frac{1}{2} \sum_{j=1}^N \omega_j \sum_{g'=1}^G \Sigma_{s,g' \rightarrow g} \phi_j^{g'} + S_i^g, \quad g = 1, 2, \dots, G; i = 1, 2, \dots, N. \quad (3-29)$$

For the purpose of this work, a set of equations are derived from Eqn. 3-29 using two energy groups ($g = 1, 2$) and two directions ($i = 1, 2$). Iterating over both indices one at a time leads to the following set of equations:

$$g = 1, i = 1$$

$$\mu_1 \frac{d\phi_1^1}{dx} + \Sigma_t^1 \phi_1^1 = \frac{1}{2} \left(\Sigma_s^{1 \rightarrow 1} \omega_1 \phi_1^1 + \Sigma_s^{1 \rightarrow 1} \omega_2 \phi_2^1 + \Sigma_s^{2 \rightarrow 1} \omega_1 \phi_1^2 + \Sigma_s^{2 \rightarrow 1} \omega_2 \phi_2^1 \right) + S_1^1; \quad (3-30)$$

$$g = 1, i = 2$$

$$\mu_2 \frac{d\phi_2^1}{dx} + \Sigma_t^1 \phi_2^1 = \frac{1}{2} \left(\Sigma_s^{1 \rightarrow 1} \omega_1 \phi_1^1 + \Sigma_s^{1 \rightarrow 1} \omega_2 \phi_2^1 + \Sigma_s^{2 \rightarrow 1} \omega_1 \phi_1^2 + \Sigma_s^{2 \rightarrow 1} \omega_2 \phi_2^1 \right) + S_2^1; \quad (3-31)$$

$$g = 2, i = 1$$

$$\mu_1 \frac{d\phi_1^2}{dx} + \Sigma_t^2 \phi_1^2 = \frac{1}{2} \left(\Sigma_s^{1 \rightarrow 2} \omega_1 \phi_1^1 + \Sigma_s^{1 \rightarrow 2} \omega_2 \phi_2^1 + \Sigma_s^{2 \rightarrow 2} \omega_1 \phi_1^2 + \Sigma_s^{2 \rightarrow 2} \omega_2 \phi_2^1 \right) + S_1^2; \quad (3-32)$$

$$g = 2, i = 2$$

$$\mu_2 \frac{d\phi_2^2}{dx} + \Sigma_t^2 \phi_2^2 = \frac{1}{2} \left(\Sigma_s^{1 \rightarrow 2} \omega_1 \phi_1^1 + \Sigma_s^{1 \rightarrow 2} \omega_2 \phi_2^1 + \Sigma_s^{2 \rightarrow 2} \omega_1 \phi_1^2 + \Sigma_s^{2 \rightarrow 2} \omega_2 \phi_2^1 \right) + S_2^2. \quad (3-33)$$

In a material where scattering from lower energy groups to higher energy groups does not occur and there is no internal neutron source, these equations reduce to:

$$g = 1, i = 1$$

$$\mu_1 \frac{d\phi_1^1}{dx} + \Sigma_t^1 \phi_1^1 = \frac{1}{2} \left(\Sigma_s^{1 \rightarrow 1} \omega_1 \phi_1^1 + \Sigma_s^{1 \rightarrow 1} \omega_2 \phi_2^1 \right); \quad (3-34)$$

$$g = 1, i = 2$$

$$\mu_2 \frac{d\phi_2^1}{dx} + \Sigma_t^1 \phi_2^1 = \frac{1}{2} \left(\Sigma_s^{1 \rightarrow 1} \omega_1 \phi_1^1 + \Sigma_s^{1 \rightarrow 1} \omega_2 \phi_2^1 \right); \quad (3-35)$$

$$g = 2, i = 1$$

$$\mu_1 \frac{d\phi_1^2}{dx} + \Sigma_t^2 \phi_1^2 = \frac{1}{2} \left(\Sigma_s^{1 \rightarrow 2} \omega_1 \phi_1^1 + \Sigma_s^{1 \rightarrow 2} \omega_2 \phi_2^1 + \Sigma_s^{2 \rightarrow 2} \omega_1 \phi_1^2 + \Sigma_s^{2 \rightarrow 2} \omega_2 \phi_2^2 \right); \quad (3-36)$$

$$g = 2, i = 2$$

$$\mu_2 \frac{d\phi_2^2}{dx} + \Sigma_t^2 \phi_2^2 = \frac{1}{2} \left(\Sigma_s^{1 \rightarrow 2} \omega_1 \phi_1^1 + \Sigma_s^{1 \rightarrow 2} \omega_2 \phi_2^1 + \Sigma_s^{2 \rightarrow 2} \omega_1 \phi_1^2 + \Sigma_s^{2 \rightarrow 2} \omega_2 \phi_2^2 \right). \quad (3-37)$$

1133

3.4 Reduction to Diffusion Approximation

The diffusion approximation is an alternative reduction of the NTE. There are several methods for deriving the diffusion approximation, however, this derivation uses Legendre polynomial expansions to account for angular dependence in the equation. The neutron transport equation can be simplified through the use of spherical harmonics, which in 1-D, reduce to Legendre polynomials to expand the angular flux and source terms while assuming an isotropic angular differential cross section. The 1-D planar, monoenergetic, NTE with isotropic scattering is

$$\begin{aligned} \mu \frac{\partial}{\partial x} \varphi(x, \mu) + \Sigma_t(x) \varphi(x, \mu) = \\ \frac{1}{2} \int_{-1}^1 \Sigma_s(x, \mu' \rightarrow \mu) \varphi(x, \mu') d\mu' + S(x, \mu) \end{aligned} \quad (3-38)$$

1134 Expanding the angular flux with Legendre polynomials separates the directional and
 1135 spatial components of the angular flux. Legendre polynomials exhibit an orthogonality
 1136 property, Eqn. 3-39, and a "3-term recursion" relationship, Eqn. 3-40, which are used in

¹¹³⁷ deriving the diffusion approximation.

$$\int_{-1}^1 d\mu P_l(\mu) P_m(\mu) = \frac{2}{2l+1} \delta_{lm} \quad (3-39)$$

¹¹³⁸

$$(2l+1)\mu P_l(\mu) = (l+1)P_{l+1}(\mu) + (l)P_{l-1}(\mu) \quad (3-40)$$

Expanding the angular flux in Eqn. 3-38 yields:

$$\begin{aligned} \mu \frac{\partial}{\partial x} \left[\sum_l^{\infty} \frac{2l+1}{2} \phi_l(x) P_l(\mu) \right] + \Sigma_t \sum_l^{\infty} \frac{2l+1}{2} \phi_l(x) P_l(\mu) = \\ \frac{1}{2} \int_{-1}^1 d\mu' \Sigma_s(x, \mu_0) \sum_l^{\infty} \frac{2l+1}{2} \phi_l(x) P_l(\mu') + S(x, \mu). \end{aligned} \quad (3-41)$$

Requiring the projections of Eqn. 3-41 against Legendre polynomials of degree m (e.g., P_m) to be equal to 0 leads to

$$\begin{aligned} \int_{-1}^1 d\mu \mu \frac{\partial}{\partial x} \left[\sum_{l=0}^1 \frac{2l+1}{2} \phi_l(x) P_l(\mu) P_m(\mu) \right] + \int_{-1}^1 d\mu \Sigma_t \sum_{l=0}^1 \frac{2l+1}{2} \phi_l(x) P_l(\mu) P_m(\mu) = \\ \frac{1}{2} \int_{-1}^1 d\mu P_m(\mu) \int_{-1}^1 d\mu' \Sigma_s(x, \mu_0) \sum_{l=0}^1 \frac{2l+1}{2} \phi_l(x) P_l(\mu') + \int_{-1}^1 d\mu S(x, \mu) P_m(\mu). \end{aligned} \quad (3-42)$$

¹¹³⁹ The summation is truncated at $l = 1$ since the first two terms are all that is necessary for

¹¹⁴⁰ finding the diffusion approximation.

Using the recurrence relationship, Eqn. 3-40, in the first term of Eqn. 3-42 yields

$$\sum_{l=0}^1 \frac{\partial \phi_l(x)}{\partial x} \left[\int_{-1}^1 d\mu \frac{l+1}{2} P_{l+1}(\mu) P_m(\mu) + \int_{-1}^1 d\mu \frac{l}{2} P_{l-1}(\mu) P_m(\mu) \right].$$

Applying the orthogonality gives,

$$\frac{(m-1)+1}{2} \frac{2}{2m+1} \frac{\partial \phi_{m-1}(x)}{\partial x} + \frac{m+1}{2} \frac{2}{2m+1} \frac{\partial \phi_{m+1}(x)}{\partial x},$$

or,

$$\frac{m}{2m+1} \frac{\partial \phi_{m-1}(x)}{\partial x} + \frac{m+1}{2m+1} \frac{\partial \phi_{m+1}(x)}{\partial x}.$$

The second term in Eqn. 3-42 is also solved using the orthogonality property as,

$$\Sigma_t \sum_{l=0}^1 \frac{2l+1}{2} \phi_l(x) \int_{-1}^1 d\mu P_l(\mu) P_m(\mu)$$

such that,

$$\Sigma_t \sum_{l=0}^1 \frac{2l+1}{2} \phi_m(x) \frac{2}{2m+1},$$

or,

$$\Sigma_t \phi_m(x).$$

Solving the third term of Eqn. 3-42 involves calculating the values for $P_{l/m}(\mu)$ for $l, m = 0, 1$, which are $P_0(\mu) = 1$ and $P_1(\mu) = \mu$. Note each integral evaluates to 0 when either l or m is odd. Alternatively, the scattering term evaluates to $2\phi_m$ when l and m are 0.

$$\frac{1}{2} \Sigma_s(x, \mu_0) \sum_{l=0}^1 \frac{2l+1}{2} \int_{-1}^1 d\mu' \phi_l(x) P_l(\mu') \int_{-1}^1 d\mu P_m(\mu) = \begin{cases} 2\phi_0; & l \text{ and } m = 0 \\ 0; & \text{else.} \end{cases}$$

And the final term in Eqn. 3-42 is simply redefined as:

$$S_m \equiv \int_{-1}^1 d\mu S(x, \hat{\Omega}) P_m(\mu).$$

₁₁₄₁ For an isotropic source, $S_m = 0$ for $m > 0$.

₁₁₄₂ Combining the terms leads to the final set of P_1 equations, Eqns. 3-43 and 3-44.

$$\frac{\partial \phi_1}{\partial x} + \Sigma_t \phi_0 = \Sigma_s \phi_0 + S_0 \quad (3-43)$$

₁₁₄₃

$$\frac{1}{3} \frac{\partial \phi_0}{\partial x} + \frac{2}{5} \frac{\partial \phi_2}{\partial x} + \Sigma_t \phi_1 = S_1. \quad (3-44)$$

₁₁₄₄ If this set of equations were solved for ϕ_0 , the result would be the diffusion approximation.

₁₁₄₅ Unfortunately, there are three unknowns (ϕ_0 , ϕ_1 , and ϕ_2) and two equations. In fact, this

₁₁₄₆ set of equations will always have more unknown variables than equations. Therefore, a

₁₁₄₇ closure condition is needed to truncate the set of equations by setting $\phi_n = 0$ for $n \geq 2$.

₁₁₄₈ Eqn. 3-44 then becomes

$$\phi_1 = \frac{-1}{3\Sigma_t} \frac{\partial\phi_0}{\partial x} \quad (3-45)$$

₁₁₄₉ which is Fick's Law.

Substituting Fick's Law in Eqn. 3-43 for ϕ_1

$$\frac{\partial}{\partial x} \left[\frac{-1}{3\Sigma_t} \frac{\partial\phi_0}{\partial x} \right] + \Sigma_t \phi_0 = \Sigma_s \phi_0 + S_0,$$

₁₁₅₀ which simplifies to the 1-D, mono-energetic, steady state diffusion approximation:

$$-D \frac{\partial^2 \phi_0}{\partial x^2} + \Sigma_a \phi_0 = S_0, \quad (3-46)$$

₁₁₅₁ where D , the diffusion coefficient is defined as

$$D \equiv \frac{-1}{3\Sigma_t}, \quad (3-47)$$

₁₁₅₂ when D is independent of x . The second derivative, $\frac{\partial^2}{\partial x^2}$, results from expressing the

₁₁₅₃ Laplacian operator in a planar coordinates systems where the coordinate-independent

₁₁₅₄ diffusion approximation is

$$-D \nabla^2 \phi_0 + \Sigma_a \phi_0 = S_0, \quad (3-48)$$

₁₁₅₅ from Duderstadt & Hamilton [37]. Given the cylindrical geometry of the cask, the

₁₁₅₆ diffusion equation is expected to be applied in a cylindrical coordinate system. Equation

₁₁₅₇ 3-49 is the 1-D cylindrical, steady-state monoenergetic diffusion equation where the

₁₁₅₈ Laplacian has been expressed in cylindrical coordinates.

$$-D \frac{1}{r} \frac{d}{dr} \left(r \frac{d\phi_0}{dr} \right) + \Sigma_a \phi_0 = S_0 \quad (3-49)$$

₁₁₅₉ 3.5 Cylindrical to Polar Coordinate Shift

₁₁₆₀ The cylindrical shape of the spent fuel cask immediately lends to a cylindrical

₁₁₆₁ geometry for the mathematical models. However, given the large radius of the cask, it is

₁₁₆₂ expected that there exists a point along the radius of the cask where polar geometry can

₁₁₆₃ be relaxed to a planar geometry with negligible effect to the neutron flux. This point can
₁₁₆₄ be found through a dimensional analysis by developing non-dimensional forms for both the
₁₁₆₅ radial and planar diffusion equations.

₁₁₆₆ Non-dimensional analysis is a process where an equation is rewritten in a manner such
₁₁₆₇ that there are no units in the problem (i.e., all parameters and variables in an expression
₁₁₆₈ are redefined using ratios rather than dimensional quantities). A comparison can be
₁₁₆₉ made between the non-dimensional forms of the 1-D polar diffusion approximation and
₁₁₇₀ 1-D planar diffusion approximation to determine the location where planar geometry is
₁₁₇₁ appropriate.

₁₁₇₂ Starting with the geometry-independent diffusion equation,

$$-D\nabla^2\phi + \Sigma_a\phi = S. \quad (3-46)$$

₁₁₇₃ where the second derivative has been written using the gradient, D is the diffusion
₁₁₇₄ coefficient, ϕ is the scalar flux, Σ_a is macroscopic absorption cross section, and S is the
₁₁₇₅ source term. The monoenergetic, steady-state, 1-D planar diffusion approximation:

$$-D\frac{d^2\phi}{dx^2} + \Sigma_a\phi = S. \quad (3-46)$$

₁₁₇₆ Dividing the equation by $-D$ and defining $L^{-2} \equiv \frac{\Sigma_a}{D}$,

$$\frac{d^2\phi}{dx^2} - \frac{1}{L^2}\phi + \frac{S}{D} = 0. \quad (3-50)$$

₁₁₇₇ Non-dimensionalizing x ,

$$\tilde{x} = \frac{x}{L}, \quad (3-51)$$

₁₁₇₈ where \tilde{x} is the non-dimensionalized form of x . The first derivative becomes

$$dx = L d\tilde{x} \quad (3-52)$$

₁₁₇₉ in non-dimensional form.

¹¹⁸⁰ The second order differential of x , dx^2 , becomes

$$dx^2 = L^2 d\tilde{x}. \quad (3-53)$$

Eqn. 3-46 then becomes

$$\frac{1}{L^2} \frac{d^2\phi}{dx^2} - \frac{1}{L^2} \phi + \frac{S}{D} = 0,$$

¹¹⁸¹ or,

$$\frac{d^2\phi}{d\tilde{x}^2} - \phi + \frac{L^2 S}{D} = 0. \quad (3-54)$$

¹¹⁸² Note: $\frac{L^2 S}{D}$ has units of $Length^{-2} Time^{-1}$, which are the same units as ϕ . So,

$$\tilde{\phi} = \frac{\phi}{L^2 S / D}, \quad (3-55)$$

¹¹⁸³ or,

$$\phi = \tilde{\phi} \frac{L^2 S}{D}, \quad (3-56)$$

¹¹⁸⁴ where $\tilde{\phi}$ is the non-dimensionalized form of ϕ . The second differential of ϕ becomes

$$d^2\phi = \frac{L^2 S}{D} d^2\tilde{\phi}. \quad (3-57)$$

¹¹⁸⁵ Using $\tilde{\phi}$, Eqn. 3-54 is written as

$$\frac{L^2 S}{D} \frac{d^2\tilde{\phi}}{d\tilde{x}^2} - \frac{L^2 S}{D} \tilde{\phi} + \frac{L^2 S}{D} = 0, \quad (3-58)$$

¹¹⁸⁶ or,

$$\frac{d^2\tilde{\phi}}{d\tilde{x}^2} - \tilde{\phi} + 1 = 0. \quad (3-59)$$

¹¹⁸⁷ The 1-D planar diffusion approximation is now expressed in a non-dimensional form.

¹¹⁸⁸ Expressing the gradient in Eqn. 3-46 in 1-D polar coordinates yields

$$\frac{1}{r} \frac{d}{dr} \left(r \frac{d\phi}{dr} \right) - \frac{1}{L^2} \phi + \frac{S}{D} = 0, \quad (3-60)$$

¹¹⁸⁹ or,

$$\frac{d^2\phi}{dr^2} + \frac{1}{r} \frac{d\phi}{dr} - \frac{1}{L^2} \phi + \frac{S}{D} = 0. \quad (3-61)$$

1190 Let

$$\tilde{r} = \frac{r}{L}, \quad (3-62)$$

1191 and,

$$\tilde{\phi} = \frac{\phi D}{L^2 S} \quad (3-63)$$

1192 Using the non-dimensionalized variables defined in Eqns. 3-62 and 3-63, Eqn. 3-61 can
1193 be rewritten as

$$\frac{d^2 \tilde{\phi}}{d\tilde{r}^2} + \frac{1}{\tilde{r}} \frac{d\tilde{\phi}}{d\tilde{r}} - \tilde{\phi} + 1 = 0. \quad (3-64)$$

1194 Then, the curvilinear form of the diffusion equation is

$$\frac{d^2 \tilde{\phi}}{d\tilde{r}^2} + \frac{k}{\tilde{r}} \frac{d\tilde{\phi}}{d\tilde{r}} - \tilde{\phi} + 1 = 0, \quad (3-65)$$

1195 where $k = 0$ for planar geometries and $k = 1$ for cylindrical geometries. Further, plotting
1196 the variable $\frac{k}{\tilde{r}}$ for $k = 1$ will show the location where accounting for polar geometries
1197 becomes negligible. Figure 3-1 shows the result from the previous dimensional analysis
1198 using material properties of the fuel materials. Near 1cm into the fuel material, results
1199 calculated using a cylindrical and planar geometries agree within 10% (denoted by the
1200 vertical black line in Fig. 3-1). After 1cm materials can be approximated using planar
1201 equations, however, the flux in the fuel region will need to be approximated using a polar
1202 diffusion equation.

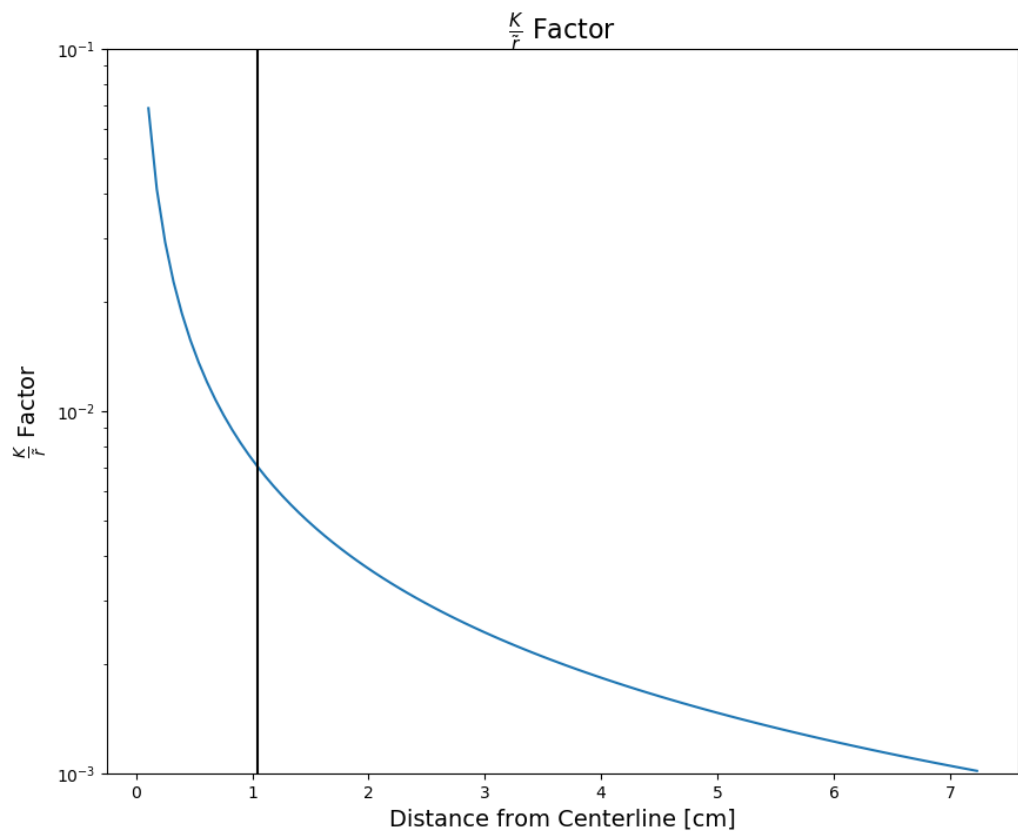


Figure 3-1. As the factor $\frac{k}{\bar{r}}$ decreases, the planar solutions better approximate polar solutions in the homogenous fuel material. The location of the black vertical line shows the point where the factor $\frac{k}{\bar{r}}$ is 10% of its initial value.

1203
1204

CHAPTER 4 ANALYSIS OF SUB-PROBLEMS

1205 This chapter analyzing each sub-problem in depth according to the results assessment
1206 methodology using the mathematical models identified in Sec. 2 and derived in Sec.
1207 3. Through the explanation of the causes of each feature, confidence is gained in the
1208 correctness of the detailed MCNP simulation.

1209

4.1 Identification of Mathematical Models in Each Region

1210 Chapter 2 identified the analytic model choice for each material region. However,
1211 differential equations only yield unique solutions when coupled with boundary conditions.
1212 Therefore, a discussion identifying appropriate boundary conditions in each material is
1213 provided. The fuel region has a unique geometry-induced feature at the center of the
1214 cylindrical fuel region where the radius is 0. The geometry at the center of the cask
1215 suggests the central symmetry boundary condition which limits the solution to a finite
1216 value at the centerline of the cask, where $r = 0$, as

$$\lim_{r \rightarrow 0} \phi(r) < \infty. \quad (4-1)$$

1217 Further, at the exiting surface of the fuel region, an approximate non-reentrant boundary
1218 condition associated with Eqn. 3-49 is

$$\phi(\mathbf{r}_b + d) = 0, \quad (4-2)$$

1219 where \mathbf{r}_b is the vector of positions comprising the outer surface S of V , and d is an
1220 “extrapolation distance” [suggested via notation to be uniformly added to each element of
1221 \mathbf{r}_b in Eqn. 4-2] given by Eqn. 4-2] given by

$$d = 2.13D. \quad (4-3)$$

1222 Equation 4-2 is intended to qualitatively reproduce the neutron flux behavior at the outer
1223 surface of a non-reentrant convex body, as otherwise observed from more general neutron
1224 transport scenarios (see, for example, Lamarch and Baratta).

1225 The remaining materials share the same choice of analytic model, Eqn. 3-29.
1226 Therefore, a single boundary condition can be used in each model, specifically, choosing
1227 to have a continuous flux boundary condition for each partial flux is satisfactory between
1228 each material, Eqn. 4-4. In Eqn. 4-4, a and b represent the two materials on either side of
1229 the boundary surface, i is the direction and g is the energy group number. The multigroup
1230 discrete ordinates equation is a first-order set of coupled differential equations and a single
1231 boundary condition for each flux is adequate.

$$\phi_{a,i}^g = \phi_{b,i}^g \quad (4-4)$$

Finally, the analytic model changes at the boundary between the fuel region and the MPC. That is, the flux in the fuel is analytically predicted using the diffusion approximation where the flux in the remaining materials is predicted using the multigroup discrete ordinates equation. The flux in the fuel is given as a single flux, treated at a single energy group and with no angle dependence. However, the multigroup discrete ordinates equations treats the flux in two energy groups and two angles. In order to “stitch” the flux together at the interface between the fuel region and MPC, energy and angular distribution data is approximated at the interior surface of the MPC. Figure 2-8h shows the percentage of neutrons above 10keV as 73.854%. Therefore, 73.854% of the neutrons calculated with the diffusion equation are considered “fast” neutrons and this is called the fast energy group or group 1 flux. The remaining neutrons are placed in the “thermal” energy or group 2 flux. A similar approach is used to treat the angular dependence at the interface. From the analysis of the detailed cask, 57.283% of the neutrons are traveling forward, or outward from the fuel region. Therefore, these neutrons are considered the right moving flux and remaining neutrons are considered left moving. This rough analysis

of the flux at the interface provides a suitable boundary condition for the flux at the inner surface of the MPC, where Eqns. 4-5-4-8 show the boundary conditions for each partial neutron flux.

$$\phi_1^{MPC,1}(x = 84.34) = (0.73854)(0.57383)\phi_{fuel} \quad (4-5)$$

$$\phi_2^{MPC,1}(x = 84.34) = (0.73854)(0.42617)\phi_{fuel} \quad (4-6)$$

$$\phi_1^{MPC,2}(x = 84.34) = (0.26146)(0.57383)\phi_{fuel} \quad (4-7)$$

$$\phi_2^{MPC,2}(x = 84.34) = (0.26146)(0.42617)\phi_{fuel} \quad (4-8)$$

1232

4.2 Discussion of Sub-problems

1233 **4.2.1 Flat Region**

1234 Initially, the flatness of the first feature suggests that a reduction in fine structure
 1235 detail can be used to adequately represent a substantial portion the fuel region. Each
 1236 fuel pin is approximately 1cm in diameter, yet the neutron flux spatial distribution does
 1237 not show variations at the centimeter level. Fluctuations in the neutron flux spatial
 1238 distribution at the centimeter level would require any simplified models to also preserve
 1239 geometric structures at the centimeter level, but the absence of these fluctuations implies
 1240 that geometric reductions are possible. Therefore, an MCNP model is developed with a
 1241 homogenized fuel in the MPC similar to the analytic model.

1242 For the purpose of clarity, this fuel composition is called “fully homogenized” since
 1243 it incorporates all the materials inside the MPC. The fully homogenized fuel composition
 1244 is determined by calculating the mass fractions of each material in the MPC (the
 1245 stainless steel basket, the neutron absorbing pads, the helium backfill, and the fuel
 1246 rods). Finally, the density of the fully homogenized fuel is corrected to account for the
 1247 various densities of each material in the MPC ($10.44 \frac{g}{cm^3}$ for a single fuel rod vs. $2.31 \frac{g}{cm^3}$
 1248 for the fully homogenized fuel). The entire interior volume of the MPC is filled with the
 1249 fully homogenized fuel material. Figure 4-1 is a cross section view of the corresponding

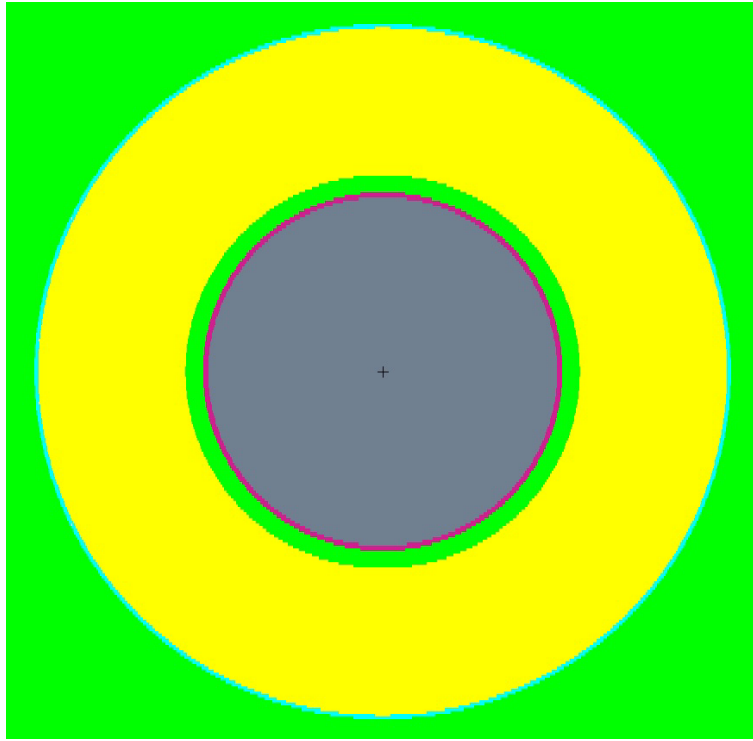


Figure 4-1. The homogeneous model. The gray circle is the fully homogenized fuel which fills the entire volume interior to the MPC.

1250 MCNP model using the fully homogenized fuel material. This model is referred to as the
 1251 “homogenous model”.

1252 Figure 4-2 shows the homogeneous model neutron flux spatial distribution through
 1253 the fuel region of the MPC, together with the complementary result from the detailed
 1254 model. The homogenous model over predicts the neutron flux spatial distribution by
 1255 20-25% through the fuel region. Even though the reduced model overpredicts the detailed
 1256 flux, the shape of the neutron flux spatial distribution predicted in both models shows a
 1257 steady decrease across the inner 65 cm. The relative flatness of the two fluxes is evidence
 1258 that geometric attenuation is less important than the material properties within the MPC.
 1259 To further corroborate this notion, Fig. 4-2 also includes results from an analytic model:
 1260 the dotted line appearing in this figure is a result from monoenergetic, 1D cylindrical
 1261 diffusion theory, Eqn. 3-46. In this analytic setting, the monoenergetic scalar neutron flux

1262 across a 1D cylindrical region with constant material properties is given by

$$\phi(r) = \frac{\alpha}{DB^2} \left(1 - \frac{I_0(Br)}{I_0(B\tilde{r})} \right); \quad B \equiv \sqrt{\frac{\Sigma_a - \bar{\nu}\Sigma_f}{D}}. \quad (4-9)$$

1263 where α is the intrinsic neutron source, B is the material buckling as indicated in terms
1264 of the macroscopic total absorption cross section Σ_a , macroscopic fission cross section Σ_f ,
1265 and mean number of neutrons per fission $\bar{\nu}$, and diffusion coefficient D , I_0 is the modified
1266 Bessel function of the first kind, and \tilde{r} is the extrapolated radius of the fuel region. The
1267 spatial curvature of the scalar flux appearing in Eq. 4-9 is controlled principally by the
1268 material buckling B ; as the value of B increases (resulting when absorption physics is
1269 dominant over scattering physics) the neutron flux spatial distribution calculated in Eq.
1270 4-9 produces a flat distribution in r - as in fuel region of both computational models. This
1271 result is discussed further in conjunction with the sensitivity discussion corresponding to
1272 the diffusion approximation. The flatness of the diffusion model is proof that the flatness
1273 seen in the MCNP models is due to material properties being dominant over geometry.
1274 While the diffusion model captures the essential physics giving rise to the flat flux region,
1275 it does not adequately capture the abrupt level off within the fuel region for $r > 65\text{cm}$.

1276 4.2.2 Abrupt Level-off Region

1277 In order to better capture the physics which describes the second feature, a second
1278 model is developed. The purpose of this model is to capture the physics associated
1279 with the neutron flux spatial distribution suddenly flattening before exiting the MPC.
1280 Intuitively, since geometric attenuation is minimal and the mfp for neutrons (70,000 cm
1281 at 1 MeV) is much greater than the thickness of the region between the fuel basket and
1282 MPC wall (10 cm), a free streaming (i.e., constant flux) approximation is likely to be
1283 valid there. To corroborate this notion, the homogeneous model is further modified to add
1284 an annulus of helium around a fuel region which is reduced in radius in a manner which
1285 preserves the volume of the original 32 fuel cells. This model is referred to as the “helium
1286 model”. Fig. 4-3 shows the difference between the homogenous and helium models. The

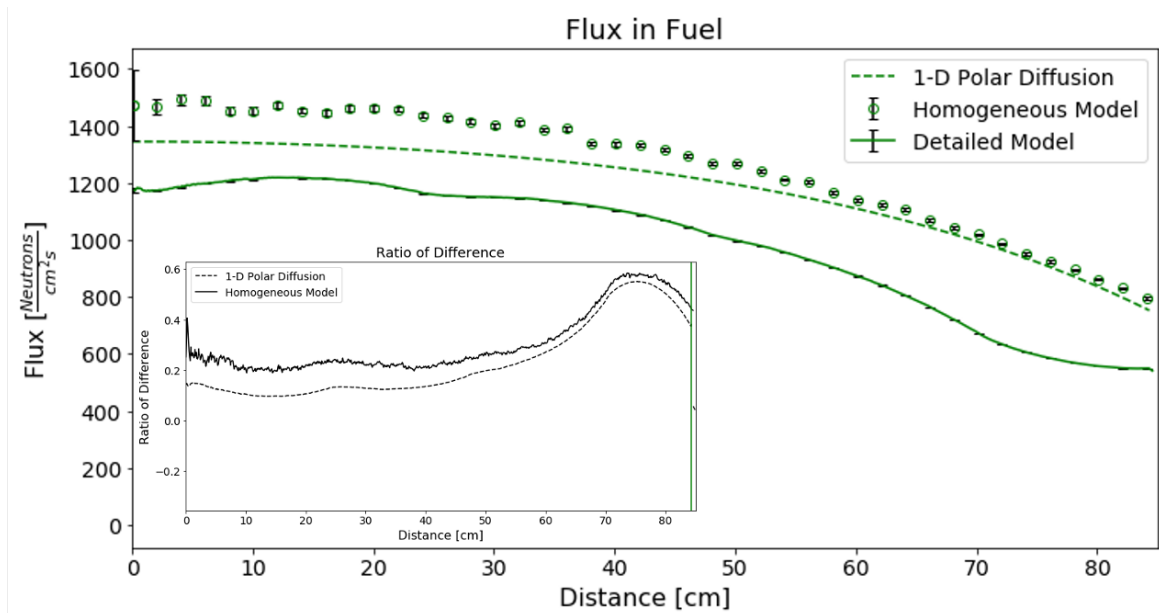


Figure 4-2. The results of the simulated neutron flux spatial distribution from the homogenous model (circles) is similarly flat to the neutron flux spatial distribution of the detailed model (solid line). The flux calculated using the diffusion approximation (dotted line) is also plotted against the two MCNP models. The diffusion approximation also shows the flatness of the neutron flux spatial distribution.

1287 composition of the fuel region is changed to account for the helium now present in the
1288 annulus. The new homogenized fuel composition, called the partially homogenized fuel
1289 composition, is made using the mass fractions of materials in the 32 fuel cells (the stainless
1290 steel fuel basket, the neutron absorbing pads, the helium interior to the fuel cells, the fuel
1291 rods) and the density of the material is adjusted to account for the reduced amount of
1292 helium ($2.95 \frac{g}{cm^3}$).

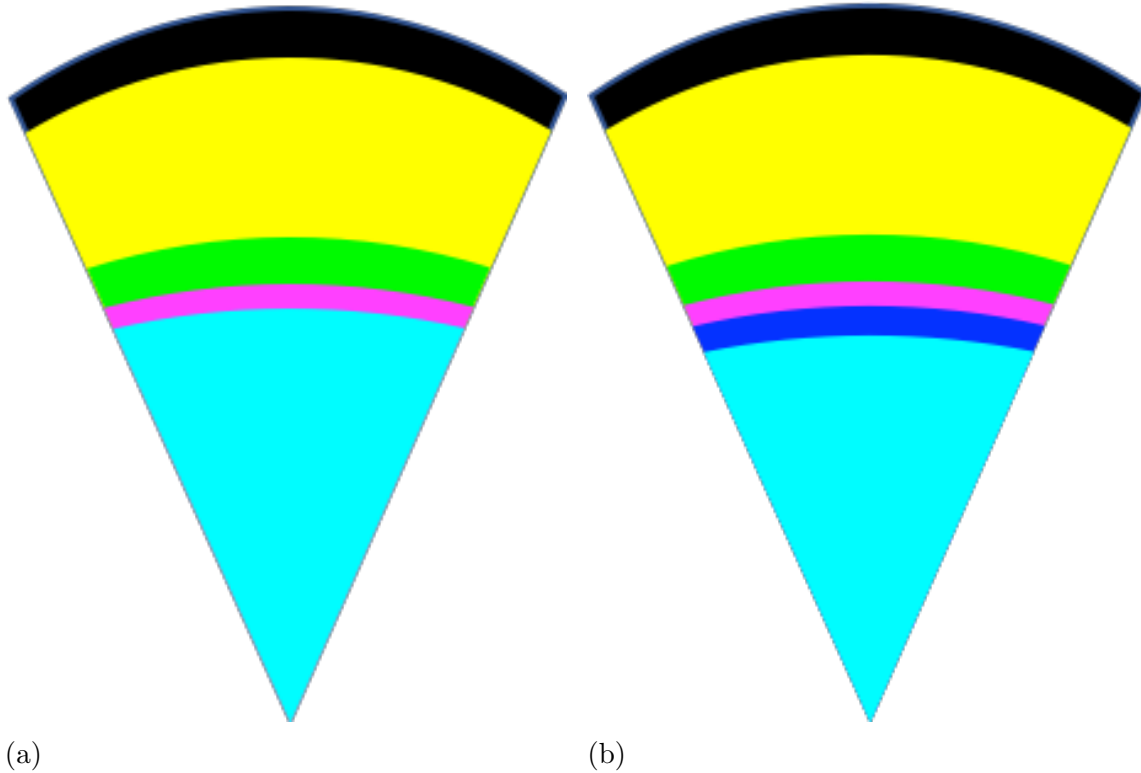


Figure 4-3. A) Section views of the homogeneous model, B) Helium model. The helium model includes an annulus of helium gas, ~ 10 cm thick, added around the homogenized fuel to allow streaming at the edge of the fuel region. Not to scale.

1293 Figure 4-4 shows the results of the simulated flux in the helium model as compared
1294 to the detailed model. The fuel region, comprised of partially homogenized fuel material,
1295 has a smaller radius and the analytic solution is held constant for $r > \tilde{r}$. The increased
1296 density of the fuel in the helium model increases the total neutron absorption and thus
1297 lowers the amplitude of the neutron flux spatial distribution. The flux flattens out over

1298 the last 20 cm, which is a result of adding the non-interacting helium annulus. The helium
1299 model better demonstrates that the flatness of the two MCNP models and the analytic
1300 model match, with the exception of the three depressions present in the detailed models.
1301 These results do show neutrons streaming through the helium region exterior to the fuel
1302 cells before exiting into the MPC even though the helium model and the analytic model
1303 do not capture the small depressions.

1304 4.2.3 Inter-bundle Depressions

1305 To this point, the simulation results assessment has shown that explanation of causes
1306 for the first two features does not necessitate simulation of geometric details at the
1307 individual fuel pin level. However, the physics associated with the three small depressions
1308 in the detailed model (seen in Fig. 2-23) has not been explained. Intuition suggests it
1309 seems necessary that some level of geometric detail needs to be added back into the
1310 reduced complexity simulations to identify the cause of the final two features.

1311 The scalar flux depressions depicted in Fig. 2-23 represent the third feature and
1312 are presumed to be caused by the neutron absorbing pads that are present between fuel
1313 bundles, located at $-71.62 < x < -71.41$ cm, $-47.61 < x < -47.40$ cm, $-23.61 <$
1314 $x < -23.40$ cm, $0.40 < x < 0.61$ cm, $24.40 < x < 24.61$ cm, $48.41 < x < 48.62$
1315 cm. These pads contain ^{10}B , which has a propensity of absorbing thermal neutrons. To
1316 corroborate this notion, reintegrating the stainless steel basket structure and neutron
1317 absorbing pads is expected to capture the depressions not found in the previous models.
1318 Again, comparing the mfp of neutrons in stainless steel 304, the neutron absorbing pads,
1319 and fuel rods in Fig. 4-5 shows the mfp is dominated by the absorbing component at a
1320 level of approximately 10cm (or less, depending on the energy of the incident neutrons).
1321 These mfp's are similar to the physical thickness of the stainless steel, neutron absorbing
1322 pads, and fuel in the MPC. Therefore, the neutrons will undergo an appreciable number of

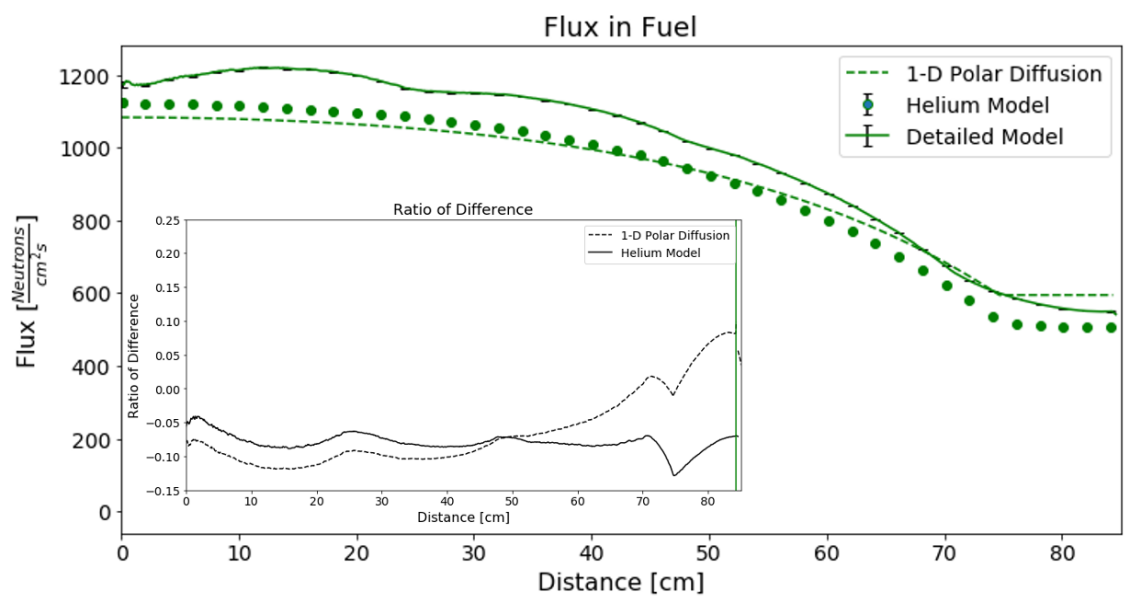


Figure 4-4. The neutron flux spatial distribution simulated by the helium model (circles) captures the neutron flux spatial distribution flattening out in the detailed model (solid line) over the 20 cm region before exiting the fuel region. The diffusion approximation (dotted line) also captures the flux flattening near 65 cm from the cask centerline after adding a helium annulus for neutron streaming.

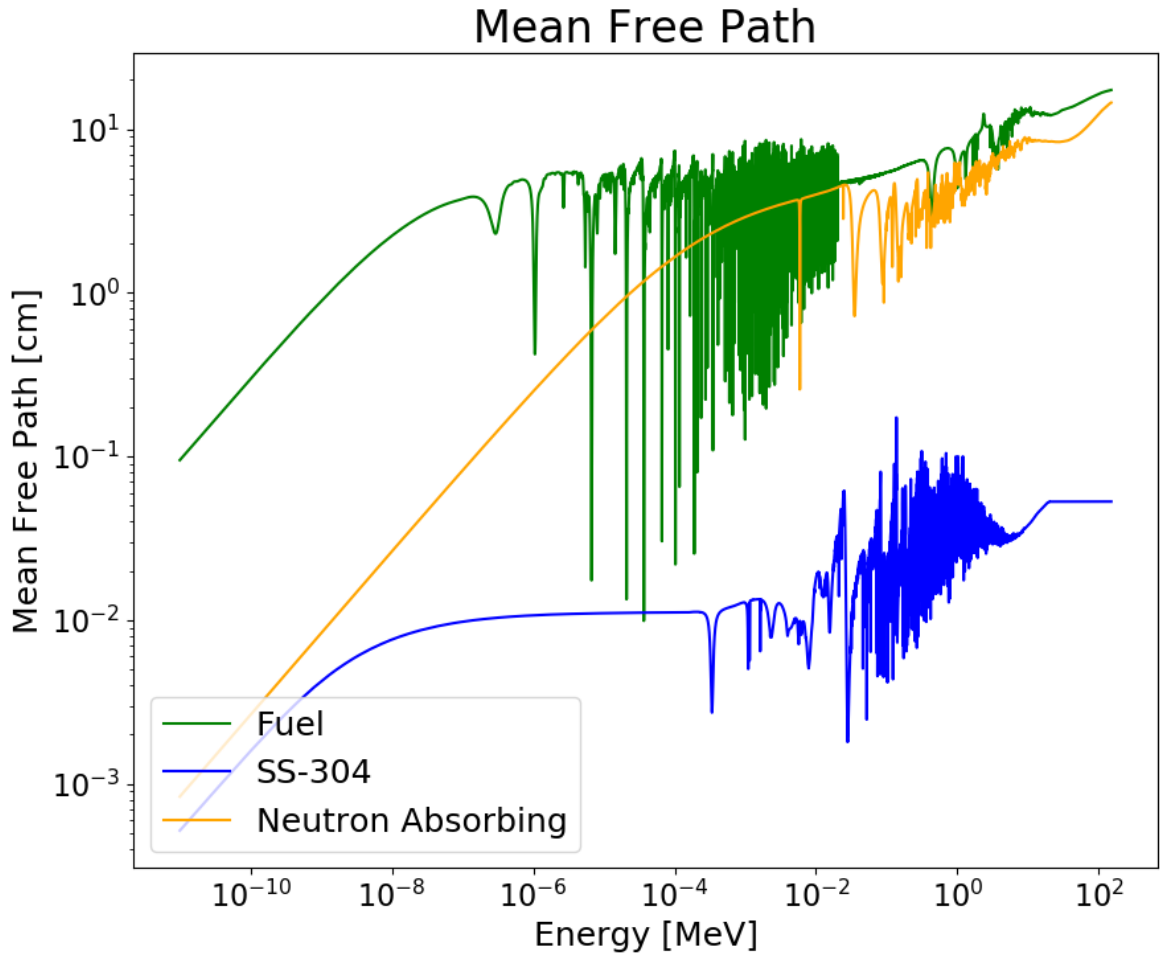


Figure 4-5. The mean free paths for stainless steel 304 (blue), neutron absorbing pad material (orange), and fuel pin material (green). These three mean free paths are similar to the physical thicknesses of each material implying that the steel and neutron absorbing pads need to be included in MCNP simulations as discrete materials instead of being incorporated into the homogenized fuel.

1323 interactions in the stainless steel and neutron absorbing materials. However, unlike in the
 1324 fuel, no neutrons are being generated in the steel and neutron absorbing materials, and so
 1325 the flux is expected to decrease therein.

1326 Another MCNP model is developed to describe the cause of the depressions, Fig. 4-6.
 1327 This multi-layered model is called the “1-D basket model” and represents a single row

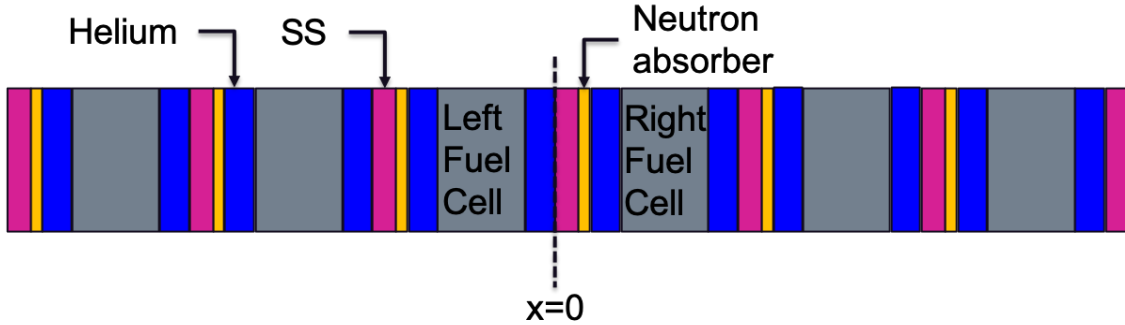


Figure 4-6. The 1-D basket model used to identify the cause of the small depressions. The model is repeating layers of stainless steel (pink), neutron absorbing pads (orange), helium (blue), and cell homogenized fuel (gray).

1328 of fuel cells from the detailed model with one difference: the volume attributed to fuel
 1329 materials. In this model, the interior volume of each fuel cell contains a cell homogenized
 1330 fuel composition with helium on both sides and neutron absorbing pad to the left. The cell
 1331 homogenized fuel composition is determined using the mass fraction of materials which
 1332 comprise the 264 fuel rods and helium between the fuel rods in each cell. The volume of
 1333 the cell homogenized fuel material is defined to be equal to the volume of a single fuel
 1334 bundle.

1335 The simulated neutron flux spatial distribution through the 1-D basket model is
 1336 shown in Fig. 4-7. The simplified basket model has six small depressions present in the
 1337 flux around ± 25 cm, ± 50 cm, ± 75 cm. These depressions correspond to a 1-2 % local
 1338 reduction in the flux, which is similar in location and magnitude to the depressions present
 1339 in the simulated neutron flux spatial distribution in the detailed model. The depressions in
 1340 the neutron flux spatial distribution occur within the stainless steel and neutron absorbing
 1341 pad materials. The flux increases in the fuel as neutrons are born from spontaneous fission
 1342 decays and (α, n) reactions. The combination of the absorption events in the neutron
 1343 absorbing pads and source events in the fuel cause the depressions observed in the neutron
 1344 flux spatial distribution.

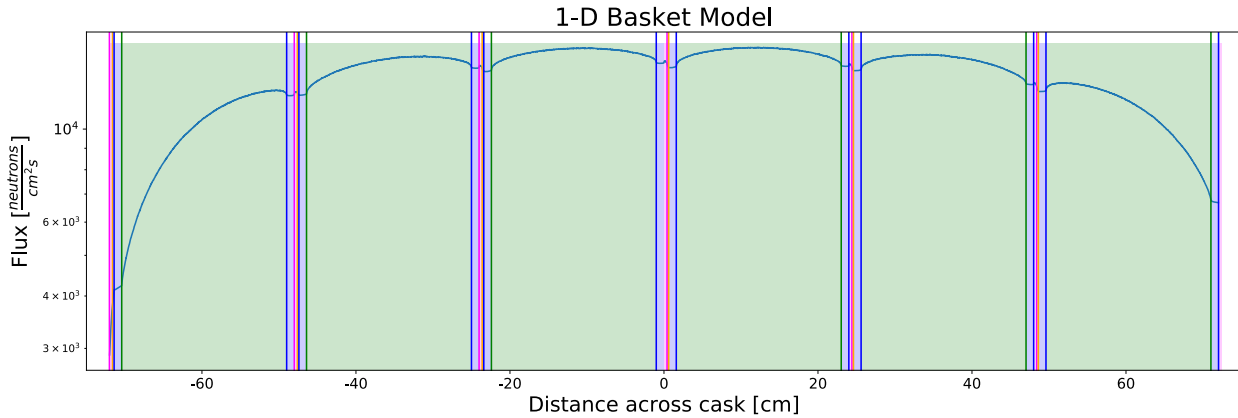


Figure 4-7. The neutron flux spatial distribution simulated from the 1-D basket model. The colors are representative of each material: stainless steel 304 (pink), neutron absorbing pad (orange), helium (blue), and cell homogenized fuel (green). There are depressions present in the flux which occur within the stainless steel and neutron absorbing pads.

1345 **4.2.4 Azimuthally Asymmetric Flux**

1346 The final feature, the flux asymmetry (seen in Fig. 2-24), is also explained using the
 1347 1-D basket model. The detailed model shows a higher flux leaving the bottom right of
 1348 section of the cask as compared to the top left section of the cask. This discrepancy is
 1349 seen at the leftmost and rightmost exiting surfaces in Fig. 4-7. The leftmost face has a
 1350 lower exiting flux value than the value observed at the rightmost face. Figure 4-6 shows
 1351 the reason for the asymmetry: a neutron born in the left fuel cell and traveling left will
 1352 pass through three neutron absorbing pads before exiting the left face, which is the same
 1353 number of neutron absorbing pads that same neutron would have to pass through if it
 1354 were traveling right. Conversely, if a neutron is born in the right fuel cell and traveling
 1355 to the left, it passes through four neutron absorbing pads. However, if that same neutron
 1356 were to travel right, it only potentially encounters two neutron absorbing pads. The
 1357 number of neutron absorbing pads a neutron potentially encounters is not the same based
 1358 on the the location of neutron generation and direction of travel because of the placement
 1359 of neutron absorbing pads in the MPC. The asymmetric loading of these pads directly
 1360 affects the neutron flux spatial distribution exiting the spent fuel cask.

1361 To further corroborate this notion, the detailed model was adjusted, replacing the
 1362 stainless steel structure and neutron absorbing pads with vacuum. Figure 4-8 compares
 1363 the ratio of the neutron flux spatial distribution averaged over the top left section and the
 1364 flux averaged over the bottom right section from the detailed model where one simulation
 1365 replaced neutron absorbing pads with vacuum and the original detailed model. The
 1366 maximum deviation of the ratios of neutron flux spatial densities is 0.1% as a result of
 1367 replacing non-fuel structure in the MPC with vacuum, confirming the results from the
 1368 basket model. In contrast, the maximum deviation of these same ratios in the original
 detailed model is nearly 10%.

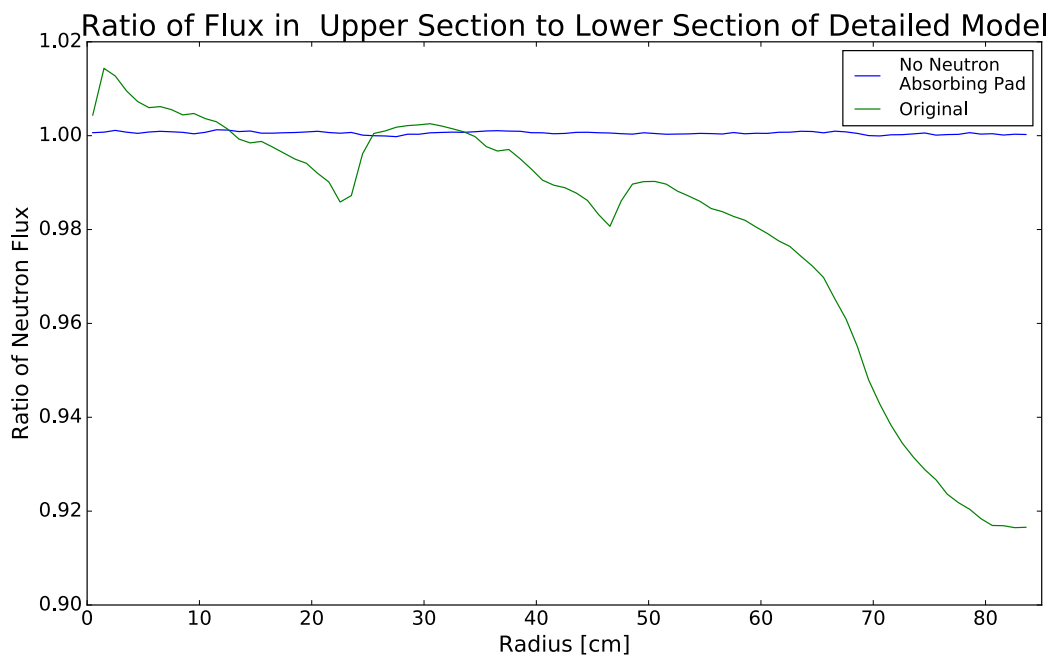


Figure 4-8. The ratio of the neutron flux spatial distribution in the upper left section of the fuel region to the neutron flux spatial distribution in the lower right section of the fuel region. This ratio is nearly 1 over the entirety of the fuel region, confirming the assumption that removing the neutron absorbing pads removes the previously identified depressions.

1369
 1370 Previous findings have shown that geometric structures finer than the stainless steel
 1371 baskets, neutron absorbing pads, and helium annulus are unnecessary for characterization
 1372 of the spatial flux distribution arising from the detailed model. A final model, the

1373 “cruciform model”, is developed to ensure no important physics are neglected in the
1374 reduced-order modeling and analysis process. This model uses the cell homogenized fuel
1375 definition in each of the 32 original fuel cells. In doing so, the stainless steel fuel basket
1376 and neutron absorbing pads are retained and discrete from the homogenized fuel. The
helium surrounding the 32 fuel cells is also retained.

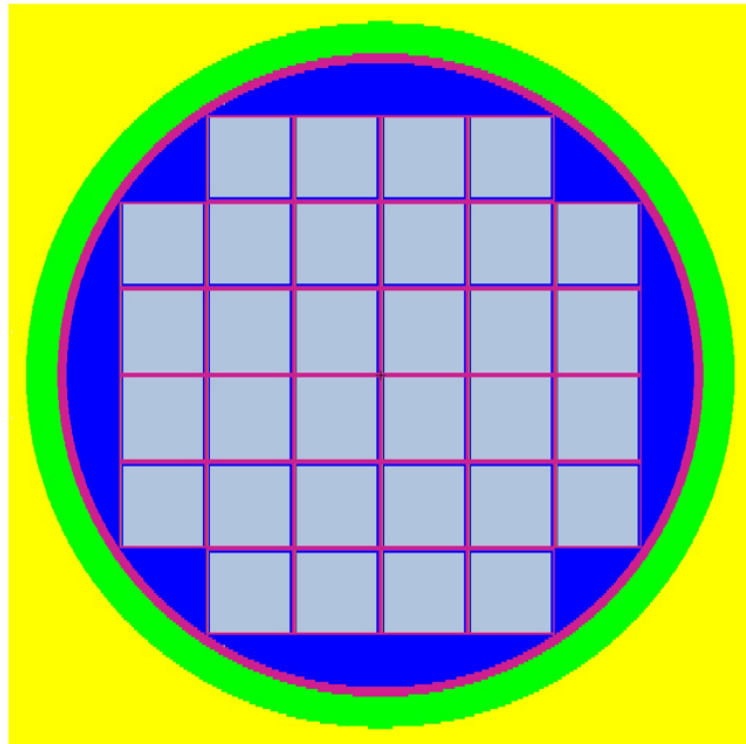


Figure 4-9. The cruciform model. The gray squares are cell homogenized fuel, the stainless steel fuel basket and MPC are pink, the helium annulus is blue, the air exterior to the MPC is green, and concrete is yellow. The neutron absorbing pads (orange) are present in this diagram, but are too thin to be seen here.

1377
1378 The neutron spatial flux distribution simulated by the cruciform model is shown in
1379 Fig. 4-10. These results underpredicts the flux from the detailed model by 5-7% through
1380 the entire fuel region, including in the helium annulus. Moreover, these results can also
1381 be interpreted as the cruciform model accounting for the physics relevant to the detailed
1382 model’s spatial neutron flux distribution at a level greater than 90%. That is, further fine
1383 detail additions to the cruciform model will “close the gap” with respect to the detailed
1384 model at a sub-10% level.

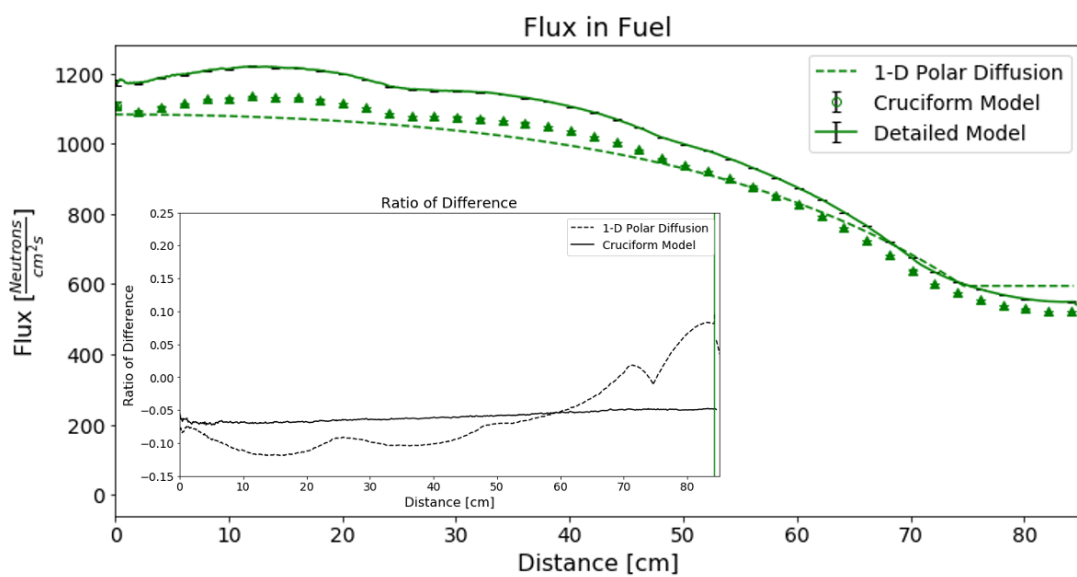


Figure 4-10. The neutron flux spatial distribution of the cruciform model (triangles) capture the flatness of, the leveling off of, and the depressions in the neutron flux spatial distribution seen in the detailed model (solid).

1385 **4.2.5 Non-exponential Decay in Concrete**

1386 The hydrogen content in concrete is responsible for thermalizing the neutron flux
1387 an attenuating neutrons. Figure 4-11 compares the neutron flux from the detailed model
1388 (solid line), the E_2S_2 analytic solution (red dashed), the fast energy group E_2S_2 solution
1389 (blue dotted), the thermal energy group E_2S_2 solution (brown dotted), and the MCNP
1390 helium model (dotted). In concrete, the neutron flux experiences a shift in energies as
1391 a result of downscattering occurring on hydrogen atoms. The analytic solutions confirm
1392 the observed shift in energies. The fast flux (the blue dotted line) decreases exponentially
1393 through the concrete regions. Intuitively, the exponential decrease is behaves similarly to
1394 an uncollided flux calculation, where the uncollided neutron flux decreases exponentially
1395 with thickness as neutrons undergo interactions in a material. In the case of concrete
1396 these interactions are mainly scattering since the scattering ratio ($\frac{\Sigma_s}{\Sigma_t}$) in the fast region
1397 for concrete is 99.5%. A high scattering ratio at fast neutron energies breeds thermal
1398 neutrons, a conclusion consistent with the initial increase in the thermal neutron flux
1399 in Fig. 4-11. As the fast neutron population decreases, the rate at which neutrons
1400 are thermalized decreases as well, which when combined with loss terms, causes the
1401 populations of both the fast and thermal neutron fluxes to decrease as a function of
1402 thickness. Both the analog MCNP model and the analytic model capture the physics of
1403 the detailed model within 10%, with the exception of the last 6cm of the analytic model.

1404 The reason the analytic model shows higher disagreement with the detailed model in
1405 the outer 6cm is a result of the boundary conditions. The E_2S_2 equations are solved using
1406 a continuous flux boundary condition at both surfaces of the model. While considering
1407 the neutron flux as continuous is a physically consistent boundary condition, higher order
1408 effects (e.g., continuity of derivatives) are not being considered. Further, the outermost
1409 boundary condition assumptions that no neutrons will re-enter the cask after leaving.

¹⁴¹⁰ While this assumption is nearly physically constituent, it will still act as source of error to
¹⁴¹¹ materials within the cask.

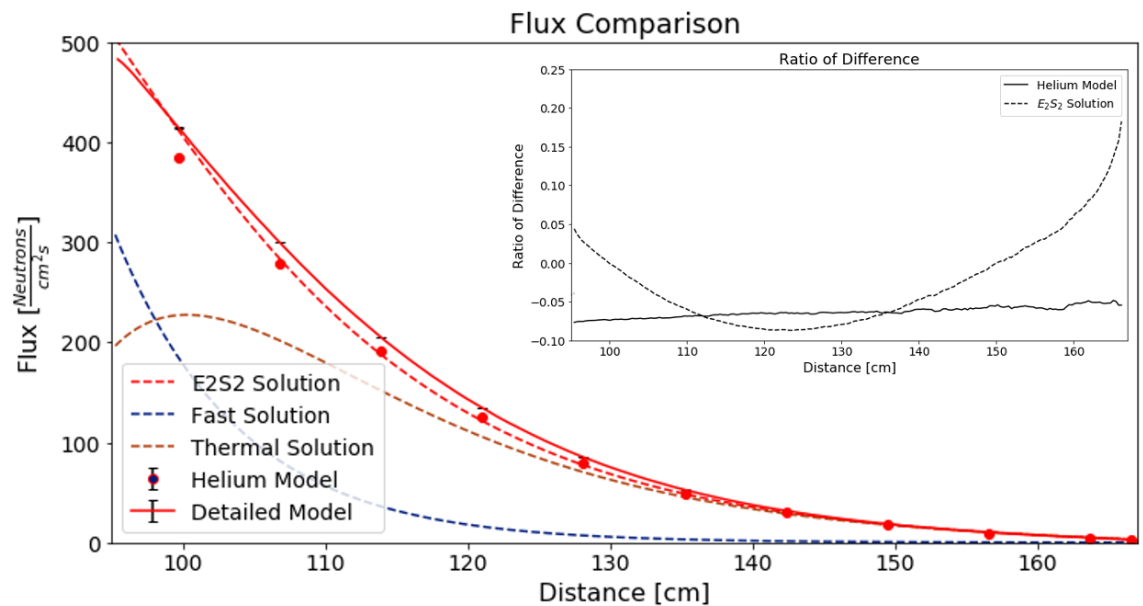


Figure 4-11. The neutron flux spatial distribution of the analytic E₂S₂ model (dashed line), helium model (circles), and detailed model (solid lines). The fast and thermal portions of the E₂S₂ solutions are shown in the blue and brown dotted lines respectively. The inset graphs shows the error between the analog models and detailed model.

¹⁴¹² 4.2.6 Flux in MPC and Carbon Steel Shell

¹⁴¹³ The MPC and carbon steel shell are the final material regions left to discuss. The
¹⁴¹⁴ thinness of these materials leads to a relatively simple discussion. Figure 4-12 compares

1415 the neutron flux from the detailed model (solid blue), the E_2S_2 model solution (dotted
1416 blue line), and the analog helium model (circles). The fast and thermal components of the
1417 E_2S_2 solution are displayed as the dark blue and brown lines respectively. Even though the
1418 thickness of the stainless steel is a similar to the MFP, some of the fast neutrons undergo
1419 scattering interactions and thermalize which results in an increase in the thermal flux.
1420 The error between the analog models and the detailed model is less than 10%. In fact, the
1421 analytic model agrees with the detailed model within 5%, which is better than the helium
1422 model.

1423 Figure 4-13 shows the neutron flux in the carbon steel shell. The flux in the carbon
1424 steel shell is almost entirely thermal since the concrete has already thermalized the
1425 neutron flux. The analytic model captures this behavior, unfortunately, the analytic model
1426 does not capture an increase in source source neutrons in the carbon steel which was
1427 observed in the detailed model. This is a result of assuming the number of neutrons bred
1428 through interactions is negligible and not including these fast neutrons in the E_2S_2 model.
1429 However, the analytic model agrees within 10-40% over the thickness of the carbon steel.
1430 Overall, this level of agreement is acceptable since the neutron flux is so small, in fact, the
1431 flux at the exiting surface of the cask is $0.68 \frac{1}{cm^2 s}$ as predicted by the detailed model and
1432 $0.91 \frac{1}{cm^2 s}$ as predicted with the E_2S_2 solution. The scale of the neutron flux is low making
1433 the larger error values acceptable. The error between the detailed and analytic models
1434 increases through the carbon steel shell as a result of the boundary conditions. At the
1435 exiting surface of the cask, the analytic solution is assumed to have a vacuum boundary
1436 condition. Meaning, none of the neutrons which leave the cask will return. While this
1437 assumption is appropriate (since the cask in the detailed model is surrounded by air), it
1438 does not exactly replicate the conditions in the detailed model. The result is an increase in
1439 error values near the outer surface of the cask.

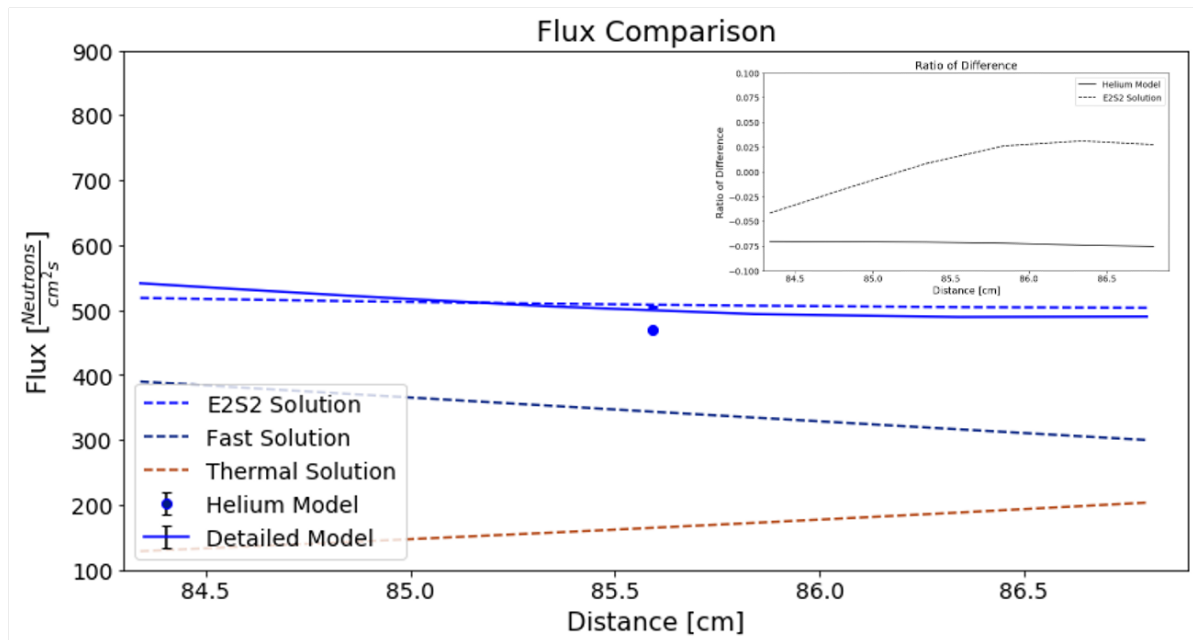


Figure 4-12. The neutron flux spatial distribution of the analytic E₂S₂ model (dashed line), helium model (circles), and detailed model (solid lines). The fast and thermal portions of the E₂S₂ solutions are shown in the blue and brown dotted lines respectively. The inset graphs shows the error between the analog models and detailed model.

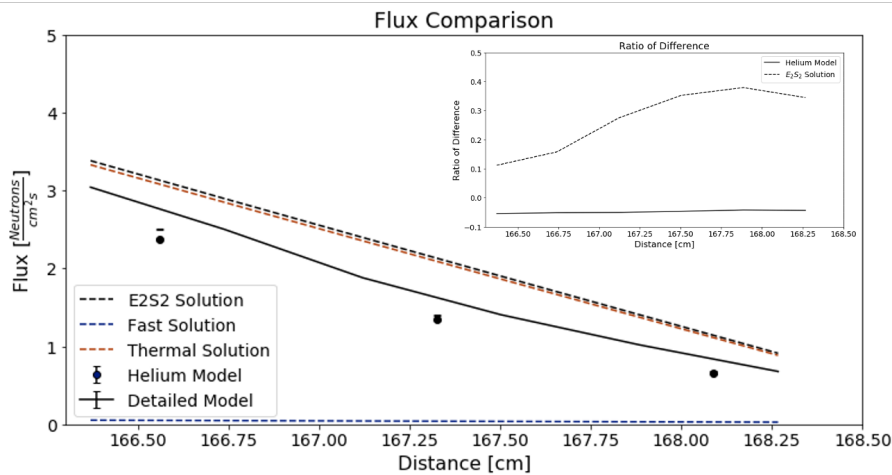


Figure 4-13. The neutron flux spatial distribution of the analytic E₂S₂ model (dashed line), helium model (circles), and detailed model (solid lines). The fast and thermal portions of the E₂S₂ solutions are shown in the blue and brown dotted lines respectively. The inset graphs shows the error between the analog models and detailed model.

1440

4.3 Summary

1441 Using reduced complexity analytic and computational models to analyze the
 1442 simulation results of a high-fidelity computational model allows for the quantification
 1443 of effects of any assumptions invoked when developing the latter model. Ensuring
 1444 important physics are preserved in the course of conducting simulations increases
 1445 the likelihood of correct results. This work exemplified this notion through a process
 1446 referred to as "simulation results assessment." As a demonstration, this work included
 1447 post-simulation analysis of a detailed MCNP model of a HI STORM 100 spent nuclear
 1448 fuel cask. A series of reduced analytic and computational models were developed and
 1449 used to identify the physics which causes features in the neutron flux spatial distribution
 1450 as calculated by the detailed model. In the HI-STORM 100 model, the stainless steel
 1451 basket, neutron absorbing pads, and helium annulus around the fuel cells are important
 1452 physical components that need to be preserved in modeling. Retaining the individual
 1453 fuel pin structure was found to be less important than broadly capturing the lumped
 1454 material properties inside the individual fuel cells. These results were corroborated using
 1455 the cruciform model, which appears to capture the physics relevant to the neutron flux
 1456 spatial distribution in the detailed model beyond the 90% level. The major features of
 1457 the neutron flux spatial distribution simulated by the detailed model are expected to be

₁₄₅₈ correct since the this model preserves material fuel properties and the geometric structure
₁₄₅₉ of the neutron absorbing pads and helium annulus.

CHAPTER 5

SENSITIVITY ANALYSIS

1462 From a practical standpoint, known functional forms (as opposed to numerical
1463 tables) are optimal for both exhaustive insight into essential phenomenology and broader
1464 application, especially if those forms are differentiable or integrable. To this point, as
1465 noted by Barenblatt,

“... for a long time ... [these] solutions were treated by most researchers as though they were merely isolated ‘exact’ solutions to special problems: elegant, sometimes useful, but extremely limited in significance. It was only gradually realized that these solutions were actually of much broader significance ...”

¹⁴⁷⁰ and moreover, by Polyanin and Zaitsev,

1471 “... exact solutions of differential equations play an important role in the
1472 proper understanding of qualitative features of many phenomena and processes
1473 in various areas of natural science ...”

¹⁴⁷⁴ and finally, by Sachdev,

1475 “... the search for exact solutions is now motivated by the desire to
1476 understand the mathematical structure of the solutions, and hence, a deeper
1477 understanding of the physical phenomena described by them. Analysis,
1478 computation, and not insignificantly, intuition all pave the way to their
1479 discovery ...”

1480 As such, even in an age dominated by computational studies there remains a distinct role
1481 for the development and implementation of analytical treatments. As summarized by
1482 Sachdevy,

1483 “... understanding the validity and place of exact/approximate analytical
1484 solution[s] in the general context can be greatly enhanced by numerical
1485 simulation. In short, there must be a continuous interplay of analysis and
1486 computation if a ... problem is to be successfully tackled.”

Now-ubiquitous quantitative code verification efforts may thus be viewed as a core element within a broader program of study; chapter 4 features a complementary analytical study to aid in the understanding of essential phenomenologies underpinning increasingly complicated computational science simulations. The remainder of chapter 5 motivates sensitivity analysis in the broader context of the results assessment methodology as a validation technique and introduces fundamental theory.

5.1 Motivation of Sensitivity Analysis

1494 As characterized by Saltelli et al.,

1495 “... sensitivity analysis is aimed ... at priority setting, to determine what
1496 factor most needs better determination, and to identify the weak links of the
1497 assessment chain (those that propagate most variance in the output) ...”

1498 Sensitivity analysis is a prime example of a field that has in recent years been almost
1499 wholly subsumed by purely computational endeavors; the literature is voluminous
1500 surrounding site-specific efforts and implementations within physics, engineering, biology,
1501 earth science, population dynamics, economics, and many other areas. This state of affairs
1502 is also reflected in the expositions of both the canonical primers and various critiques
1503 surrounding the subject.

1504 The evolution of sensitivity analysis from its historical and largely analytical roots
1505 to modern-day computational programs of study has largely proceeded in tandem with
1506 parallel developments in large-scale computational science. The reasons for this outcome
1507 include but are not necessarily limited to:

1508 1. Sensitivity analysis has emerged as one of the cornerstone processes through which
1509 generalized mathematical models or codes may be assessed through an integrated
1510 program of verification, validation, and uncertainty quantification. Modern-day
1511 sensitivity studies are therefore most commonly encountered in the context of code
1512 evaluations.

1513 2. Fully coupled, global sensitivity analyses (as opposed to their “one factor at a time”
1514 or purely local or derivative-based counterparts) are increasingly viewed as necessary
1515 components of fully rigorous code assessment strategies. These techniques typically
1516 demand repeated code execution under coupled sampling spanning the entire space
1517 of possible parameter realizations.

1518 3. Tremendous advances in the power and widespread availability of high-performance
1519 computing resources has made conceptually and computationally simple “brute-force
1520 method” sensitivity analysis approaches more viable than ever before. In these
1521 studies, even large or otherwise complicated codes can be rapidly, repeatedly
1522 executed under conjoined parameter sampling.

1523 In these often-necessary realizations of sensitivity analysis practices, complementary
1524 analytical studies assume the same historical relevance and underpinning basis, limitations,
1525 and advantages as for the attendant mathematical models.

1526 A classical example of this phenomenology with broad relevance to the nuclear
1527 engineering community is adjoint analysis, as detailed among many others by Keepin,
1528 Henry, and Lewins. As noted by Lewins,

1529 “For sensitivity and uncertainty analysis, one frequently is interested in a
1530 formulation relating the change in a given performance parameter to many
1531 different alterations in the system input or design variables.[38]”

1532 Further, Stacey, Greenspan, and Lewins and Becker discuss the appropriateness
1533 of analytical adjoint based approaches in nuclear engineering, since adjoint sensitivity
1534 calculations are best suited for applications when one is interested in the change in
1535 response to many input parameters [38–40]. Nuclear engineering is not unique in that
1536 a desired response (e.g., the neutron flux) depends on many input parameters (e.g.,
1537 nuclear data). The extent of these problems have made for a desirable application of many
1538 modern-day computational approaches for executing adjoint-based sensitivity analysis
1539 studies. However, if an analytic model has a closed-form solution, then solving the system

1540 from the forward direction is more appropriate since this process is considerably more
1541 straightforward and does not require knowledge of the adjoint solution.

1542 Closely related to analytical adjoint methods is Cacuci's "forward sensitivity
1543 analysis procedure" (FSAP) based on the concept of the Gâteaux generalized directional
1544 derivative. This formalism (if not its practical implementation) is entirely analytical,
1545 and often features minimal computational overhead; in turn, however, it only provides
1546 decoupled sensitivity information on the local or first-order level. As such, when
1547 implemented in the context of analytical mathematical models, Cacuci's FSAP shares
1548 the same general drawbacks and benefits associated with analytical modeling in general.

1549 In short, the potentially narrow scope of analytically computed sensitivity information
1550 is counterbalanced by a more complete and lucid functional representation that may prove
1551 informative of more general developments. This important idea forms the motivation of
1552 this work, to be initiated in a specific context with relevance to the nuclear engineering
1553 community.

1554 The notions previously set forth are entirely general, and may be applied in any
1555 number of contexts. Of particular relevance to this study is the implementation of the
1556 aforementioned techniques in the context of modeling and simulation of containers
1557 intended for the long-term storage of spent nuclear reactor fuel.

1558 Complementary analytical sensitivity analysis modeling of spent fuel cask scenarios is
1559 intended to serve two essential purposes:

- 1560 1. These studies can serve as guides for targeting future, entirely computational
1561 sensitivity analysis studies pertaining to spent fuel cask scenarios, thus potentially
1562 achieving computational cost savings where necessary.
- 1563 2. Analytical studies may also serve as guides for interpreting, understanding, and
1564 rigorizing certain results of existing and future computational studies pertaining to
1565 spent fuel casks.

1566 The primary objective of this work is therefore to execute an analytical sensitivity
1567 analysis study along the analytic models identified in Chpt. 4. In support of this
1568 objective, Sec. 5.2 provides a discussion of the the general concepts of sensitivity
1569 analysis as well as a detailed description of the methods used in this work. Chapter
1570 6 applies appropriate sensitivity analysis methods on the analytic and computational
1571 models. Chapter 7 compares the sensitivity analysis results between the analytic and
1572 computational models and discusses implications of those comparisons.

1573 5.2 Local Sensitivity Analysis Primer

1574 Saltelli, Chan, and Scott define sensitivity analysis as the study of “relationships
1575 between information flowing in and out of a model[41].” That is, sensitivity analysis
1576 investigates how perturbations in input parameter values influence a system’s response,
1577 where input parameters are data values passed by the user or calculated by a model
1578 and are used in the calculation of output variables. The most common input parameters
1579 appearing in nuclear engineering models are cross sections, which are derived from
1580 material properties supplied by a model or code user. In order to better understand the
1581 general process of sensitivity analysis, Oblow and Pin provide a short description of the
1582 procedure [42]. To begin, consider the set of linear equations

$$1583 \quad \mathbf{R} = \mathbf{F}(\mathbf{y}, \boldsymbol{\alpha}), \quad (5-1)$$

1584 where

1585 \mathbf{R} is a vector of the system responses,

1586 \mathbf{F} is a vector of the model equations (e.g., vector containing the diffusion
equation),

1587 \mathbf{y} is the state vector (e.g., vector of ϕ values),

1588 $\boldsymbol{\alpha}$ is the vector of the system parameters,

1589 where the vector \mathbf{F} can also represent nonlinear model equations, however, the following
1590 discussion is limited to linear equations for the purpose of this work.

1591 Local sensitivity information describes first-order sensitivities, meaning, the sensitivity
 1592 information is related to the first derivative of \mathbf{R} , (e.g. , $\frac{\partial \mathbf{R}}{\partial \boldsymbol{\alpha}}$). Further, the first derivative
 1593 describes the ratio of change in a system's response caused by changing the value of
 1594 a parameter [43]. Hence, taking the derivative of Eqn. 5-1 over each parameter, $\boldsymbol{\alpha}_i$,
 1595 independently yields

$$\frac{dR}{d\alpha_i} = \frac{\partial \mathbf{F}}{\partial \mathbf{y}} \frac{d\mathbf{y}}{d\alpha_i}. \quad (5-2)$$

1596 Since \mathbf{F} contains the analytic models described by the user, the value $\frac{\partial \mathbf{F}}{\partial \mathbf{y}}$ can be
 1597 calculated directly. Simplifying the final derivative in Eqn. 5-2 requires using the chain
 1598 rule on Eqn. 5-1 to arrive at

$$\frac{d\mathbf{y}}{d\alpha_i} = \frac{\partial \mathbf{F}}{\partial \mathbf{y}} \frac{d\mathbf{y}}{d\alpha_i} + \frac{\partial \mathbf{F}}{\partial \boldsymbol{\alpha}} \frac{d\boldsymbol{\alpha}}{d\alpha_i}. \quad (5-3)$$

1599 Re-expressing Eqn. 5-2, using Eqn. 5-3, yields the sought after sensitivity information $\frac{d\mathbf{R}}{d\boldsymbol{\alpha}}$.
 1600 However, this approach can be algebraically involved since it requires solving the set of
 1601 equations \mathbf{F} for each parameter variation.

1602 In response to this problem, Cacuci developed a method for determining sensitivity
 1603 information for all parameters simultaneously, given the function \mathbf{F} has a solution
 1604 [13]. Cacuci utilizes the Gâteaux differential (G-differential), a form of the directional
 1605 derivative, to find the differential value corresponding to each parameter simultaneously.

1606 In this paradigm, the unperturbed response value (the value of the response function
 1607 where all parameters are unperturbed) is defined as

$$\mathbf{R}(\mathbf{e}^0), \quad (5-4)$$

1608 where $\mathbf{e}^0 = (\mathbf{y}^0, \boldsymbol{\alpha}^0)$ and the superscript 0 denotes the nominal, or unperturbed, value. If,
 1609 moreover, the vector \mathbf{h}_α contains the perturbation values for M number of parameters as

$$\mathbf{h}_\alpha \equiv (\delta\alpha_1, \delta\alpha_2, \dots, \delta\alpha_M). \quad (5-5)$$

1610 Sensitivity information of the response function caused by the variations \mathbf{h}_α is found
 1611 by taking the G-differential, $\delta\mathbf{R}(\mathbf{e}^0; \mathbf{h})$, of the response function, where \mathbf{h} is the
 1612 concatenation of the perturbed parameter values and the perturbed state values;

$$\mathbf{h} \equiv (\mathbf{h}_y, \mathbf{h}_\alpha). \quad (5-6)$$

1613 Taking the G-differential of the response thus yields

$$\delta\mathbf{R}(\mathbf{e}^0; \mathbf{h}) \equiv \frac{d}{d\epsilon} [\mathbf{R}(\mathbf{e}^0 + \epsilon\mathbf{h})] \Big|_{\epsilon=0} = \lim_{\epsilon \rightarrow 0} \frac{\mathbf{R}(\mathbf{e}^0 + \epsilon\mathbf{h}) - \mathbf{R}(\mathbf{e}^0)}{\epsilon}, \quad (5-7)$$

1614 where ϵ is interpreted as an infinitesimal deviation from the nominal value of a given
 1615 parameter, and the rightmost expression is the definition of the G-derivative. In general,
 1616 the evaluated result of Eqn. 5-7 can be written as

$$\delta R(\mathbf{e}^0; \mathbf{h}) = \sum_i^M \eta_i \delta \alpha_i, \quad (5-8)$$

1617 where η_i contains sensitivity information for the parameter α_i . The values of η_i are used
 1618 to calculate the sought after sensitivity coefficients, which provide a relative comparison
 1619 between parameters. The sensitivity coefficients are thus calculated using $\delta\mathbf{R}$ as

$$S_{\alpha_i} = \frac{\delta R}{\delta \alpha_i} \frac{\alpha_i}{R(\mathbf{e}^0)} = \eta_i \frac{\alpha_i}{R(\mathbf{e}^0)}, \quad (5-9)$$

1620 where S_{α_i} is the sensitivity coefficient for parameter α_i [44].

1621 The sensitivity coefficients are used to determine the the “importance” of each
 1622 parameter. Parameters with larger sensitivity coefficients have a larger impact on the
 1623 the system response. The signs of sensitivity coefficients is also important, as the signs
 1624 indicate the direction of change in the response given a change in a parameter. Meaning,
 1625 if the sensitivity coefficient has a negative value for a given parameter, increasing the value
 1626 of that parameter will cause the value of the response to decrease. On the other hand, if
 1627 the sensitivity coefficient has a positive value, increasing the associated parameter value
 1628 will cause an increase in the response value.

₁₆₂₉ Chapter 6 investigates the effects of perturbing parameters relating to nuclear data in
₁₆₃₀ the solution to Eqn. 4-9, the solution to the 1D cylindrical diffusion equation.

1631 CHAPTER 6
 1632 SENSITIVITY THEORY OF REDUCED PHYSICS MODELS

1633 **6.1 Local Sensitivity Analysis of Representative Spent Fuel Cask Model**

1634 **6.1.1 Fuel Region**

1635 Section 3 introduced the diffusion approximation which uses experimental data in
 1636 the form of cross sections to predict the neutron flux through the fuel region of the cask.
 1637 Taking, the solution to Eqn. 3-46 with the boundary conditions given in Eqns. 4-1 and 4-2
 1638 is

$$\phi^0(r) = \frac{S^0}{D^0(B^0)^2} \left(1 - \frac{I_0(B^0 r)}{I_0(B^0 \tilde{r}^0)} \right); \quad B^0 \equiv \sqrt{\frac{\Sigma_a^0 - \bar{\nu}^0 \Sigma_f^0}{D^0}}. \quad (3-49)$$

1639 where S^0 is the intrinsic neutron source, I_0 is the modified Bessel function of the first kind,
 1640 and \tilde{r}^0 is the extrapolated radius of the fuel region equivalent to $r_b^0 + d^0$. The superscript
 1641 0 denotes the nominal value of each input parameter or response function.

1642 Identifying the unperturbed input parameters from Eqn. 3-49 as

$$\boldsymbol{\alpha}^0 \equiv (S^0, D^0, B^0, \tilde{r}^0), \quad (6-1)$$

1643 and the perturbation vector, \mathbf{h}_α as

$$\mathbf{h}_\alpha \equiv (\delta S, \delta D, \delta B, \delta \tilde{r}), \quad (6-2)$$

1644 the vector \mathbf{h}_u becomes

$$\mathbf{h}_u \equiv (\delta \phi). \quad (6-3)$$

1645 Then, the vector of nominal input parameters and response functions is defined as

$$\mathbf{e}^0 \equiv (\phi^0(r), \boldsymbol{\alpha}_0), \quad (6-4)$$

1646 where the response function is

$$R(\mathbf{e}^0) = \phi^0(r). \quad (6-5)$$

₁₆₄₇ Finally, determining the sensitivities for each input parameter using Eqns. 6-1-6-5 in Eqn.

₁₆₄₈ 5-7 is equivalent to replacing each input parameter in Eqn. 3-49 with

$$\alpha_i^0 \rightarrow (\alpha_i^0 + \epsilon \delta \alpha_i). \quad (6-6)$$

₁₆₄₉ Using Eqn. 6-6 to expand the input parameters in Eqn. 3-49 gives

$$\delta R(\mathbf{e}^0; \mathbf{h}) = \frac{d}{d\epsilon} \left[\frac{(S^0 + \epsilon \delta S)}{(D^0 + \epsilon \delta D)((B^0 + \epsilon \delta B))^2} \left(1 - \frac{I_0((B^0 + \epsilon \delta B)r)}{I_0((B^0 + \epsilon \delta B)(\tilde{r}^0 + \epsilon \delta \tilde{r}))} \right) \right] \Big|_{\epsilon=0}. \quad (6-7)$$

₁₆₅₀ Evaluating Eqn. 6-7 yields

$$\delta R(\mathbf{e}^0; \mathbf{h}) = \eta_1(r) \delta S + \eta_2(r) \delta D + \eta_3(r) \delta B + \eta_4(r) \delta \tilde{r}, \quad (6-8)$$

where the r -dependent functions appearing in Eqn. 6-8 are defined by

$$\eta_1 \equiv \frac{1 - \frac{I_0(B^0 r)}{I_0(B^0 \tilde{r}^0)}}{(B^0)^2 D^0}, \quad (6-9)$$

$$\eta_2 \equiv \frac{-S^0}{(B^0)^2 (D^0)^2} \left(1 - \frac{I_0(B^0 r)}{I_0(B^0 \tilde{r}^0)} \right), \quad (6-10)$$

$$\eta_3 \equiv \frac{-2S^0 \left(1 - \frac{I_0(B^0 r)}{I_0(B^0 \tilde{r}^0)} \right)}{(B^0)^3 D^0} - \frac{S^0 r I_1(B^0 r)}{(B^0)^2 D^0 I_0(B^0 \tilde{r}^0)} + \frac{S^0 \tilde{r}^0 I_0(B^0 r) I_1(B^0 \tilde{r}^0)}{(B^0)^2 D^0 (I_0(B^0 \tilde{r}^0))^2}, \quad (6-11)$$

$$\eta_4 \equiv \frac{S^0 I_0(B^0 r) I_1(B^0 \tilde{r}^0)}{B^0 D^0 (I_0(B^0 \tilde{r}^0))^2}, \quad (6-12)$$

$$(6-13)$$

and the associated sensitivity coefficients are summarized as

$$S_{c,S} = \eta_1 \frac{S^0}{\phi(r)}, \quad (6-14)$$

$$S_{c,D} = \eta_2 \frac{D^0}{\phi(r)}, \quad (6-15)$$

$$S_{c,B} = \eta_3 \frac{B^0}{\phi(r)}, \quad (6-16)$$

$$S_{c,\tilde{r}} = \eta_4 \frac{\tilde{r}^0}{\phi(r)}. \quad (6-17)$$

Equation 3-49 indicates that some of the input parameters appearing within may be defined in terms of other, more fundamental input parameters, such as how Σ_a^0 appears in the definition of B^0 as well as in D^0 . In practice, the values for D^0 , B^0 , and \tilde{r}^0 are calculated from experimental data or geometry (in the case of \tilde{r}^0). Therefore, it is necessary to express each of the above input parameters according to their individual definitions using Eqns. 6-18 - 6-20:

$$D^0 \equiv \frac{1}{3(\Sigma_s^0 + \Sigma_c^0 + \Sigma_f^0)}, \quad (6-18)$$

$$B^0 \equiv \sqrt{\frac{\Sigma_a^0 - \bar{\nu}^0 \Sigma_f^0}{D^0}} = \sqrt{\frac{\Sigma_c^0 + \Sigma_f^0(1 - \bar{\nu}^0)}{\frac{1}{3(\Sigma_s^0 + \Sigma_c^0 + \Sigma_f^0)}}}, \quad (6-19)$$

$$\tilde{r}^0 \equiv r_b^0 + \frac{0.710}{(\Sigma_s^0 + \Sigma_c^0 + \Sigma_f^0)}, \quad (6-20)$$

1651 where Σ_c^0 is the nominal capture cross section and r_b^0 is the nominal cask fuel region outer
 1652 radius, and the nominal total absorption cross section is redefined using $\Sigma_a^0 \equiv \Sigma_c^0 + \Sigma_f^0$.
 1653 Fundamental sensitivity coefficient results written in terms of the parameters Σ_s , Σ_c , Σ_f ,
 1654 and r_b are then determined by applying the G-derivative to each of Eqns. 6-18-6-20 and
 1655 substituting the results into their respective places in Eqn. 6-9 - 6-12.

1656 Redefining the sensitivity coefficients for B , D , and \tilde{r} in terms of those for Σ_c , Σ_s , $\bar{\nu}$,
 1657 Σ_f , and r_b is a straightforward process similar to how the coefficients were found for B , D ,
 1658 and \tilde{r} above. Taking the G-derivative of each of Eqns. 6-18-6-20, each equation is redefined
 1659 to be expressible in the terms $\delta\Sigma_c$, $\delta\Sigma_s$, $\delta\bar{\nu}$, $\delta\Sigma_f$, and δr_b . These definitions are then used
 1660 in the sensitivity coefficients summarized in Eqn. 6-14 - 6-17 to yield the final expressions.

Applying Eqn. 5-7 to Eqns. 6-18-6-20 using the following definitions for \mathbf{e}^0 and \mathbf{h} ,

$$\mathbf{e}^0 \equiv (\phi^0, \Sigma_c^0, \Sigma_s^0, \bar{\nu}^0, \Sigma_f^0, r_b^0) \quad (6-21)$$

$$\mathbf{h} \equiv (\delta\phi, \delta\Sigma_c, \delta\Sigma_s, \delta\bar{\nu}, \delta\Sigma_f, \delta r_b) \quad (6-22)$$

yields

$$\delta D(\mathbf{e}^0; \mathbf{h}) = \frac{d}{d\epsilon} \left[\frac{1}{3 \left((\Sigma_s^0 + \epsilon \delta \Sigma_s) + (\Sigma_c^0 + \epsilon \delta \Sigma_c) + (\Sigma_f^0 + \epsilon \delta \Sigma_f) \right)} \right] \Bigg|_{\epsilon=0}, \quad (6-23)$$

$$\delta B(\mathbf{e}^0; \mathbf{h}) = \frac{d}{d\epsilon} \left[\sqrt{\frac{(\Sigma_c^0 + \epsilon \delta \Sigma_c) + (\Sigma_f^0 + \epsilon \delta \Sigma_f) (1 - (\bar{\nu}^0 + \epsilon \delta \bar{\nu}))}{3 \left((\Sigma_s^0 + \epsilon \delta \Sigma_s) + (\Sigma_c^0 + \epsilon \delta \Sigma_c) + (\Sigma_f^0 + \epsilon \delta \Sigma_f) \right)}} \right] \Bigg|_{\epsilon=0}, \quad (6-24)$$

$$\delta \tilde{r}(\mathbf{e}^0; \mathbf{h}) = \frac{d}{d\epsilon} \left[(r_b^0 + \epsilon \delta r_b) + \frac{0.7104}{(\Sigma_s^0 + \epsilon \delta \Sigma_s) + (\Sigma_c^0 + \epsilon \delta \Sigma_c) + (\Sigma_f^0 + \epsilon \delta \Sigma_f)} \right] \Bigg|_{\epsilon=0}. \quad (6-25)$$

Evaluating Eqns. 6-23-6-25 determines the variations δB , δD , and $\delta \tilde{r}$ as

$$\begin{aligned} \delta B = & \frac{\delta \Sigma_s \sqrt{3}(-\bar{\nu}^0 \Sigma_f^0 + \Sigma_c^0 + \Sigma_f^0)}{2 \sqrt{(-\bar{\nu}^0 \Sigma_f^0 + \Sigma_c^0 + \Sigma_f^0)(\Sigma_c^0 + \Sigma_f^0 + \Sigma_s^0)}} - \\ & \frac{\delta \bar{\nu} \sqrt{3} \Sigma_f^0 (\Sigma_c^0 + \Sigma_f^0 + \Sigma_s^0)}{2 \sqrt{(-\bar{\nu}^0 \Sigma_f^0 + \Sigma_c^0 + \Sigma_f^0)(\Sigma_c^0 + \Sigma_f^0 + \Sigma_s^0)}} + \frac{\delta \Sigma_c \sqrt{3}(-\bar{\nu}^0 \Sigma_f^0 + 2 \Sigma_c^0 + 2 \Sigma_f^0 + \Sigma_s^0)}{2 \sqrt{(-\bar{\nu}^0 \Sigma_f^0 + \Sigma_c^0 + \Sigma_f^0)(\Sigma_c^0 + \Sigma_f^0 + \Sigma_s^0)}} + \\ & \frac{\delta \Sigma_f \sqrt{3}(-\bar{\nu}^0 (\Sigma_c^0 + \Sigma_f^0 + \Sigma_s^0) - \bar{\nu}^0 \Sigma_f^0 + 2 \Sigma_c^0 + 2 \Sigma_f^0 + \Sigma_s^0)}{2 \sqrt{(-\bar{\nu}^0 \Sigma_f^0 + \Sigma_c^0 + \Sigma_f^0)(\Sigma_c^0 + \Sigma_f^0 + \Sigma_s^0)}}, \end{aligned} \quad (6-26)$$

$$\delta D = \frac{\delta \Sigma_c + \delta \Sigma_s + \delta \Sigma_f}{3 (\Sigma_c^0 + \Sigma_f^0 + \Sigma_s^0)^2} \quad (6-27)$$

$$\delta \tilde{r} = \frac{0.7104 \delta r_b}{\Sigma_c^0 + \Sigma_f^0 + \Sigma_s^0} - \frac{0.7104 r_b^0 (\delta \Sigma_c + \delta \Sigma_f + \delta \Sigma_s)}{(\Sigma_c^0 + \Sigma_f^0 + \Sigma_s^0)^2}. \quad (6-28)$$

¹⁶⁶¹ These values are then substituted into Eqn. 6-8 in order to determine the sensitivity

¹⁶⁶² coefficients. Chapter 7 discusses the results of the sensitivity analysis.

¹⁶⁶³

6.2 Monte Carlo Based Sensitivity Analysis

1664

1665

CHAPTER 7

DISCUSSION OF SENSITIVITY ANALYSIS

1666 Chpt. 6. derived the sensitivity coefficients for each analytic model used in the
 1667 problem. This chapter will explain the trends in the sensitivity coefficients. Further, the
 1668 results from the sensitivity coefficients are compared between the analytic and MCNP
 1669 results.

1670

7.1 Comparison of Results

1671 The representative homogeneous fuel composition employed in the helium model
 1672 may therefore be used to determine an associated set of nominal input parameters
 1673 S^0 , Σ_c^0 , Σ_s^0 , $\bar{\nu}^0$, and Σ_f^0 for use with the analytical results appearing in Sec. 6.1.1,
 1674 featuring an associated quantification of their relevance to the detailed model. Given
 1675 fuel composition of the helium model, these input parameters are evaluated using the
 1676 nuclear data processing code NJOY code [45], where the necessary calculations proceed by
 1677 weighting the cross section values against the neutron source energy spectrum. Otherwise,
 1678 the nominal input parameter r_b^0 is the radius of the homogenized fuel material, 74.68 cm.
 1679 Table 7-1 provides a summary of parameter values calculated for the homogeneous fuel
 1680 associated with the helium model.

1681 Figure 7-1 depicts the sensitivity coefficients $S_{c,i}$ associated with the elemental
 1682 parameters $i = S, \Sigma_c, \Sigma_s, \bar{\nu}, \Sigma_f$, and r_b appearing within the analytical model given
 1683 by Eqn. 4-9, as calculated using Eqs. 6-9-6-12, 6-14-6-17, and 6-26-6-28 and the data
 1684 appearing in Table 7-1. Several trends are immediately evident from Fig. 7-1:

Table 7-1. Summary of cross section data in the homogenized fuel.

Parameter	Values
S^0	20.1430 $\frac{\text{neutrons}}{\text{cm}^3 \text{s}}$
Σ_c^0	0.0607976 $\frac{1}{\text{cm}}$
Σ_f^0	9.002E-3 $\frac{1}{\text{cm}}$
Σ_s^0	0.1032 $\frac{1}{\text{cm}}$
$\bar{\nu}^0$	2.6475 <i>neutrons</i>
r_b	74.68 <i>cm</i>

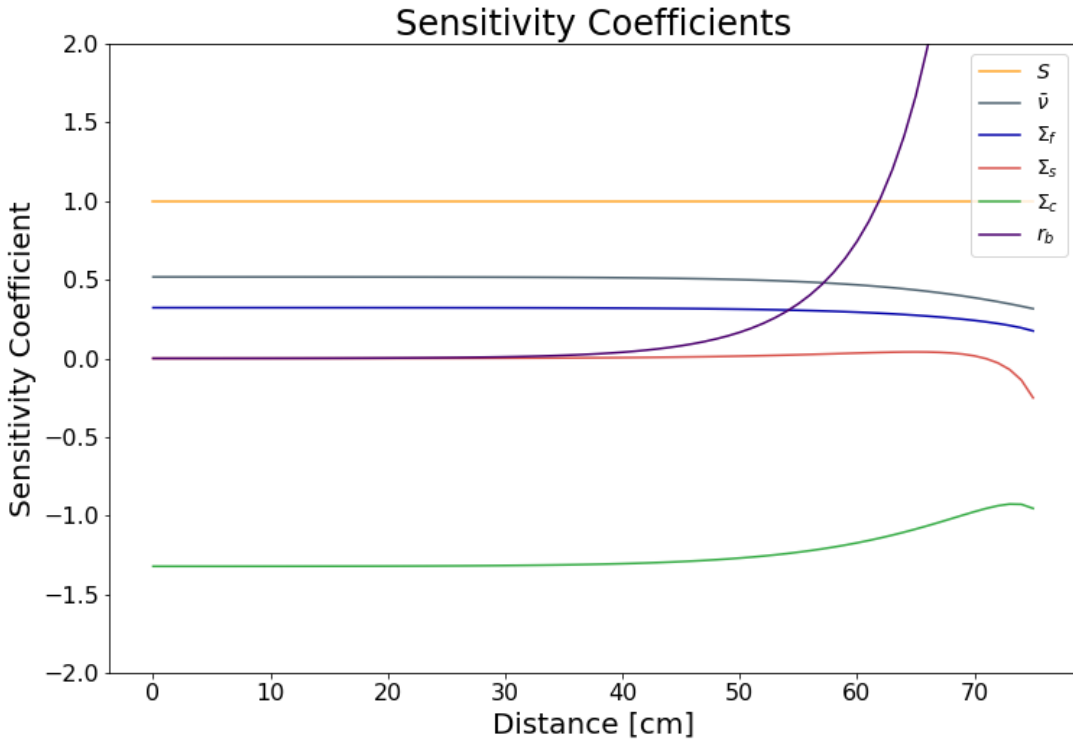


Figure 7-1. Analytical sensitivity coefficients as a function of the cylindrical radius in the homogenized fuel region.

- 1685 • The sensitivity coefficient associated with the intrinsic neutron source term S is
1686 identically one since the source term itself appears simply as a scalar multiplier
1687 within Eqn. 4-9.
- 1688 • The sensitivity coefficient associated with the capture cross section Σ_c is negative
1689 throughout the entire homogenous fuel region. This phenomenon indicates that
1690 as the capture cross section increases, the neutron flux decreases. This behavior is
1691 physically plausible since capture is a pure loss mechanism (i.e., as more neutrons
1692 are lost to capture, the value of the neutron flux becomes smaller). S_{c,Σ_c} has an
1693 inflection point and increases in value near 73 cm from the centerline, since loss
1694 terms are forcing the flux to meet to the boundary condition in Eqn. 4-2.
- 1695 • The sensitivity coefficient of r_b exhibits the most dramatic change across the radius
1696 of the cask. In fact, the value increases to 13.238 at 74.68 cm. Perturbing r_b is
1697 effectually perturbing the location of the boundary condition, Eqn. 4-2. For this
1698 reason, S_{c,r_b} increases drastically from 40 cm to 74.78 cm since boundary conditions
1699 are imperative in constructing unique solutions. This also explains why the value is
1700 less than 0.04 for the first 40 cm, as the flux at these values is less affected by the
1701 boundary condition at 74.68 cm and more affected by the boundary condition at the

1702 centerline, Eqn. 4-1. Finally, the values are positive since increasing the radius value
1703 would force the flux to remain at higher values through the radius of the fuel.

- 1704 • Figure 7-1 shows that positive perturbations in $\bar{\nu}$ cause uniformly positive
1705 perturbations in the neutron flux. This trend is physically plausible since increasing
1706 the number of neutrons generated through fission events will increase the flux value
1707 throughout a multiplying material. Along these same lines, the sensitivity coefficient
1708 for the fission cross section Σ_f is also uniformly positive since increasing the
1709 likelihood of fission will in turn increase the number of neutrons in the homogeneous
1710 fuel material (i.e., as the number of neutrons available for transport increases, the
1711 flux increases). Moreover, while there appears to be a strong correlation between
1712 $S_{c,\bar{\nu}}$ and S_{c,Σ_f} as appearing in Fig. 7-1, the two coefficients are not identical since Σ_f
1713 appears decoupled $\bar{\nu}$ as part of its inclusion in the definition of D given by Eqn. 4-9.
- 1714 • Otherwise, the sensitivity coefficients associated with Σ_f , $\bar{\nu}$, Σ_s , and Σ_c all have a
1715 similar shape: they are nearly flat for a majority of the cask's radial extent, before
1716 trending toward zero near the outer surface of the cask. This phenomenon is a
1717 consequence of all these terms appearing within the definition of B as given by Eqn.
1718 4-9, which in turn controls the shape of the analytical neutron flux. The relationship
1719 between these input parameters demonstrates how the structure of the neutron flux
1720 is related to the structure of the sensitivity coefficients, since the G-derivative is a
1721 linear operator.
- 1722 • The sensitivity coefficient associated with the scattering cross section Σ_s exhibits
1723 the most non-trivial behavior; it is positive and increasing for $r < 66.84$ cm,
1724 positive and decreasing for $66.84 \text{ cm} < r < 70.93$ cm, and negative for $r > 70.93$
1725 cm to the cask outer radius. In turn, these features are indicative of the relative
1726 importance of a variety of gain and loss mechanisms occurring within Eqn. 4-9.
1727 In particular, for $r < 70.93$ cm neutron scattering serves a gain mechanism: it
1728 acts to spatially redistribute but otherwise preserve the neutron flux within the
1729 monoenergetic diffusion model (i.e., in the absence of thermalization). For $r > 70.93$
1730 cm, neutron scattering is a loss mechanism: scattering in proximity to the outer
1731 boundary of the fuel region serves to increase leakage processes. The inflection point
1732 occurring at $r = 66.84$ cm is then indicative of the spatial location where the role
1733 of neutron scattering begins to transition: its presence owes to the approximate
1734 non-reentrant boundary condition given by Eqn. 4-2, which is intended to include
1735 leakage mechanics within the analytical diffusion model. That is, if the neutron flux
1736 was instead terminated at the physical extent of the fuel region, the analytical model
1737 would predict no neutron leakage and rather a zero neutron flux there. In this case,
1738 S_{c,Σ_s} would then be uniformly positive, which is clearly a non-physical result in the
1739 neighborhood of the cask outer boundary.

1740 To further understand and better rank the importance of the various competing

1741 physical phenomenologies included in Eqn. 4-9, Fig. 7-2 depicts the absolute value of

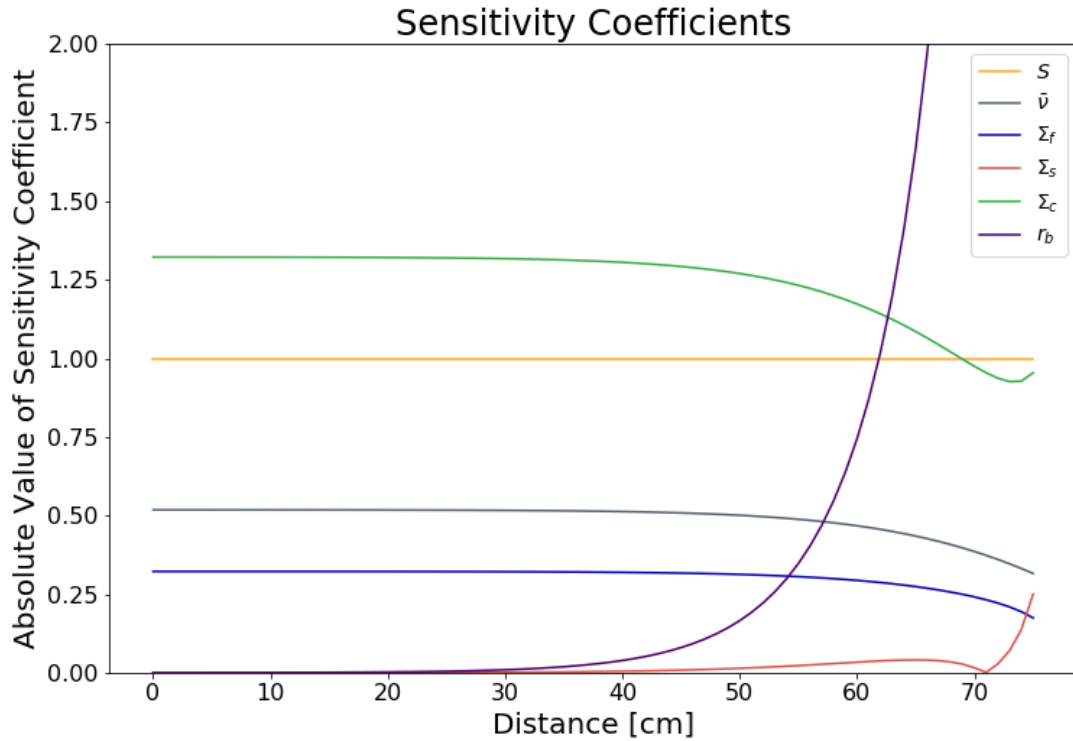


Figure 7-2. The absolute values of the sensitivity coefficients depicted in Fig. 7-1.

1742 each sensitivity coefficient plotted in Fig. 7-1. Several additional trends are immediately
 1743 evident from Fig. 7-2:

- 1744 • For a majority of the cask radius, Σ_c is the most important input parameter;
 1745 however, its importance drops near the cask outer radius as a result of the increase
 1746 in S_{c,Σ_s} caused by leakage.
- 1747 • For a majority of the cask radius, S is the second most important input parameter;
 1748 however, near 60 cm, S_{c,r_b} quickly becomes the most important parameter and
 1749 $S_{c,S}$ is briefly the third most important parameter before becoming the second the
 1750 important parameter near 69 cm.
- 1751 • For a majority of the cask radius, $\bar{\nu}$ and Σ_f are the third and fourth most sensitive
 1752 parameters, respectively. However, the sharp increase in S_{c,r_b} relegates $\bar{\nu}$ and Σ_f to
 1753 the fourth and fifth most important parameters near 55 cm.
- 1754 • For the majority of the cask, r_b is the fifth most important parameter until
 1755 approximately 35 cm where S, c, r_b increase and overtakes all the other parameters to
 1756 become the most important parameter in the system.

1757 • For a majority of the cask radius, Σ_s is the least important input parameter;
1758 however, it becomes the fourth most important parameter near the cask outer
1759 radius.

1760 These importance trends manifest in Figs. 7-1 and 7-2 due principally to the
1761 r -dependent interplay between the capture and leakage loss mechanisms present in
1762 Eqn. 4-9. For example, capture is the dominant loss mechanism near the cask centerline,
1763 as shown in Fig. 7-1 a neutron initially located there is most likely to undergo many
1764 interactions before escaping from the cask outer surface. Conversely, leakage becomes
1765 an increasingly important loss mechanism near the cask outer radius, the importance of
1766 which is observed to eventually exceed that of capture. This physical interplay noticeably
1767 manifests in the behavior of S_{c,Σ_s} and S_{c,Σ_c} as depicted in Figs. 7-1 and 7-2: for example,
1768 at the point where S_{c,Σ_s} changes sign, S_{c,Σ_c} changes slope.

1769 **7.2 Summary**

CHAPTER 8 CONCLUSIONS

Analytical models are useful tools for enhancing traditional analysis from the extensive computational modeling used in nuclear engineering. Performing sensitivity analysis reveals the underlying mathematical structure inherent to a scenario, leading to a deeper understanding of the salient physics. Incorporating a study of appropriate analytical models acts as part of a broader program of study which underpins the results from increasingly complicated computational science simulations. Further, the addition of analytically computed sensitivity information proves informative as a guide in interpreting, understanding, and rigorizing results of existing and future computational studies.

In the spirit of established analytical and computational model comparison techniques and outcomes the various analytical results, examples, and commentary provided in Chps.. 4, 6, and 7 represent an example of how an incorporated analytic and analytical sensitivity analysis studies can be used to set up, precondition, and eventually inform or compare against a complementary computational sensitivity analysis study. Within this conceptual strategy, and against the backdrop of the detailed MNCP computational model of a HI-STORM 100 spent nuclear fuel storage cask, the results appearing herein exemplify a more general recipe justifying the development and execution of local sensitivity analysis formalisms within the context of surrogate analytical models:

1789 1. Establish a high-fidelity computational model, and extract key features of the

1790 simulation output.

1791 2. Based on these key features, establish a reduced-fidelity model of the same

1792 underlying scenario; preferably this model is amenable to analytical or semi-analytical

1793 solution.

1794 3. Execute a sensitivity analysis study on the reduced-fidelity model; again, preferably

1795 this study will be amenable to analytical or semi-analytical evaluation.

1796 4. Scenario dependent evaluation of the analytical or semi-analytical sensitivity
1797 structure requires nominal input parameters; these must also be consistent with the
1798 key features extracted from the high-fidelity computational model.

1799 5. Establish scenario-dependent sensitivity trends and input parameter importance
1800 ranking to precondition additional high-fidelity computational sensitivity analysis
1801 studies.

1802 Chapters 4, 6, and 7 exemplify this process in its application to the HI-STORM 100
1803 spent fuel cask and complimentary analytic models. For example, in the case of the fuel
1804 region, the parasitic capture cross section was found to be the parameter causing the most
1805 uncertainty in the neutron flux.

1806 More broadly, results of this type are capable of guiding future research to reduce
1807 uncertainty in the most impactful input parameters inherent to a given scenario of
1808 interest. Further, by identifying the most impactful parameters a code user can identify
1809 if any simplifications were made when developing an input which would affect the results.
1810 From these conclusions, a user could either change the input to address any insufficiencies
1811 or explain the insufficiencies and identify pathways for improvement. Either decision
1812 results in a more thorough examination of the problem, which is ultimately the goal of any
1813 scientific study.

1814 Further, the analytical results provided in this work are intended to be informative
1815 of complementary studies performed using computational tools. A process exemplified
1816 in Chp. 6, perhaps the most meaningful application of this work is the performance of a
1817 purely computational, local sensitivity analysis study in the context of both the detailed
1818 and helium models, using MNCP. In such an activity, the results of this work serve two
1819 principal purposes:

1820 1. The analytical results are used to guide more expensive (in terms of time or
1821 resources) computational studies, by identifying input parameters that are either

1822 particularly important or rapidly variable at some physical location within a fuel
1823 cask geometry or physics model, or somehow otherwise impactful.

1824 2. The analytical results are directly compared to computationally derived, local
1825 sensitivity coefficient information, thus further illuminating not only the possible
1826 sufficiency and limitations of various analytical models, but also the most important
1827 physics occurring within neutron transport simulation of spent fuel cask scenarios.

1828 8.0.1 Recommendations for Future Work

1829 In addition to this necessary program of study, there appears to be a nearly limitless
1830 sequence of higher-fidelity analytical fuel cask models in which the G-derivative formalism
1831 may be brought to bear. Candidate analytical models along these lines include but are not
1832 necessarily limited to multi-group neutron diffusion models, multi-group Pn or Sn neutron
1833 transport models, and multi-group integral or integro-differential neutron transport
1834 models. Depending on the physical processes of interest, each of these models may be
1835 formulated as static or time-dependent, in various representative geometries, and featuring
1836 any number of multi-material regions. Again, the ultimate intent of analytical sensitivity
1837 analysis studies within any of these formalisms is to enable comparison to complementary
1838 computational results.

1839 Finally, and as indicated in Chp.. ??, programs of sensitivity analysis as applied to
1840 computational models of spent nuclear fuel casks appears to be an area ripe for further
1841 advancement in research and development. This being the case, and in tandem with the
1842 aforementioned potential for new, analogous analytical treatments, there also appears
1843 to be ample opportunity for the computational evaluation of not only local sensitivity
1844 information as pertaining to spent fuel casks, but also the more complete global metrics as
1845 described by Saltelli et al., and many other authors.

REFERENCES

1847 [1] “Hi-storm fsar,” Holtec International, report, 2017.

1848 [2] G. Barenblatt, *Flow, Deformation, and Fracture: Lectures on Fluid Mechanics and*
1849 *the Mechanics of Deformable Solids for Mathematicians and Physicists*. Cambridge
1850 University Press, 2014.

1851 [3] “Nuclear Power Summary - News & Notes,” DOE, Tech. Rep., April 2019.

1852 [4] R. H. J. JR., “Dry cask inventory assessment,” Savannah River National Laboratory,
1853 Tech. Rep., 2016.

1854 [5] C. Greulich and et. al., “High energy neutrons transmission analysis of dry cask
1855 storage,” *Nuc. Inst. and Meth. in Phys. Res. A*, vol. 874, pp. 5–11, 2017.

1856 [6] I. Harkness and et al., “Development of neutron energy spectral signatures for passive
1857 monitoring of spent nuclear fuels in dry cask storage,” *EPJ Web of Conferences-
1858 ANIMMA 2017*, vol. 170, 2018.

1859 [7] I. Harkness and et. al., “Feasibility of fast neutron spectroscopy for safeguards and
1860 verification of spent fuel in dry cask storage,” Los Alamos National Laboratory, Tech.
1861 Rep. LA-UR-18-29519, 2018.

1862 [8] W. Fickett, “Detonation in miniature,” *Am. J. Phys.*, vol. 47, no. 12, pp. 1050–1059,
1863 1979.

1864 [9] “Guide for verification and validation in computational solid mechanics,” American
1865 Society of Mechanical Engineers, American National Standard ASME V&V 10-2006,
1866 2006.

1867 [10] W. L. Oberkampf and T. G. Trucano, “Verification and validation benchmarks,” *Nuc.
1868 Eng. and Desn.*, no. 238, pp. 716–743, 2008.

1869 [11] P. Knupp and K. Salari, *Verification of Computer Codes in Computational Science
1870 and Engineering*. Chapman & Hall/CRC, 2003.

1871 [12] T. Sullivan, *Introduction to Uncertainty Quantification*. Springer, 2015.

1872 [13] D. Cacuci, *Sensitivity and Uncertainty Analysis: Theory*. Chapman & Hall/CRC,
1873 2003, vol. 1.

1874 [14] H. Bode, *Network Analysis and Feedback Amplifier Design*. Van Nostrand-Reinhold,
1875 1945.

1876 [15] M. D. McKay, “Sensitivity analysis,” Los Alamos Scientific Laboratory, Tech. Rep.
1877 LA-UR-79-982, 1979.

1878 [16] R. Mosteller, “Bibliography of mcnp verification and validation: 2004,” Los Alamos
1879 National Laboratory, Tech. Rep. LA-UR-04-8965, 2004.

1880 [17] F. B. Brown, "The mcnp6 analytic criticality benchmark suite," Los Alamos National
1881 Laboratory, Tech. Rep. LA-UR-16-24255, 2016.

1882 [18] P. Grechanuk and et al., "Semi-analytic benchmarks for mcnp6," *2017 American Nuc.*
1883 *Soc. Annual Meeting*, no. LA-UR-17-20668, 2017.

1884 [19] P. Roache, *Verification and Validation in Computational Science and Engineering*.
1885 Hermosa, 1998.

1886 [20] B. C. Kiedrowski and et al., "Mcnp6 shielding validation suite: Past, present, and
1887 future," *2011 American Nuc. Soc. Winter Meeting*, 2011.

1888 [21] F. B. Brown, M. E. Rising, and J. L. Alwin, "Verification of mcnp6.2 for nuclear
1889 criticality safety applications," Los Alamos National Laboratory, Tech. Rep.
1890 LA-UR-17-23822, 2017.

1891 [22] S. Mashnik, "Validation and verification of mcnp6 against intermideat and
1892 high-energy experimental data and results by other codes," Los Alamos National
1893 Laboratory, Tech. Rep., 2010.

1894 [23] Y. Chen and et. al., "Surface dose rate calculations of a spent-fuel storage cask by
1895 using mavric and its comparison with sas4 and mcnp," *Nuclear Thechnology*, vol. 175,
1896 no. 1, pp. 343–350, 2017.

1897 [24] A. Chen, Y. Chen, J. Wang, R. Sheu, Y.-W. Liu, and S. Jiang, "A comparison of dose
1898 rate calculations for a spent fuel storage cask by using mcnp and sas4," *Annals of*
1899 *Nuclear Engineering*, vol. 35, pp. 2296–2305, 2008.

1900 [25] Thiele.H and F.-M. Borst, "Shielding benchmark calculations with scale/mavric and
1901 comparison with measurements for the german cask castor haw 20/28 cg," *Nuclear*
1902 *Thechnology*, vol. 168, no. 3, pp. 867–870, 2017.

1903 [26] C. Wharton, E. Seabury, A. Caffrey, and P. Winston, "Summary report: Inl cdcis
1904 cask scanner testing at doel, belgium," Idaho National Laboratory, Tech. Rep., 2013.

1905 [27] C. R. Priest, "Dosimetry, activation, and robotic instrumentation damage modeling
1906 of the holtec hi-storm 100 spent nuclear fuel system," Master's thesis, North Carolina
1907 State University, MS Thesis 2014.

1908 [28] C. A. Miller and et. al., "Verification of dry storage cask loading using monoenergetic
1909 photon sources," *Annals of Nuclear Engineering*, vol. 137, 2020.

1910 [29] R. Kelly and et al., "Uncertainty quantification of concrete utilized in dry cask
1911 storage," *Rad. Transport and Pro.*, 2013.

1912 [30] Y. Gao and et. al., "Radiation dose rate distributions of spent fuel casks estimated
1913 with mavric based on detailed geometry and continuous-energy," *An. of Nuc. Eng.*,
1914 no. 117, pp. 84–97, 2018.

1915 [31] H. Yang, C. Liao, and Z. Liu, “Imaging a dry storage cask with cosmic ray muons,”
 1916 Oregon State University, Tech. Rep., 2018.

1917 [32] C. Liao and H. Yang, “Design of a cosmic-ray muon tomography system for dry
 1918 storage cask imaging,” *IEEE*, 2014.

1919 [33] (2019, Dec). [Online]. Available: <https://www.nrc.gov/waste/spent-fuel-storage/dry-cask-storage.html>

1920

1921 [34] H. R. Trellue and et. al., “Description of the spent nuclear fuel used in the next
 1922 generation safeguards initiative to determine plutonium mass in spent fuel,” Los
 1923 Alamos National Laboratory, report, 2011.

1924 [35] “Scale: Comprehensive modeling and simulation suite for nuclear safety analysis and
 1925 design,” Oak Ridge National Laboratory, report, 2011.

1926 [36] G. I. Bell and S. Galsstone, *Nuclear Reactor Theory*. Von Nostrand Reinhold
 1927 Company, 1970.

1928 [37] J. J. Duderstadt and L. J. Hamilton, *Nuclear Reactor Analysis*. John Wiley and Sons,
 1929 1876.

1930 [38] J. Lewins and M. Becker, *Sensitivity and Uncertainty Analysis of Reactor Performance
 1931 Parameters*, ser. Advances in Nuclear Science and Technology. Plenum Press, New
 1932 York, 1982, vol. Vol. 14.

1933 [39] W. M. Stacey, *Variational Methods in Nuclear Reactor Physics*. Academic Press,
 1934 New York, 1974.

1935 [40] E. Greenspan, *Developments in Perturbation Theory*, ser. Advances in Nuclear Science
 1936 and Technology. Academic Press, New York, 1976, vol. Vol. 9.

1937 [41] A. Saltelli, K. Chan, and E. M. Scott, *Sensitivity Analysis*. John Wiley & Sons, 2000.

1938 [42] E. M. Obloj and F. G. Pin, “Sensitivity analysis using computer calculus: A nuclear
 1939 waste isolation application,” *Nuc. Science and Eng.*, vol. 94, pp. 46–65, 1986.

1940 [43] *Sensitivity Analysis and Applications to Nuclear Power Plant*, The University fo
 1941 Tennessee. IEEE IJCNN, 1992.

1942 [44] Y. Qiu, M. Aufiero, K. Wang, and M. Fratoni, “Development of sensitivity analysis
 1943 capabilities of generalized responses to nuclear data in monte carlo code rmc,” *An. of
 1944 Nuc. Eng.*, no. 97, pp. 142–152, 2016.

1945 [45] R. MacFarlane and et.al., *The NJOY Nuclear Data Processing System, Version 2016*,
 1946 Los Alamos National Laboratory, December 2016.

1947

BIOGRAPHICAL SKETCH

1948 Tyler Joseph Remedes began his academic career at Colorado School of Mines.
1949 He always enjoyed a challenge and chose to pursue a Bachelors of Science degree in
1950 Engineering Physics. While at Mines, he was an undergraduate researcher in Dr. Uwe
1951 Griefe's research group where he helped develop, prepare, and test organic neutron
1952 scintillation detectors. It was through this experience that he decided to continue his
1953 education at the University of Florida. Tyler's time at UF saw research in many areas of
1954 nuclear engineering as he explored various realms of nuclear engineering, including nuclear
1955 fuels, cosmic radiation shielding, nuclear imaging, and finally neutronics. Tyler spent
1956 his first summer at Los Alamos National Laboratory in 2016 where he worked on signal
1957 processing for ultra-fast radiation detection. In 2018, Tyler returned to Los Alamos, this
1958 time to stay, and worked with Dr. Scott Ramsey and Mr. Joe Schmidt learning about the
1959 utility of analytics as applied to neutronics. His time working with Dr. Ramsey and Mr.
1960 Schmidt has been a transformative period for Tyler.